

**TRƯỜNG ĐẠI HỌC QUY NHƠN  
QUY NHON UNIVERSITY**

**TẠP CHÍ KHOA HỌC  
JOURNAL OF SCIENCE**

**CHUYÊN SAN KHOA HỌC TỰ NHIÊN VÀ KỸ THUẬT  
ISSUE: NATURAL SCIENCES AND ENGINEERING**

**15 (3)**  

---

**2021**

**BÌNH ĐỊNH, 6/2021**



## MỤC LỤC

1. Một kỹ thuật lấy mẫu phục vụ hiển thị ánh sáng  
**Lê Thị Kim Nga, Đoàn Thị Xương, Lương Thị Mộng Duyên** .....5
2. Nghiên cứu đặc tính động của động cơ không đồng bộ tuyến tính đơn biên ba pha ứng dụng trong thang máy  
**Trương Minh Tấn, Nguyễn Bình Tài** .....13
3. Vận hành tối ưu hệ thống năng lượng (điện - gas) có xét đến năng lượng mặt trời, gió và hệ thống tích trữ trên cơ sở mô hình Energy Hub  
**Hà Thanh Tùng, Phạm Thị Hồng Anh, Phạm Thị Ngọc Dung** .....21
4. Quy trình tính toán độ bền dầm bê tông cốt thép chịu mômen uốn - xoắn đồng thời theo TCVN 5574:2018  
**Phạm Thị Lan, Hoàng Công Duy** .....31
5. Ảnh hưởng của một số phân hữu cơ vi sinh đến sinh trưởng và năng suất của măng tây xanh (*Asparagus officinalis* L.) trồng tại thành phố Quy Nhơn, tỉnh Bình Định  
**Nguyễn Thị Y Thanh, Bùi Hồng Hải, Đoàn Công Thiên, Hồ Tân** .....43
6. Sự hội tụ địa phương của một kiểu phương pháp Newton gần đúng sử dụng mô hình tối ưu trong bài toán con  
**Trần Ngọc Nguyên, Nguyễn Văn Vũ** .....53
7. Về một phương trình ma trận  
**Nguyễn Duy Ái Nhân, Dư Thị Hòa Bình** .....61
8. Xác định sự xuất hiện vết nứt bằng phương pháp biến đổi Wavelet  
**Hoàng Công Vũ, Nguyễn Thị Thảo Nguyên** .....67
9. Tối ưu hóa dựa trên thiết kế tổng hợp trung tâm (CCD) cho quá trình chuyển hóa axit béo tự do trong dầu chiết xuất từ bã cà phê thành diesel sinh học  
**Phan Thị Thanh Phương, Võ Văn Tiến, Nguyễn Việt Quang, Lê Thị Thanh Ngân, Đặng Nguyễn Thoại** .....77



# Một kỹ thuật lấy mẫu phục vụ hiển thị ánh sáng

Lê Thị Kim Nga<sup>1,\*</sup>, Đoàn Thị Xương<sup>2</sup>, Lương Thị Mộng Duyên<sup>3</sup>

<sup>1</sup>*Viện Nghiên cứu ứng dụng khoa học và công nghệ, Trường Đại học Quy Nhơn, Việt Nam*

<sup>2</sup>*Thư viện, Trường Đại học Quy Nhơn, Việt Nam*

<sup>3</sup>*Khoa Khoa học máy tính và Công nghệ thông tin, Trường Đại học Quang Trung, Việt Nam*

*Ngày nhận bài: 27/11/2020; Ngày nhận đăng: 27/02/2021*

## TÓM TẮT

Tạo ra được cảm giác chân thực cho các hình ảnh 3 chiều là chủ đề rất được quan tâm trong lĩnh vực đồ họa máy tính và thực tại ảo. Một trong những hướng tiếp cận phổ biến cho bài toán này là sử dụng dò tia ngẫu nhiên trên cơ sở phương trình tô bóng. Bài báo trình bày một kỹ thuật lấy mẫu phục vụ hiển thị ánh sáng trên cơ sở một số tùy chỉnh với tiếp cận dò tia ngẫu nhiên theo phương trình tô bóng.

**Từ khóa:** *Lấy mẫu, Monte Carlo light transport, thực tại ảo, dò tia, tô bóng.*

---

*\*Tác giả liên hệ chính.*

*Email: kimnle@arist.edu.vn*

# A sampling technique for light display

Le Thi Kim Nga<sup>1,\*</sup>, Doan Thi Xuong<sup>2</sup>, Luong Thi Mong Duyen<sup>3</sup>

<sup>1</sup>Research Institute for Applied Science and Technology, Quy Nhon University, Vietnam

<sup>2</sup>Library, Quy Nhon University, Vietnam

<sup>3</sup>Faculty of Computer Science and Information Technology, Quang Trung University, Vietnam

Received: 27/11/2020; Accepted: 27/02/2021

## ABSTRACT

Creating realistic sense for 3D images is a great topic of interest in the field of computer graphics and virtual reality. One of the common approaches to this problem is to use random ray tracing based on shading equations. The paper presents a sampling technique for light display based on a number of customizations with random ray tracing approach according to the shading equation.

**Keywords:** Sampling, Monte Carlo light transport, virtual reality, ray tracing, shading.

## 1. INTRODUCTION

Nowadays, virtual reality is one of the key science and technology fields thanks to its broad applicability in various aspects of life, such as health, education, architecture, military, tourism, and entertainment, etc. With many products being implemented, according to<sup>1</sup> the market for virtual reality products is predicted to grow from US \$7.9 billion in 2018 to US \$44.7 billion in 2024, with the annual growth rate of 33.5% during the forecast period.



**Figure 1.** A number of virtual reality applications

One of the most interesting research issues of virtual reality is the shading techniques

for displaying high-fidelity 3D images. We have known that to see an object, the light from that object must reach our eyes. Light can come from a light source, hit the object and bounce off our eyes. It is also possible that light collided with another object or other objects before it touched the object. Hence when looking at a point on an object, there are countless rays of light that collide violently in the scene before hitting that point and reaching our eyes. Typically, studies will attempt to analyze and simulate part of that process to build realistic lighting display techniques.

One of the well-known studies on understanding how light travels through space to calculate emission levels at each point is the shading equation given by Kajiya.<sup>2</sup> Accordingly, the emission at a point is calculated internally by summing up the emission level itself and the intensity of the reflected radiation when the surface is illuminated by light sources.

\*Corresponding author.

Email: [kimmle@arist.edu.vn](mailto:kimmle@arist.edu.vn)

$$\begin{aligned}
 &L_0(x, \vec{\omega}_0) \\
 &= L_e(x, \vec{\omega}_0) \\
 &+ \int_{\Omega(\vec{n})} f_r(x, \vec{\omega}_i) \\
 &\rightarrow \vec{\omega}_0).L_i(x, \vec{\omega}_i).\cos(\vec{n}_i, \vec{\omega}_i)d\omega_i
 \end{aligned}$$

In which,  $L_0$  is the radiation intensity at  $x$  point in one direction  $\vec{\omega}_0$ .  $L_0$  will be calculated by the intensity of radiation itself.  $L_e$  and the sum of reflections is calculated using a distribution function of two-dimensional reflection.<sup>3</sup> If the surface is not a source, value  $L_e$  is equal to 0.

According to the shading equation, reflected radiation is synthesized in all possible directions of the incident light rays. This calculation is impractical, so we can apply Monte Carlo numerical simulations to sample the incident light rays, thereby turning the integral into a finite sum.

A study using light-based simulation with this approach is Cinematic Rendering,<sup>4</sup> which results in high-quality 3D images from tomography data. The technique is built on the basis of applying Monte Carlo method to randomly sample the traced rays along with using shading equation on cube data.

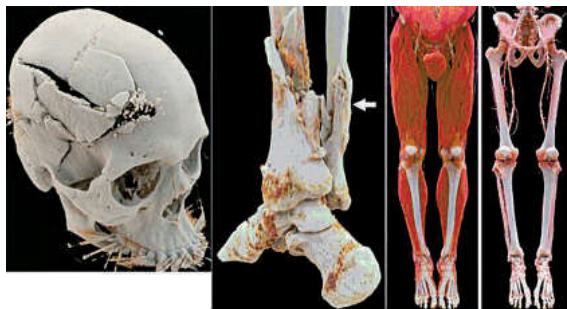


**Figure 2.** A number of images of Cinematic Rendering<sup>4</sup>

Using ray tracing to approximate the actual transmission of light by the Monte Carlo method is also one of the common approaches in computer graphics to create images for high-quality 3D animation. This access is used in some Pixar animation studio data. By rendering high-definition animations, the amount of rays used is extremely large, which also leads to

the need for computational time. According to Christensen team,<sup>5</sup> it takes about 15 to 24 hours for a frame rendering for films like Cars and Monsters University.

The paper presents a sampling technique for displaying light according to the random ray tracing approach to perform light synthesis based on shading equations. Accordingly, Section II will detail the theoretical contents of techniques with reflection ray sampling, light source point sampling as well as random ray interruption. In Section III, there are some test results with analysis of the output quality as well as the execution time corresponding to the technical customizations. Conclusion is at the end.

## 2. A SAMPLING TECHNIQUE FOR LIGHT DISPLAY

### 2.1. Directional scattering

When light strikes a surface, what is visible to the surface is reflected rays. Figuring out how to estimate the direction of the reflected ray is an important criterion in simulating light hitting that surface. For some surfaces, such as mirrors, the reflected light is considered to be perfect according to the laws of light reflection, ie the incident ray and the reflected ray align with the surface normal at equal angles. With some non-glossy surfaces, the light will scatter depending on the extent. And, for example, with the fabric surface, it can be considered that light is scattered evenly in all directions of the sphere half considered in the distribution function of two-dimensional reflection.

There are many ways to estimate the direction of the reflected ray. In this paper, we test reflected light rays at an intermediate level between uniform scattering and mirror reflection. Accordingly, the reflected light ray will have the taken direction as the directional ray generated according to standard distribution around the position of the reflected mirror ray.

Mirror reflection is referred as  $d_s$ ,  $d_s$  standardized to unit vector. We set up a space

with the coordinate origin at the reflection point and there are 3 base vectors,  $u$ ,  $v$  and  $d_s$ .

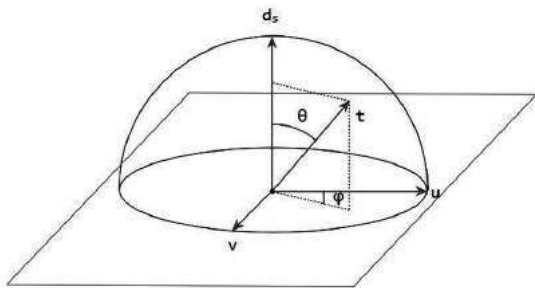


**Figure 3.** Space for generating reflection rays

In Figure 3, we can see space for generating reflection rays. In this space,  $t$  is the generated reflected ray;  $t$  originates from the reflection point and has a length of 1. Reflective generation is based on two angles  $\theta$  and  $\varphi$ . In which,  $\varphi$  is randomly distributed evenly within  $[0, 2\pi]$ ,  $\theta$  is generated as a standard distribution with an expectation of 0 then takes the absolute value.  $\theta$  is also limited to upper bound as  $\frac{\pi}{2}$ .

**2.2. Sampling the light source point**

While performing the sampling of the traced rays to perform Monte Carlo simulation for the shading equation, the path of the sampling ray needs to collide with the light source for that sampling to be meaningful. That is when the radiation value at the new observation point is updated by the sampling ray. With extremely large light sources, such as the sky, most sampling rays make sense. However, with small light sources, such as light bulbs in the room, or the sun at extremely remote locations, it is clear that the probability of the sampled rays hitting the light source is quite low. That is likely to waste a lot of computing resources.

Instead, based on some suggestions from Shirley's work,<sup>6</sup> we performed reflected radiation at each location that would be sampled by a direct ray to each light source if it is not covered and another random ray in which the direct ray from the light source will be sampled based on a random sample of the light source. Specifically, in this case, we assume that the light source is a sphere and we randomly take

points according to a uniform distribution on the light source sphere. This point together with the point to be calculated will be used to construct the ray directly with the light source.

We consider the point on the sphere described as Figure 4. In this,  $r$  is the sphere radius, and this value will be fixed for each specific sphere. The values of  $\theta$ ,  $\varphi$  will change when we consider different points on the sphere.

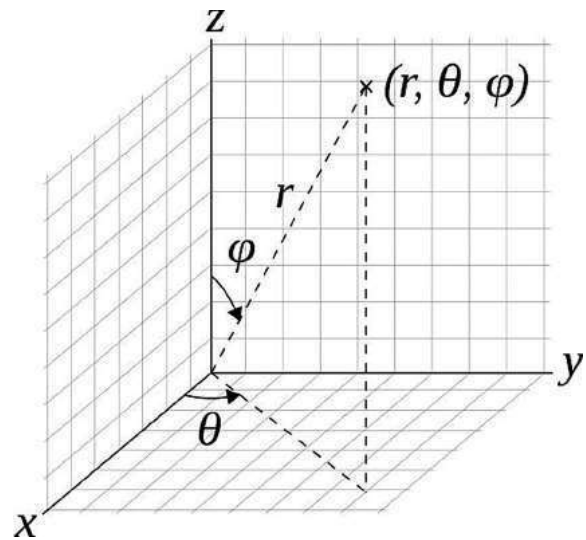


**Figure 4.** Points on the sphere represented by a set  $(r, \theta, \varphi)$

The generated score will have the following coordinates:

$$x = r \sin\varphi \cos\theta, y = r \sin\varphi \sin\theta, z = r \cos\varphi$$

Based on this we have the first case that is randomly generated by uniformly distributed  $\theta$  in  $[0, 2\pi]$  and  $\varphi$  in  $[0, \pi]$ .

However, according to Simon,<sup>7</sup> the generation in the first case will cause the generated points to be concentrated at the poles, so an alternative case is case 2 with  $\varphi = \cos^{-1}(1 - 2u)$ , where  $u$  is randomly distributed evenly in  $[0, 1]$  and  $\theta$  is generated the same way as before.

In addition,<sup>7</sup> it is also described an alternative case which is case 3: independent generation 3 values of  $x, y, z$  randomly according to the normal distribution, calling  $V = (x, y, z)$ . At that point  $P = \frac{V}{\|V\|}$  would be randomly distributed evenly across a sphere.



**2.3. Ray interruption**

Sampling of rays was carried out on the basis of physical light. In practice, however, a ray can strike continuously until it runs out of energy. That means one ray may be sampled millions of times or more, which means it is not practical to perform calculations. Moreover, having collided too many times, its contribution to radiation has also become very small. To interrupt ray generation, we experimented with a reflectance threshold value  $t \in [0,1]$ . Thus, if  $u > t$ , the ray generation process will be interrupted. In which,  $u$  is taken randomly according to uniform distribution in  $[0,1]$ . The  $t$  threshold also corresponds to the fact that surfaces have high light absorption capacity, when the amount of reflected rays will be less than those with less light absorption. In addition, to limit the number of rays, we set a parameter of the ray interruption limit, that is, the maximum number of reflections possible of the rays in the rendered scene.

**3. EXPERIMENT**

The program was tested and installed on the basis of Visual C++ 2015, with the support of two open sources OpenCV<sup>8</sup> and montelight-cpp.<sup>9</sup> The rendering process is performed purely on the CPU. The test scene is designed based on the Cornell box model and conducted on an Intel Core i7-4510U 2.6GHz computer.



**Figure 5.** Rendering images from left to right of different cases of spherical reflection: uniform scattering, directional scattering, mirror reflection

We can easily see the difference between the effects in Figure 5. In detail, the use of directed scattering produces an intermediate result compared with uniform scattering and mirror reflection. This is quite understandable and has been predefined from the theoretical content. Next, we sample the light source point

sample in 3 described cases in Section 2.2. To show how points are generated, we visualize the sampling points. In which, 800 points were sampled on a case by case basis described as Figure 6.

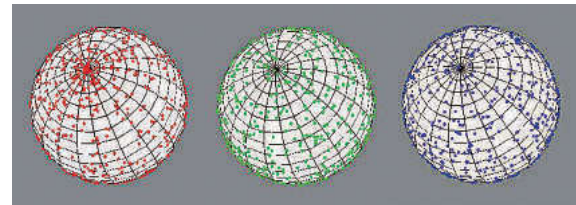


**Figure 6.** Description of sampling random points on a sphere in 3 cases: Case 1 in red, Case 2 in green, Case 3 in blue

Obviously, the points focus more on the pole in Case 1 when we randomly generate both angles in a uniform distribution. In the other two cases, the points are evenly distributed on the surface of the sphere. To illustrate the effect of 3 light point sampling strategies, we perform image rendering with two cases where the light source is a large sphere and the light source is a small sphere. Result is described as Figure 7.

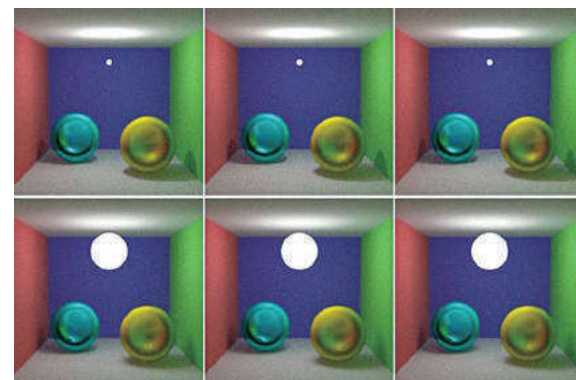


**Figure 7.** Rendering images according to 3 light source sampling points: cases in order of 1, 2, 3 turn from left to right and the top row is with a small light source, the bottom row is a large light source

In the test, with each rendering, 50 rays were sampled. It was found that there was no clear difference in the influence of 3 light source sampling cases for both small and large light sources. Thus, although Case 1 is not really random according to the uniform distribution of the sphere, we can use it to get the same result.

In order to experiment with the ray interruption, the threshold for generating reflected

rays is set individually between different objects in the scene, while the ray interruption limit will be fixed in the whole scene. We also performed a run time comparison between ray break limits with 128x128 image rendering test and 50-ray sampling.

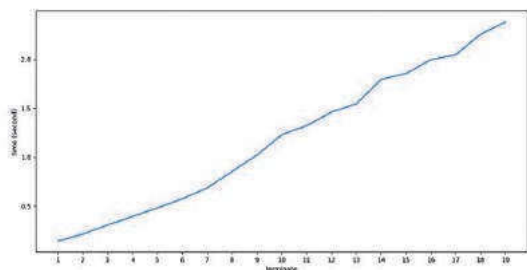


**Figure 8.** Diagram between ray interruption limit and runtime

We observe Figure 8 to visualize the relationship between the interrupt limit and run time. There is a relatively clear time difference between the ray interruption limits and the change is almost linear in proportion to the ray interruption limits. This is quite understandable because the calculated volume is equivalent at once taking rays at a point.



**Figure 9.** Images rendered with ray interruption limits, respectively 1, 2, 3, 4

To visualize more clearly the effect of ray interruption limits to rendered image, we observe Figure 9. This is image results shown corresponding to the different ray interruption limits. With Level 1, the shadow areas are very clear because the ray only reflects once, so in addition to direct light from the light source, there is no other source. Therefore, places hidden from the direct light source will have no light. In addition, with a limit of 2, the hidden regions have secondary reflecting light, which is no longer dark, but these must be higher interruptions, mirror reflection and directional scattering effects on surface of the two new spherical balls is clearly shown.

#### 4. CONCLUSION

The paper presents a sampling technique for displaying light according to the random ray tracing approach to perform light synthesis based on shading equations. Research simulating light effects to express images with high fidelity is one of the most interesting research issues of virtual reality. This problem is even more meaningful in terms of the field of virtual reality, which becomes popular in the world in general and in Vietnam in particular. The paper presents a sampling technique for light display on a random ray based on shading equations. These are important initial research results for the team to serve as the foundation for further studies in the field of graphics and virtual reality.

#### REFERENCES

1. Markets and markets, Virtual Reality Market with COVID-19 Impact Analysis by Offering (Hardware and Software), Technology, Device Type (Head-Mounted Display, Gesture-Tracking Device), Application (Consumer, Commercial, Enterprise, Healthcare) and Geography - Global Forecast to 2025, <<https://www.marketsandmarkets.com/Market-Reports/reality-applications-market-458.htm>>, last accessed on 23/5/2020.
2. J., T. Kajiya. *The rendering equation*, ACM SIGGRAPH Computer Graphics, Proceedings of the 13<sup>th</sup> annual conference on Computer graphics and interactive techniques, 31/8/1986.
3. Forsyth, A . David. *Computer vision: A modern approach*, 2<sup>nd</sup> edition, Pearson, New York, 2012.
4. M. Eid, C. D. De Cecco, et al. Cinematic rendering in CT: a novel, lifelike 3D visualization technique, *American Journal of Roentgenology*, **2017**, 209(2), 370-379.
5. P. H. Christensen, J. Fong, D. M. Laur, and D. Batali. Ray tracing for the movie ‘Cars’, *IEEE Symposium on Ray Tracing*, **2006**, 1-6.

6. P. Shirley, C. Wang, and K. Zimmerman. Monte Carlo techniques for direct lighting calculations, *ACM Trans. Graph*, **1996**, 15(1), 1-36.
7. C. Simon. Generating uniformly distributed numbers on a sphere, <<http://corysimon.github.io/articles/uniformdistn-on-sphere/>>, last accessed on 23/5/2020.
8. Open source computer vision library, <<https://sourceforge.net/projects/opencvlibrary/>>, last accessed on 23/5/2020.
9. Montelight, <<https://github.com/Smerity/montelight-cpp>>, last accessed on 23/5/2020.



# Nghiên cứu đặc tính động của động cơ không đồng bộ tuyến tính đơn biên ba pha ứng dụng trong thang máy

Trương Minh Tấn<sup>1,\*</sup>, Nguyễn Bình Tài<sup>2</sup>

<sup>1</sup>Phòng Đào tạo Đại học, Trường Đại học Quy Nhơn, Việt Nam

<sup>2</sup>Trường Cao đẳng Kỹ thuật Công nghệ Quy Nhơn, Việt Nam

Ngày nhận bài: 22/12/2020; Ngày nhận đăng: 30/03/2021

## TÓM TẮT

Động cơ không đồng bộ tuyến tính có mạch từ hở nên từ thông không liên tục từ cực này đến cực khác mà nó bị cắt ra ở đoạn đầu và đoạn cuối làm từ trường trong động cơ mất đối xứng cũng như dòng điện xoáy trong mạch thứ cấp gây ra sức từ động không sin và gọi là hiệu ứng đầu cuối và dòng xoáy. Việc ứng dụng loại động cơ này trong thang máy cũng đã được quan tâm, tuy nhiên để thực hiện tốt và phát triển loại mô hình truyền động này thì cần có nền tảng nghiên cứu về đặc tính làm việc của động cơ, đặc biệt là đặc tính động. Bài báo đề cập đến vấn đề nghiên cứu đặc tính động của động cơ không đồng bộ tuyến tính đơn biên ba pha ứng dụng trong thang máy trong các trường hợp không mang tải, mang tải, tần số thay đổi và nguồn điện mất đối xứng. Phương pháp mô phỏng trên phần mềm Matlab được sử dụng trong nghiên cứu này.

**Từ khóa:** Động cơ không đồng bộ tuyến tính, truyền động thang máy chở khách, mô hình động.

---

\*Tác giả liên hệ chính.

Email: [truongminhtan@qnu.edu.vn](mailto:truongminhtan@qnu.edu.vn)

# Study on dynamic characteristics of three-phase single-side linear induction motor used in elevator

Truong Minh Tan<sup>1,\*</sup>, Nguyen Binh Tai<sup>2</sup>

<sup>1</sup>Undergraduate Training Office, Quy Nhon University, Vietnam

<sup>2</sup>Quy Nhon Engineering and Technology College, Vietnam

Received: 22/12/2020; Accepted: 30/03/2021

## ABSTRACT

Linear induction motor has open magnetic circuits, so the flux is discontinuous from one pole to the other where it is cut off at the beginning and at the end, making the magnetic field in the motor asymmetric as well as the eddy currents in the secondary circuit cause non-sinusoidal magneto-motive force and is called end effect and eddy current. The application of this motor type in elevators has been of great interest, but to perform well and develop this drive type, it is necessary to have a research background on the working characteristics of motor, especially the dynamic characteristics. The paper deals with the study of dynamic characteristics of three-phase single-side linear induction motor used in elevator in the no-load and loaded elevator, variation of frequency and asymmetric power supply. The simulation method on Matlab software is used in this study.

**Keywords:** *Linear induction motor, passenger elevator drives, dynamic model.*

## 1. INTRODUCTION

Elevator is a specialized equipment to transport of passengers, goods, materials, etc. in vertical direction. The characteristics of transport by elevator compared to other means of transportation are the time of a small transport cycle, large transportation frequency, continuous opening and closing of the machine.

Structure diagram of elevator using linear induction motor (LIM), drive winch with cable sheave by friction is shown in Figure 1.<sup>1</sup> The winch is located above the elevator shaftway which run along the entire height of the building. On the load-bearing structure along the elevator shaftway, there are guide rails attached to the counterbalance unit and the elevator cabin which are hung on the two ends of the lifting cables thanks to the suspension system. The suspension system is intended to ensure that the individual

lifting cables are of equal tension. The lifting cable is squeezed through the cable grooves of the friction pulley of the winch. When the LIM operates, the towing winch operates, the friction pulley rotates and transmits motion to the lifting cable, the elevator cabin goes up or down on the guide rails along the elevator shaftway, LIM rests on guide rails along the length of the secondary part.

Linear induction motor has open magnetic circuits, so the flux is discontinuous from one pole to the other where it is cut off at the beginning and at the end, making the magnetic field in the motor asymmetric as well as the eddy currents in the secondary circuit cause non-sinusoidal magneto-motive force and this is called end effect and eddy current. In Figure 2,<sup>2-4</sup> these effects are modeled and simulated on the basis of mathematical model,<sup>5</sup> and finite element method 3D.<sup>6</sup>

---

\*Corresponding author.

Email: [truongminhtan@qnu.edu.vn](mailto:truongminhtan@qnu.edu.vn)

The content of the paper presents a dynamic model of a three-phase single-side linear induction motor (SLIM) used in elevators taking into account the components of end effects and eddy currents, thereby surveying the thrust and velocity responses when starting the system in the cases of no-load, load-carrying, variation of frequency and asymmetrical power supply. This can be considered as the basic foundation for the study of the SLIM to develop and implement an appropriate control model. The simulation method on Matlab software is used in this study.

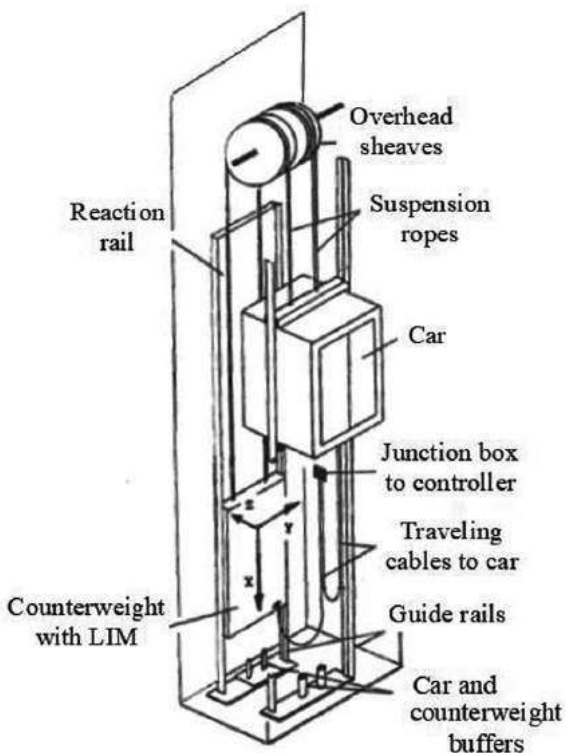


**Figure 1.** Passenger elevator model using the LIM

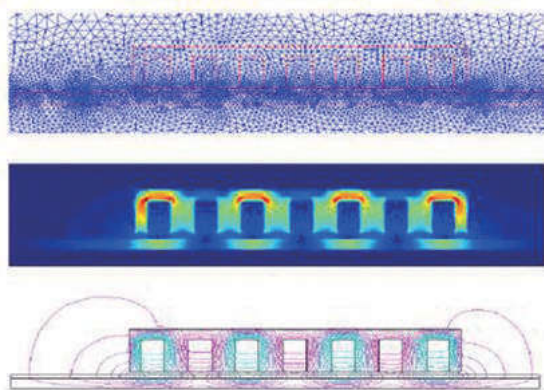


**Figure 2.** Flux density distribution inside the LIM

**2. SLIM MODEL TAKING INTO ACCOUNT THE COMPONENTS OF END EFFECT AND EDDY CURRENT**

Components reflect end effects:<sup>4</sup>  $L_m \cdot (1-f(\xi))$

with  $\xi = \frac{l \cdot R_r}{L_r \cdot v}$  và  $f(\xi) = \frac{1 - e^{-\xi}}{\xi}$  (1)

When the SLIM is moving, in the secondary side aluminum plate exists an eddy current component and causes loss.

$$P_{dx} = R_r \cdot I_\mu^2 \frac{1 - e^{-\xi}}{\xi} = I_\mu^2 R_r f(\xi) \quad (2)$$

The characteristic component for this loss is  $R_r f(\xi)$ , and it is connected in series in the magnetization branch as shown in Figure 3.

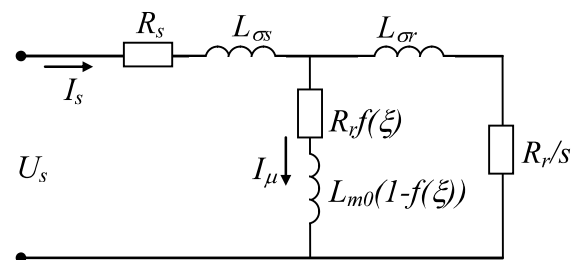


**Figure 3.** Equivalent circuit of LIM

On the  $\alpha\beta$  coordinate system. The dynamic model of the SLIM is described as follows:

$$\begin{cases} \frac{di_{s\alpha}}{dt} = -D'i_{s\alpha} + B'\psi_{r\alpha} + \frac{\pi}{\tau} vC\psi_{r\beta} + Au_{s\alpha} \\ \frac{di_{s\beta}}{dt} = -D'i_{s\beta} + B'\psi_{r\beta} - \frac{\pi}{\tau} vC\psi_{r\alpha} + Au_{s\beta} \\ \frac{d\psi_{r\alpha}}{dt} = F'i_{s\alpha} - E'\psi_{r\alpha} - \frac{\pi}{\tau} v\psi_{r\beta} \\ \frac{d\psi_{r\beta}}{dt} = F'i_{s\beta} - E'\psi_{r\beta} + \frac{\pi}{\tau} v\psi_{r\alpha} \\ F_e = \frac{3}{2} \frac{p}{2} \frac{\pi}{\tau} \cdot k_F \cdot (\psi_{r\alpha} i_{s\beta} - \psi_{r\beta} i_{s\alpha}) \\ \frac{dv}{dt} = m(F_e - F_L) \end{cases} \quad (3)$$

In there:

$$A = \frac{L_r - L_m \cdot f(\xi)}{(L_s - L_m f(\xi)) \cdot (L_r - L_m f(\xi)) - (L_m(1 - f(\xi)))^2}$$

$$B = \frac{R_r \cdot L_m (1 - f(\xi))}{(L_r - L_m f(\xi))} \cdot \frac{1}{L_s - L_m f(\xi) \cdot (L_r - L_m f(\xi)) - (L_m (1 - f(\xi)))^2}$$

$$C = \frac{L_m (1 - f(\xi))}{(L_s - L_m f(\xi)) \cdot (L_r - L_m f(\xi)) - (L_m (1 - f(\xi)))^2}$$

$$B' = \left[ \frac{R_r \cdot f(\xi) - \frac{L_m (1 - f(\xi))}{L_r - L_m f(\xi)} (R_r + R_r f(\xi))}{1} \right] \cdot \frac{1}{L_s - L_m f(\xi) \cdot (L_r - L_m f(\xi)) - (L_m (1 - f(\xi)))^2}$$

$$D = \frac{R_s \cdot (L_r - L_m f(\xi))^2 + R_r \cdot (L_m (1 - f(\xi)))^2}{(L_r - L_m f(\xi))} \cdot \frac{1}{L_s - L_m f(\xi) \cdot (L_r - L_m f(\xi)) - (L_m (1 - f(\xi)))^2}$$

$$D' = \left[ \frac{R_s + R_r f(\xi) - \frac{2 \cdot R_r f(\xi) \cdot L_m (1 - f(\xi))}{L_r - L_m f(\xi)} + \frac{(R_r + R_r f(\xi)) \cdot (L_m (1 - f(\xi)))^2}{(L_r - L_m f(\xi))^2} \right] \cdot \frac{1}{L_r - L_m f(\xi)} \cdot \frac{1}{(L_s - L_m f(\xi)) \cdot (L_r - L_m f(\xi)) - (L_m (1 - f(\xi)))^2}$$

$$E = \frac{R_r}{L_r - L_m \cdot f(\xi)}; E' = \frac{R_r + R_r f(\xi)}{L_r - L_m \cdot f(\xi)}$$

$$F = \frac{R_r \cdot L_m (1 - f(\xi))}{L_r - L_m \cdot f(\xi)}$$

$$F' = \frac{(R_r + R_r f(\xi)) \cdot L_m (1 - f(\xi))}{L_r - L_m \cdot f(\xi)} - R_r f(\xi)$$

Thrust coefficient:  $k_F = \frac{L_m (1 - f(\xi))}{L_r - L_m f(\xi)} \quad (4)$

$$F_e = m \dot{v} + nv + F_L \quad (5)$$

$$L_m = 3L_{m0}/2; L_s = L_m + L_{\sigma s}; L_r = L_m + L_{\sigma r} \quad (6)$$

Here:  $R_s(R_r)$ ,  $L_s(L_r)$  - resistance and inductance components of the primary (secondary);  $L_{\sigma s}(L_{\sigma r})$  - dissipation inductance of primary (secondary) part;  $L_m$  - mutual inductance between primary and secondary;  $L_{m0}$  - maximum mutual inductance between primary and secondary;  $u_{s\alpha}$ ,  $u_{s\beta}$  - components along the  $\alpha$  and

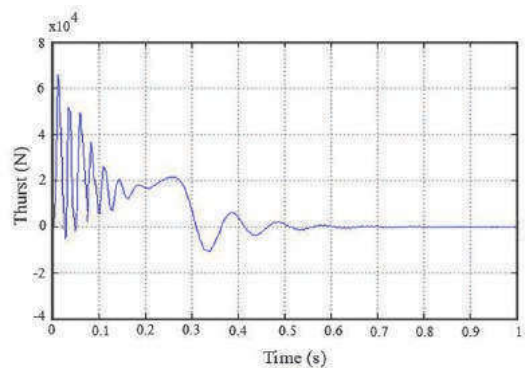
$\beta$  axes of the voltage vector;  $i_{s\alpha}$ ,  $i_{s\beta}$  - components along the  $\alpha$  and  $\beta$  axes of the current vector;  $\psi_{r\alpha}$ ,  $\psi_{r\beta}$  - components along the  $\alpha$  and  $\beta$  axes of the flux vector of secondary part;  $v$  - velocity of primary part;  $F_e$  - electromagnetic thrust of the motor;  $F_L$  - load force;  $m$  - mass;  $n$  - coefficient of friction;  $l$  - primary part length.

### 3. DYNAMIC CHARACTERISTICS OF THREE-PHASE SINGLE-SIDE LINEAR INDUCTION MOTOR USED IN ELEVATOR

Simulation is performed on Simulink/Matlab with the parameters of the SLIM applied in the elevator:<sup>7</sup> Rated line voltage 400 V;  $I_{ldm} = 201.6$  A;  $F = 16$  kN;  $f = 50$  Hz; velocity 10 m/s;  $a = 2$  m/s<sup>2</sup>, total weight of cabin and bearing  $m_{cabin} = 500$  kg; Number of passenger in one cabin 5 and average weight of each passenger 75 kg;  $s_{dm} = 10\%$ ;  $R_s = 0.00356 \Omega$ ;  $R_r = 0.2055 \Omega$ ;  $X_s = 0.1371 \Omega$ ;  $X_m = 1.1795 \Omega$ .

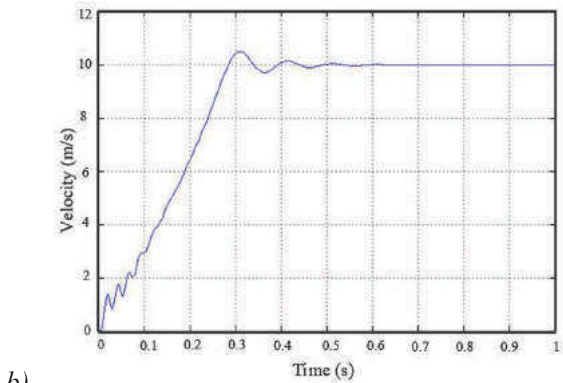
#### 3.1. In case of no-load:

The primary or stator moves along the secondary of a SLIM and no-load (cabin, passenger), the thrust, velocity, stator current responses as shown in Figures 4 and 5. The obtained results show that factors such as end effects and eddy currents have a great influence on the dynamic characteristics of the SLIM. The maximum transient thrust value in the case of the end effect and eddy current is only 58 kN (decreased by 4.13%) and the maximum thrust value is 18 kN (decreased by 12.19%) compared to not considered. The value of the maximum current amplitude in the first cycle is slightly changed. Start-up time is longer.

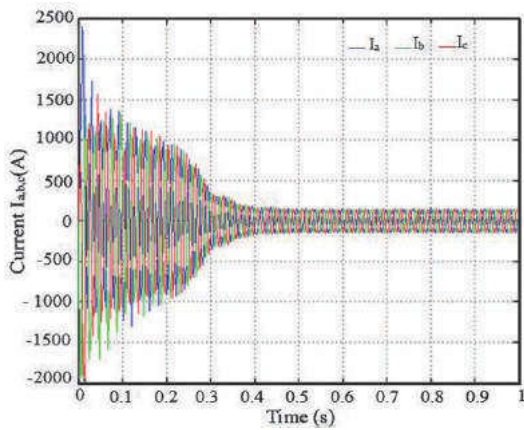


a)



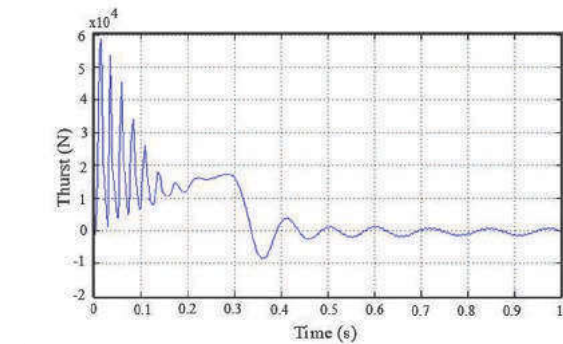


b)

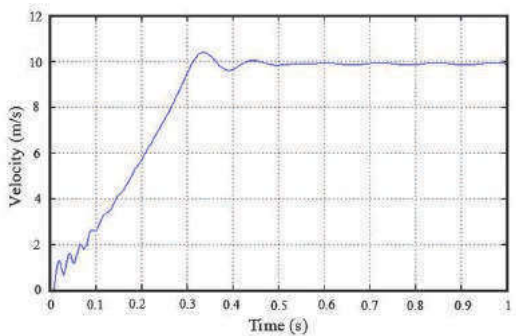


c)

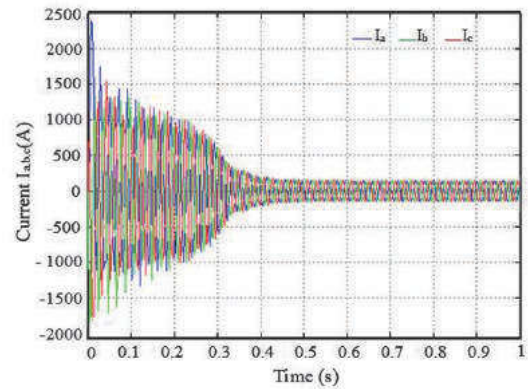
**Figure 4.** Thrust response a) velocity b) stator current c) at no-load in the absence of end effect and eddy current



a)



b)



c)

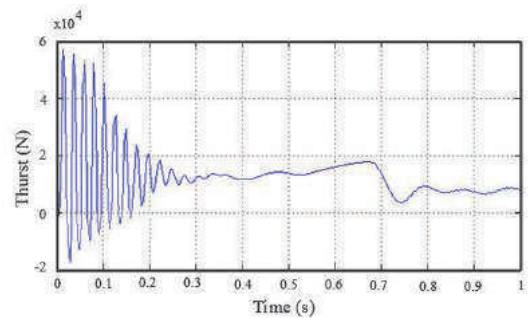
**Figure 5.** Thrust response a) velocity b) stator current c) at no load in the case of end effect and eddy current

During the operation of SLIM, end effect and eddy currents phenomena always occur simultaneously, causing synergistic effects on dynamic characteristics. Therefore, the investigation of the characteristics in the following cases is carried out on the model that takes this phenomenon into account.

**3.2. In case of load-carrying:**

The primary part moves along the secondary and the full load (cabin and passenger) and load 57.14% (cabin and no passenger).

When starting the SLIM with a large load, the start-up time is prolonged. For example, the starting time at full load is 0.7 s which is larger than 0.3 s with load 57.14%. Note that starting the SLIM with a large load will be very difficult, even if it doesn't start, the load force of the elevator belongs to the type of energy of potential force, the motor can be pulled back at the moment the force reaches its minimum value. The maximum transient thrust value as well as the maximum thrust value are not changed when changing the load force.



a)

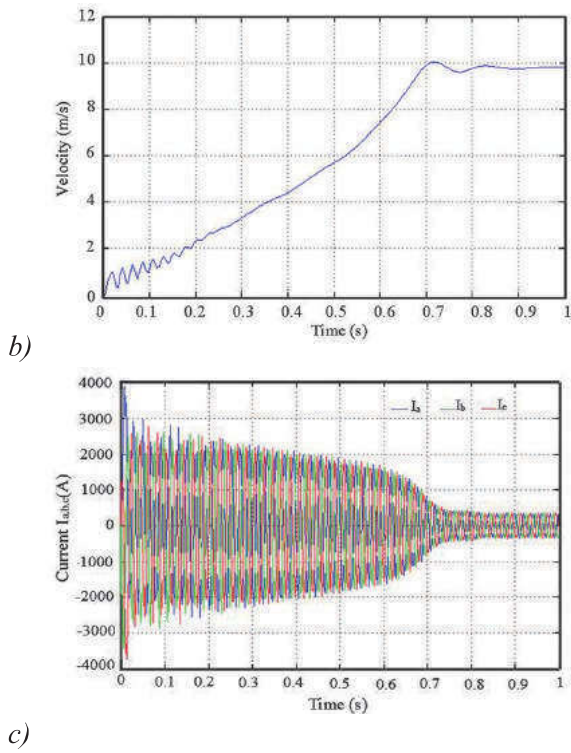


**Figure 6.** Thrust response a) velocity b) stator current c) at full load

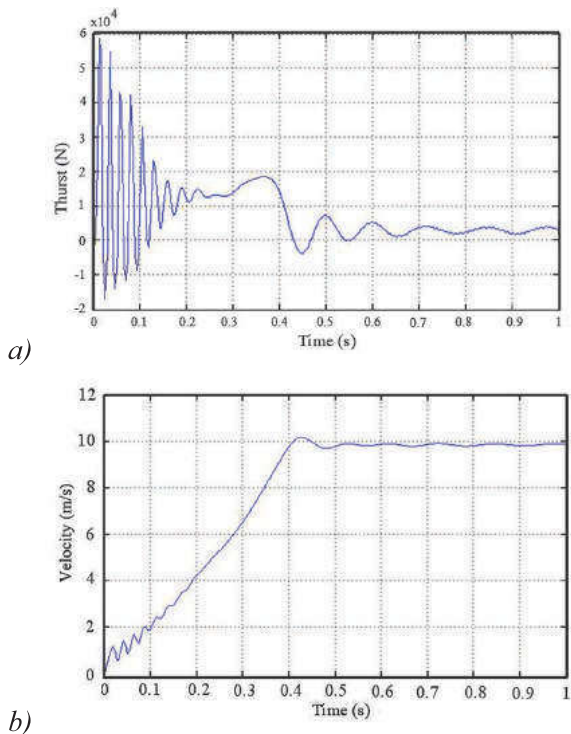


**Figure 7.** Thrust response a) velocity b) at load 57,14%

**3.3. In case of power supply frequency reduced by 1%:**

Investigate the dynamic characteristics of the motor in case the power supply frequency is

reduced by 1% (49.5 Hz) compared to the 50 Hz power frequency as shown in Figure 8. The speed of the motor is reduced, the maximum transient force value in this case is 61 kN (increase of 3.28%) and the maximum thrust value is 20.5 kN (increase of 4.88%) compared to the case of Figure 6 (59 kN and 19.5 kN) this can be explained that the effect of end effect phenomenon in the SLIM is also reduced in the working area of lower speed.

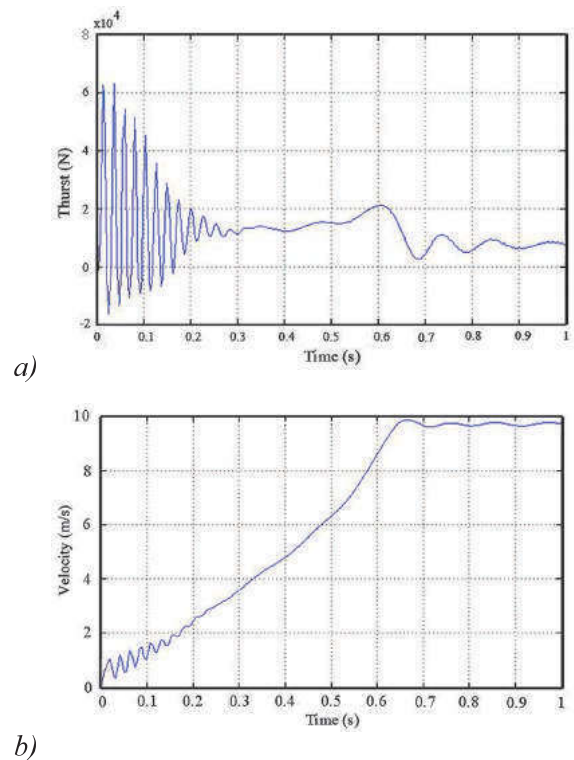


**Figure 8.** Thrust response a) velocity b) at full load and power supply frequency reduced by 1%

**3.4. In case of asymmetrical power supply:**

Considering another case related to the symmetry of the power supply for the motor, the phase A voltage is reduced by 5% compared to the remaining 2 phase voltage. The results in Figure 8 shows that the current in phase A has a larger amplitude than the other two phases, the start up time is extended to 0.8 s and the thrust and speed response fluctuate at steady state, which can cause “jerk” when operating the elevator system.

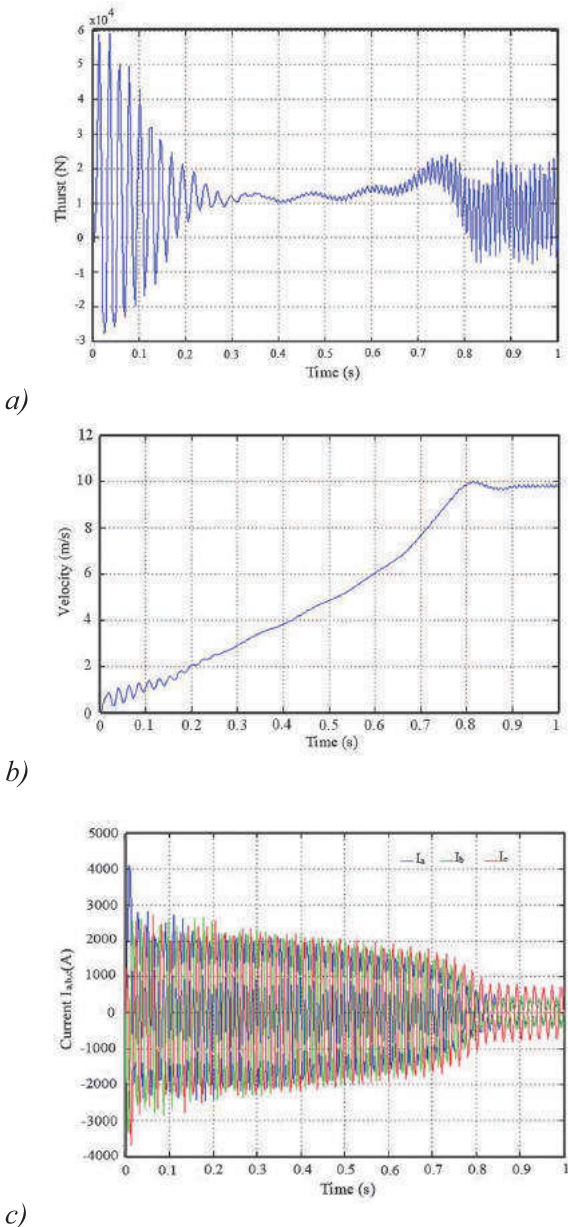


**Figure 9.** Thrust response a) velocity b) stator current c) at full load and asymmetrical power supply

**4. CONCLUSION**

- End effect and eddy current in the SLIM have a certain influence on the working state of the motor, reduce the magnitude of the thrust, and change the shape of the dynamic thrust characteristics single - side linear induction motor.

- The dynamic characteristics of the SLIM are considered in the following cases: no load, low load, full load, variable frequency, and asymmetrical voltage source. The results show

that the dynamic characteristics change with the changes of the working state of the motor.

- The issue of using a SLIM for the passenger elevator drive system has opened up the prospect for the application of this motor to loads of potential energy nature. The system attains the criteria of velocity, fast response time as well as safety requirements when operating.

- In present practice, the motor velocity regulation is usually combined with the inverter, and the dynamic characteristics of the motor in this case need to be further studied.

**REFERENCE**

1. J. F. Gieras, E. Gagnon. Innovative elevator drive with a linear induction motor, *University of Technology and Life Sciences in Bydgoszcz*, **1992**, 150-155.
2. Truong Minh Tan, Nguyen The Cong, Le Van Doanh, Phung Anh Tuan. Algorithm to design single sided linear induction motor thrust optimization, *Journal of Science Technology Technical Universities*, **2009**, 70, 1-5.
3. J. F. Gieras. *Linear induction drives*, Oxford University Press, Inc., New York, 1994.
4. J. Duncan and C. Eng. Linear induction motor equivalent circuit model, *Proc. IEE*, **1983**, 130(1), 51-57.
5. M. N. Raju, M. S. Rani. Mathematical modelling of linear induction motor, *International Journal of Engineering & Technology*, **2018**, 4(24), 111-114.
6. J. A. D. Hernández, N. D. Carralero, E. G. Vázquez. A 3-D simulation of a single-sided linear induction motor with transverse and longitudinal magnetic flux, *Applied Sciences MPDI*, **2020**, 10(7004), 1-26.
7. A. M. Mhway, N. W. Aung, M. N. Y. Tun. Design of single-sided linear induction motor used in elevator, *International Journal of Science and Engineering Applications*, **2018**, 7(10), 386-390.



# Vận hành tối ưu hệ thống năng lượng (điện - gas) có xét đến năng lượng mặt trời, gió và hệ thống tích trữ trên cơ sở mô hình Energy Hub

Hà Thanh Tùng<sup>1,\*</sup>, Phạm Thị Hồng Anh<sup>2</sup>, Phạm Thị Ngọc Dung<sup>1</sup>

<sup>1</sup>Trường Đại học Kỹ thuật Công nghiệp - Đại học Thái Nguyên, Việt Nam

<sup>2</sup>Trường Đại học Công nghệ thông tin và Truyền thông - Đại học Thái Nguyên, Việt Nam

Ngày nhận bài: 23/03/2021; Ngày nhận đăng: 05/05/2021

## TÓM TẮT

Trong bài báo này, trung tâm năng lượng (Energy Hub) được xem như là một siêu nút kết nối giữa điện năng, khí tự nhiên, mặt trời và gió; sau đó thông qua các thiết bị chuyển đổi và hệ thống tích trữ năng lượng để đáp ứng nhu cầu sử dụng điện, nhiệt, và làm mát của phụ tải. Ngôn ngữ lập trình bậc cao GAMS được sử dụng để giải quyết vấn đề vận hành tối ưu mạng năng lượng (Energy Network - EN) với hàm mục tiêu tổng chi phí sử dụng năng lượng và phát thải nhà kính ( $\text{NO}_2$ ,  $\text{SO}_2$  và  $\text{CO}_2$ ) nhỏ nhất. Ảnh hưởng của nguồn năng lượng phân tán, hệ thống tích trữ đến hiệu quả vận hành EN được đánh giá thông qua 04 kịch bản vận hành khác nhau. So sánh với hình thức cung cấp năng lượng điện truyền thống, kết quả tính toán cho thấy mô hình đề xuất đã làm thay đổi đáng kể đường đặc tính năng lượng điện và khí tự nhiên mua từ hệ thống; tăng hiệu quả khai thác và sử dụng tối ưu năng lượng so với hình thức cung cấp năng lượng chỉ sử dụng duy nhất một dạng năng lượng điện.

**Từ khóa:** Khí tự nhiên, điện năng, mạng năng lượng, vận hành tối ưu, hệ thống tích trữ.

\*Tác giả liên hệ chính.

Email: tunganh@tnut.edu.vn

# Optimal operation of the energy network (electricity - gas) considering solar, wind, and energy storages system based on energy hub modeling

Ha Thanh Tung<sup>1,\*</sup>, Pham Thi Hong Anh<sup>2</sup>, Pham Thi Ngoc Dung<sup>1</sup>

<sup>1</sup>Thai Nguyen University of Technology, Vietnam

<sup>2</sup>Thai Nguyen University of Information and Communication Technology, Vietnam

Received: 23/03/2021; Accepted: 05/05/2021

## ABSTRACT

In this paper, the Energy Hub (EH) is considered as a super-node connecting different forms of energy including electricity, natural gas, solar energy, and wind energy; then through conversion equipment and energy storage systems meets the demand for electricity, heat, and cooling of small loads. GAMS is used to solve the optimal operation problem of Energy Network (EN) with the objective of minimizing the cost of energy and greenhouse emission (NO<sub>2</sub>, SO<sub>2</sub> and CO<sub>2</sub>). The effect of distributed energy, and energy storage systems on the performance of EN is assessed through four different operating scenarios. Compared to traditional electricity supply, the results showed that EN dramatically changed the characteristics of electricity consumption line chart and natural gas purchased from the system; thus, increasing efficiency and optimal use of energy compared to the conventional architecture of using a single energy source.

**Keywords:** Natural gas, electricity, energy network, Optimal operation, Energy storages.

## 1. INTRODUCTION

Depletion of energy resources and pressure of environmental pollution are two big problems for scientists. Nowadays, instead of using single energy systems,<sup>1</sup> combined energy systems are receiving strong attention.<sup>2,3</sup> The introduction of Energy Network (EN) concept<sup>4-6</sup> is considered a breakthrough to improve reliability, reduce pollution and encourage the development of energy systems. It also improves stability, and achieve the goal of economical and efficient use of energy.

Energy hub (EH)<sup>1</sup> is a model that has attracted the attention of researchers. EH is considered a multi-purpose system that combines

capacity and load through a converter system.<sup>7-8</sup> Studies<sup>9-11</sup> address the problems of combining different energy forms through this model. In general, EH allows optimal connectivity between types of energy, considering storage devices, distribution sources, electric vehicles, etc.

Along with the establishment and development of EN and EH, renewable energy and energy storage technology are two solutions that continue to be researched and developed extensively to confront increasing pressure from society's demand. The traditional form of energy distribution through the electricity system has proved significant efficiency of these two groups in terms of operation and energy saving.<sup>12</sup>

---

\*Corresponding author.

Email: tunganh@tnut.edu.vn

The evaluation of the efficiency of renewable energy and Energy Storage System (ESS) to the independent EH optimal operation problem was introduced in studies.<sup>13-15</sup> However, for the EN model constructed from several EHs, their role and impacts have not been fully addressed. The operation problem has only been solved on the side of calculating the optimal capacity among EHs without calculating and comparing the efficiency between the energy network (electricity, heat, natural gas...) and traditional power network.

In large areas, the EN has to supply a lot of loads. As a result, many EHs are connected on a large scale by distribution networks to provide energy to consumers. This paper focuses on solving the following three problems: (1) *Simultaneously analyse operational cost optimization problems in EH-using networks and the use of renewable resources in storage and distribution networks;* (2) *Ensure optimal network operation in all situations by considering the operational parameters and energy losses of both electricity and natural gas distribution networks;* (3) *Assess the impact of energy sources and storage devices on EN performance by comparing system energy consumption and emissions across four operating scenarios.*

The 22 kV distribution grid with 6 load nodes is the basis for the formation of EN. four scenarios considered include independent network operation and optimal operation of EN with the participation of solar, wind and ESS energy. The approach and solution to the problem are as follows: The energy center model (including concept, structure, mathematical description), energy balance problem and EN system structure will be introduced in part 2. Part 3 develops an optimal operation problem for EN with the objective function of minimizing energy costs and emission costs (SO<sub>2</sub>, NO<sub>2</sub> and CO<sub>2</sub>). Part 4 addresses the optimal operation problem using GAMS. Micro Energy Networks (MEN) optimization problem is considered with four different configurations to simultaneously meet the heat, electricity and cooling needs of 6 load

nodes. The conclusion and suggestion for further research are presented in section 5.

**2. ENERGY HUB & ENERGY NETWORK**

**2.1. Mô hình EH**

The concept and structure of EH were introduced in study.<sup>16</sup> In general, EH is considered a node in an energy network with multiple inputs and outputs. The energy centers are described in Figure 1. In which, P, L denote the input and output energy of the respective energy forms. The EH model is used with n converters corresponding to efficiency  $\eta_1, \eta_2 \dots$  to  $\eta_n$ .

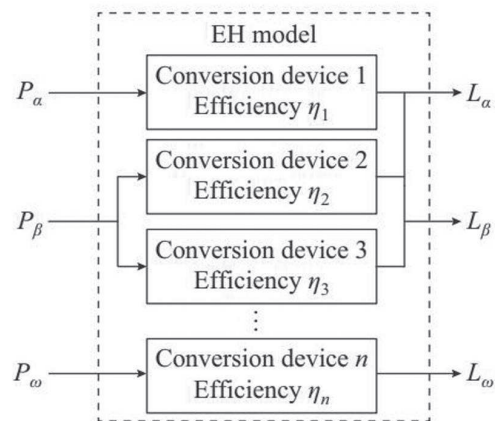


**Figure 1.** General structure of EH

**2.2. Energy Network model**

EN is an extensive definition of the power grid that combines natural gas and other forms of energy (Figure 2). Its advantages are (1) Promote applications of new and renewable energy sources; (2) Lower energy costs, emissions and load peaks while flexibly responding to load diversity; (3) Promote diversified and sustainable development of energy technology.

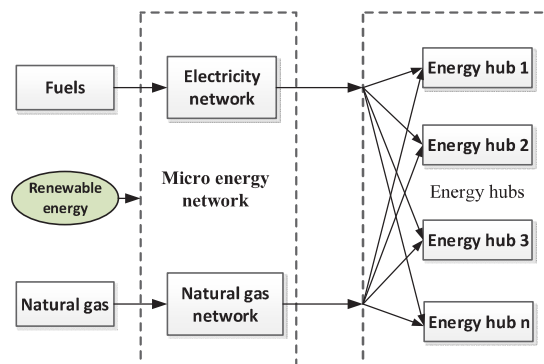


**Figure 2.** General structure of EN

With the mentioned advantages, the research analyzes and proposes a model consisting of several EHs to link the electricity and natural gas networks with the structure as shown in Figure 2.

The power distribution of the power network can be through the basic node power balance equation:

$$\begin{cases} Q_{E,i}^G = Q_{E,i}^D + V_i \sum_{j=i}^{n_E} V_j (G_{E,ij} \cos \theta_{ij} + B_{E,ij} \sin \theta_{ij}) \\ P_{E,i}^G = P_{E,i}^D + V_i \sum_{j=i}^{n_E} V_j (G_{E,ij} \cos \theta_{ij} + B_{E,ij} \sin \theta_{ij}) \end{cases} \quad (1)$$

In which  $P_{E,i}^G(t)$ ,  $Q_{E,i}^G$  represent active and reactive power of the generator flows into the  $i$ -th node;  $P_{E,i}^D(t)$ ,  $Q_{E,i}^D$  represent the active and reactive power of the electrical load at node  $i$ .  $V_i$ ,  $V_j$  are the voltage values at node  $i$  and node  $j$ .  $G_{E,ij}$ ,  $B_{E,ij}$ , and  $\theta_{ij}$  are the active inductance, reactive inductance of the conductor, and phase difference from node  $i$  to  $j$  respectively.  $n_e$  is the number of nodes in the power network.

The natural gas network is supplied from gas plants or natural gas supply companies through pipelines, compressors and valve systems. The air flow in the gas line can be calculated according to the document:<sup>17,18</sup>

$$f_{ij}^L = k_{ij}^L \text{sign}(p_i, p_j) \sqrt{\text{sign}(p_i, p_j) (p_i^2 - p_j^2)} \quad (2)$$

Where, they are the natural gas flow rate and the coefficient of gas pipes from point  $i$  to  $j$ , respectively,  $p_i$ ,  $p_j$  are the gas pressure at points  $i$  and  $j$ , respectively.

In the above Equation (2),  $\text{sign}(p_i, p_j)$  represents the flow direction in the gas pipeline. The specific value is determined by Formula (3) as follows:

$$\text{sign}(p_i, p_j) = \begin{cases} +1, & \text{if } p_i > p_j \\ -1, & \text{else} \end{cases} \quad (3)$$

Natural gas flow can be calculated based on the gas flow in the pipeline and the Gross Heating Value (GHV) of the gas according to the expression:

$$\begin{cases} P_{G,ij}^L = GHV \times f_{ij}^L \\ P_{G,ij}^C = GHV \times f_{ij}^C \end{cases} \quad (4)$$

Where,  $P_{G,ij}^L$ ,  $P_{G,ij}^C$  are the capacity of natural gas and pump pressure from point  $i$  to point  $j$ , respectively;  $K_{ij}^C$  is the compressor constant;  $f_{ij}^L$  is the natural gas flow from point  $i$  to  $j$ ;  $f_{ij}^C$  is the pressure pump loss from point  $i$  to  $j$ . Then the gas balance equation is written as mathematical formula (5) as follows:

$$P_{G,i}^S = P_{G,i}^D + \sum_{j=1}^{n_g} P_{G,ij}^C + \sum_{j=1}^{n_g} P_{G,ij}^L \quad (5)$$

$P_{G,i}^S$  is the capacity of natural gas flowing into point  $i$ .  $P_{G,i}^D$  is the natural gas power consumed at point  $i$ .  $n_g$  is the number of nodes of the natural gas network.

### 3. OPTIMAL MODEL

#### 3.1. Proposed EH model

This study proposes an EN model as shown in Figure 3. EN is formed on the basis of a distribution grid (voltage level 22 kV), scale to meet the demand for electricity, heat and cool energy for 06 nodes load. The natural gas network and the electricity network are connected through EHs. Within the scope of the research model, applications from solar energy (can be exploited in the form of electricity through the solar thermal system and electricity through the photovoltaic battery system), wind power and electric ESS, heat, and cool are provided in the EH hubs. The energy storage system plays the role of storing and transmitting according to the optimal operating mode of MEN.

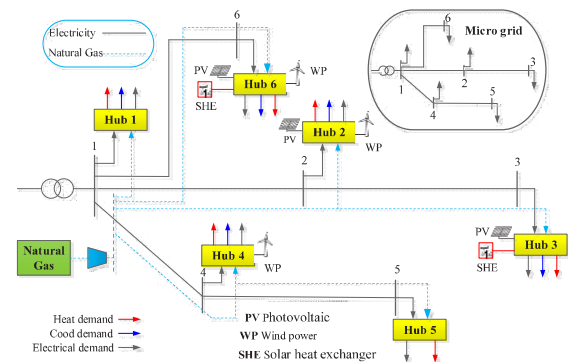


**Figure 3.** Proposed EN model



**3.2. EH structure**

A general EH structure consisting of 12 devices is proposed in Figure 4. In which, the source group includes: electricity distribution system, natural gas system, distributed source (wind energy and solar energy); The group of conversion equipment includes: voltage transformer, Micro turbine (MT), Air Conditioned (AC), Gas boiler (GB), Absorption Chiller (ACh), solar heat exchanger (SHE) and Electric heater (EHe). The group of storage systems includes: Energy storage devices (Energy storage ES), thermal storage devices (Thermal Storage TS) and Ice storage-IS. Energy demand includes electricity, heat and cooling loads.

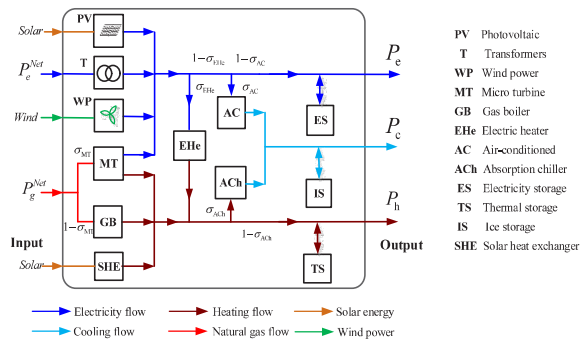


**Figure 4.** EH model structure

The relationship between input/output energy of the general EH model at the  $n^{th}$  node is rewritten as mathematical formula (6).

$$\begin{aligned}
 L_{e,n}(t) &= \left[ P_{e,n}(t)\eta_{e,n}^T + P_{g,n}(t)v_{MT,n}(t)\eta_{ge,n}^{MT} + P_{e,n}^{WP}(t) + P_{e,n}^{PV}(t) \right] \\
 &\quad \times \left( 1 - v_{EHe,n}(t) \right) \left( 1 - v_{AC,n}(t) \right) + \left( P_{ES,n}^{dis}(t) - P_{ES,n}^{ch}(t) \right) \\
 L_{h,n}(t) &= \left[ \left( P_{g,n}(t) \left( v_{MT,n}(t)\eta_{gh,n}^{MT} + (1 - v_{MT,n}(t))\eta_{h,n}^{GB} \right) + P_{h,n}^{SHE}(t) \right) + \right. \\
 &\quad \left. + \left( P_{e,n}(t)\eta_{e,n}^T + P_{g,n}(t)v_{MT,n}(t)\eta_{ge,n}^{MT} + P_{e,n}^{WP}(t) + P_{e,n}^{PV}(t) \right) \eta_{h,n}^{EHe} v_{EHe,n}(t) \right] \\
 &\quad \times \left( 1 - v_{ACh,n}(t) \right) + \left( P_{HS,n}^{dis}(t) - P_{HS,n}^{ch}(t) \right) \\
 L_{c,n}(t) &= \left[ \left( P_{g,n}(t) \left( v_{MT,n}(t)\eta_{gh,n}^{MT} + (1 - \sigma_{MT,n}(t))\eta_{h,n}^{GB} \right) + P_{h,n}^{SHE}(t) \right) + \right. \\
 &\quad \left. + \left( P_{e,n}(t)\eta_{e,n}^T + P_{g,n}(t)v_{MT,n}(t)\eta_{ge,n}^{MT} + P_{e,n}^{WP}(t) + P_{e,n}^{PV}(t) \right) \eta_{h,n}^{EHe} v_{EHe,n}(t) \right] v_{ACh,n}\eta_{h,n}^{ACh} \\
 &\quad + \left[ P_{e,n}(t)\eta_{e,n}^T + P_{g,n}(t)v_{MT,n}(t)\eta_{ge,n}^{MT} + P_{e,n}^{WP}(t) + P_{e,n}^{PV}(t) \right] \times \\
 &\quad \left( 1 - v_{EHe,n}(t) \right) v_{AC,n}(t)\eta_{e,n}^{AC} + \left( P_{CS,n}^{dis}(t) - P_{CS,n}^{ch}(t) \right)
 \end{aligned} \tag{6}$$

**3.3. Mathematical model**

**3.3.1. Objective function**

The optimal operation problem EN with the proposed objective function is the total cost of energy (the cost of purchasing electricity and natural gas from the system and the total cost of  $CO_2$ ,  $SO_2$ , and  $NO_2$  emissions of the MT and GB equipment for a period of 1 day (24 hours)) is the smallest:

$$\text{Min} \sum_{t=1}^{24} \left[ P_{\sum_e}(t)c_e^{Net}(t) + P_{\sum_g}(t)c_g^{Net}(t) + C_{MT} + C_{GB} \right] \tag{7}$$

$$C_{MT} = \left( \sum_{n=1}^6 \sum_{em}^3 c_{em} EF_{em}^{MT} P_{g,n}^{MT}(t) \right); C_{GB} = \left( \sum_{n=1}^6 \sum_{em}^3 c_{em} EF_{em}^{GB} P_{g,n}^{GB}(t) \right)$$

In Eq (7),  $P_{\sum_e}(t)$ ,  $P_{\sum_g}(t)$ ,  $P_{\sum_g}(t)$  are the total energy including electricity and natural gas purchased from the respective external system at time  $t$ ;  $EF_{em}^{MT}$ ,  $EF_{em}^{GB}$  are the emission factors of MT and GB, respectively.

**3.3.2. Mathematical constraints**

**a. Transmission power limit**

System limitations include limits on active

power, reactive power and node voltage in the grid. The pressure and compression ratio in the natural gas network are as follows:

$$\begin{cases} p_{ck}^{\min} \leq p_{ck} \leq p_{ck}^{\max} \\ p, V_i^{\min} \leq p, V_i \leq p, V_i^{\max} \\ P, Q_{E,i}^{G,\min} \leq P, Q_{E,i}^G \leq P, Q_{E,i}^{G,\max} \end{cases} \quad (8)$$

**b. Technical limits of EH**

The constraint of energy balance for the corresponding EH at the  $n^{th}$  node is introduced in part 2 by the mathematical Formula (6). Other constraints include: Limiting the input power of electricity and natural gas at the  $n^{th}$  center; the mathematical formula (9) expresses the transition limits for AC, MT, ACh and EHe according to the state variable  $v_{AC,n}(t), v_{MT,n}(t), v_{ACh,n}(t), v_{EHe,n}(t)$  at time  $t$  of the  $n$ -th center respectively.

$$\begin{cases} \sigma_{AC}(t), \sigma_{MT}(t), \sigma_{ACh}(t), \sigma_{EHe}(t) \in [0, 1] \\ P_{e-g,n}(t) \leq P_{e-g,n}^{\max} \end{cases} \quad (9)$$

**c. Energy Storage System - ESS**

The system of energy storage devices in EN uses three types of storage devices simultaneously: ES, TS, and IS respectively at the  $n^{th}$  EH. Primarily, the principle of discharge and its effects are the same. Considering each  $n^{th}$  EH at the  $t$ -th hour of the day, the energy storage system is investigated through the charging process and the corresponding energy loss factor  $\rho_{e,h,c-n}^{ES,TS,CS-loss}$ :

$$\begin{cases} \psi_{ES,TS,IS}^{ch,dis}(n)(t) P_{ES,TS,IS}^{ch,dis}(n)(t) > 0 \Leftrightarrow \psi_{ES,TS,IS}^{ch}(n)(t) = 1 \\ \psi_{ES,TS,IS}^{dis}(n)(t) + \psi_{ES,TS,IS}^{ch}(n)(t) = 1 \\ \psi_{ES,TS,IS}^{dis}(n)(t) \times \psi_{ES,TS,IS}^{ch}(n)(t) = 0 \\ 0 \leq P_{ES,HS,CS}^{ch,dis}(n)(t) \leq P_{ES,HS,CS}^{ch,dis-Max}(n) \\ P_{e,h,c}^{ES,TS,CS-loss}(t) = \rho_{e,h,c}^{ES,TS,CS-loss} P_{e,h,c}^{ES,HS,CS}(t) \\ P_{e,h,c}^{ES,HS,CS-Min} \leq P_{e,h,c}^{ES,HS,CS}(t) \leq P_{e,h,c}^{ES,HS,CS-Max} \\ P_{e,h,c}^{ES,HS,CS}(t) = P_{e,h,c}^{ES,HS,CS}(t-1) + P_{ES,HS,CS}^{ch}(n)(t) - P_{ES,HS,CS}^{dis}(n)(t) - P_{ES,HS,CS}^{loss}(n)(t) \end{cases} \quad (10)$$

Constraint on energy balance in calculation cycle  $T=24$  hours (due to the characteristic of discharge power that often repeats on a 1-day cycle):

<https://doi.org/10.52111/qnjs.2021.15303>

$$P_{e,h,c}^{ES,HS,CS}(0) = P_{e,h,c}^{ES,HS,CS}(T) \quad (11)$$

**d. Energy price**

Energy price including electricity and gas prices is the determining factor of the objective function (9). Where the price of natural gas is constant<sup>18</sup> introduced in Expression (12). The electricity tariff is determined according to the Time-Of-Use (TOU) tariff.<sup>17</sup>

$$c_g^{Net}(t) = \text{const} \quad [\$/\text{kWh}] \quad (12)$$

**4. CALCULATION RESULTS**

Four different operating scenarios (OS) for EN are proposed in Table 2 to assess the role and impact of renewable energy (solar and wind) and ESS on model performance as follows:

**Table 1.** Operating scenarios

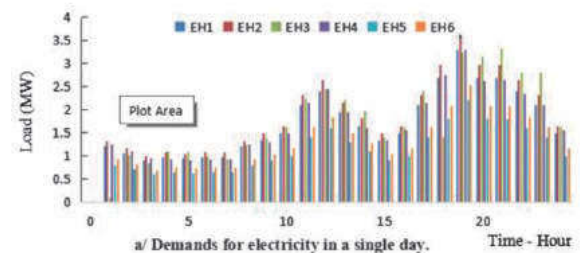
OS	Electricity network	Natural gas network	Solar wind	ESS (ES, HS, CS)
1	✓			
2	✓	✓		
3	✓	✓	✓	
4	✓	✓	✓	✓

**4.1. Calculation data**

The parameters for EN are as follows: the limited power from the power system through the transformer is 20 MVA, the rated voltage is 22 kV. The allowable voltage is [0.9-1.1]. The natural gas system has a nominal capacity of 20 MW for EN. The base pressure of the natural gas network is 10 bar.

**4.1.1. Load data**

Load parameters including power, heat and cooling demand based on<sup>7,8</sup> are as follows:



<https://doi.org/10.52111/qnjs.2021.15303>

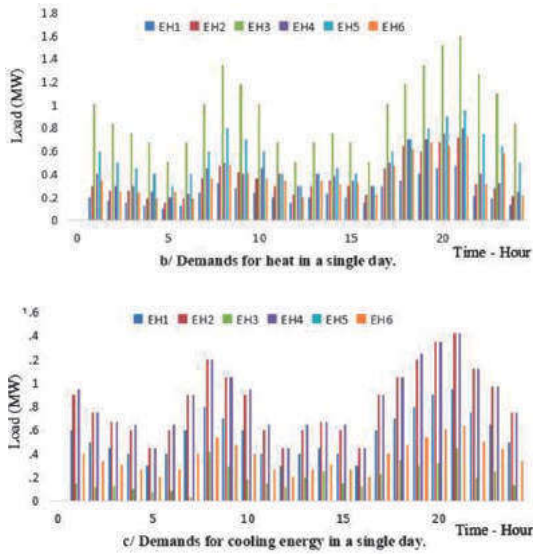


Figure 5. Demand for energy consumption

4.1.2. Energy price

Real-time energy prices are shown in Figure 6, where electricity prices are determined according to the TOU tariff<sup>17</sup> while natural gas prices are assumed to be constant.<sup>18</sup>

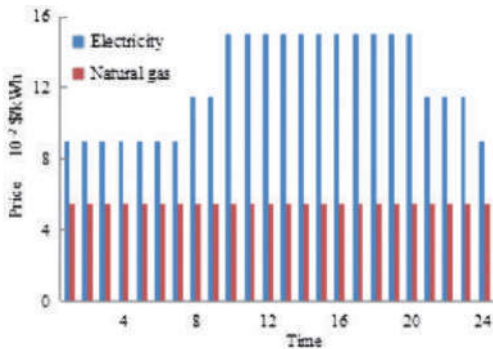


Figure 6. Prices of electricity and natural gas

4.1.3. System parameters

The parameters of 06 HubEH are presented in Table 2, the parameters of electricity and natural gas networks in Table 3:

Table 2. EH parameters

$T_{\mu_e}$	$\mu_{ge}^{MT}$	$\mu_{gh}^{MT}$	$P_h^{HS-max}$ (MWh)	$\rho_h^{HS,-loss}$ (MW)	$\mu_h^{HS}$ (MW)
0.95	0.4	0.5	4.2	0.02	0.96
$P_{ES}^{dis-max}$ (MW)	$P_e^{ES-min}$ (MW)	$P_c^{ES-max}$ (MWh)	$\eta_{h,n}^{EH_e}$	$P_{ES}^{ch-max}$ (MW)	$P_{HS}^{dis-max}$ (MW)
0.45	0.05	4.2	0.90	0.45	0.45
$\mu_h^{GB}$	$\mu_h^{ACh}$	$\mu_e^{AC}$	$\rho_e^{ES-loss}$	$\mu_e^{ES}$	$P_{HS}^{ch-max}$ (MW)
0.9	0.85	0.8	0.02	0.93	0.45

Table 3. Parameters of Electricity and Natural Gas Networks

Electricity network					Fuel gas heating value
Line	$R_E$ ( $\Omega$ )	$X$ ( $\Omega$ )	$B_E$ ( $10^{-3}S$ )	$L$ km	$k$
1-2	0.096	0.108	0.130	1.2	7
2-3	0.072	0.081	0.0972	0.9	9
1-4	0.12	0.135	0.162	1.5	6
4-5	0.084	0.0945	0.1134	1.5	8
1-6	0.144	0.162	0.1944	1.8	5

4.1.4. Distributed sources

The distribution characteristics of PV, SHE and WP in a typical day are shown in Figure 7.

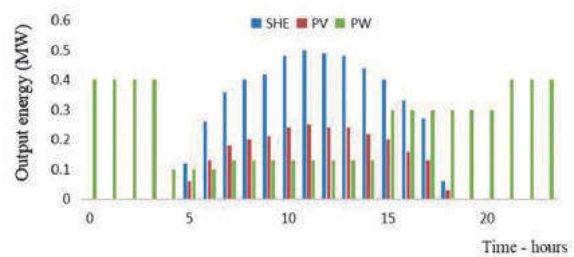
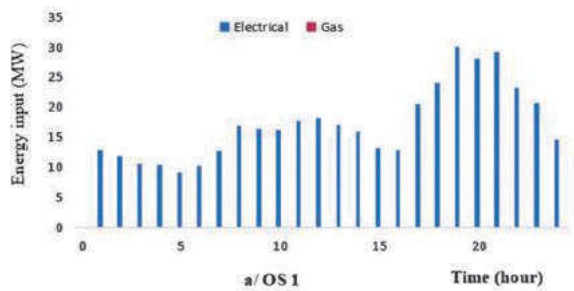


Figure 7. Transmit power of distributed sources

4.2. Optimal calculation results

The GAMS (MINOS) programming language<sup>19</sup> is used to compute the EN optimization with the objective function (7) and the constraints from (1) to (12). Calculation results for optimal operation with four different scenarios are presented in Table 4.

The results of optimal calculation of input energy in four scenarios are shown in Figure 8.



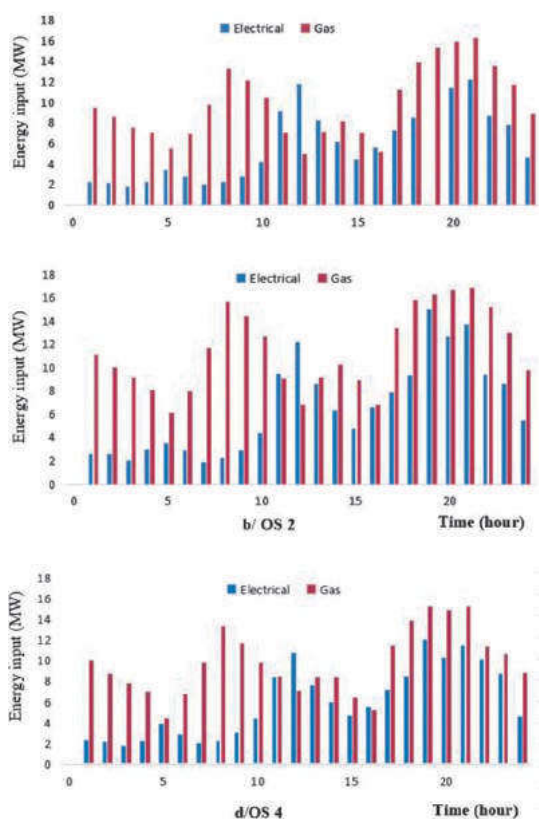


**Figure 8.** Electric and natural gas energy (input) in 4 OSs

The above results show that: The combination of several EHs forms an EN structure (including solar, wind and ESS) that responds appropriately and flexibly to the diversity of loads. The optimal results show that the optimal model can respond to changes in electricity prices and surcharges; at the same time, it allows the adjustment of renewable energy sources according to time and season.

**Table 4.** Costs comparison among 4 OSs

Calculation results	OS 1	OS 2	OS 3	OS 4
Total operation cost (\$/day)	52653	38297	34335	33782
Total operation cost (\$/day)	8.48	5.21	4.42	3.38
Total operation cost (\$/day)	857	721	615	528
Total operation cost (\$/day)	0	799	688	589

The comparison of four different EN scenarios clarified the role and impact of ESS, solar and wind on model performance by reducing the total cost categories (Table 4): operation, loss and pollution. In particular, if we compare OS 4 with OS 1, the total operating cost of OS 4 is reduced by 35.84%, the total loss is reduced by 60.14%; Therefore, cutting electricity demand during peak hours will help improve the urgent need for upgrading and renovating the power network.

The additional investment costs for the natural gas, PV, SHE and wind turbine networks are quite high but will be offset by EN's cost-effective performance. The results demonstrate that the proposed EN model contributes significantly to the study of future multi-energy systems that integrate renewable energy and energy storage systems.

**5. CONCLUSION**

Based on the energy center model, this research proposes the optimal operation between the power system and the natural gas network with the integration of solar, wind and energy storage systems.

The research analyzed the energy consumption of the whole system and emissions through four operating scenarios to assess the impact of distributed energy sources, energy storage devices on the performance of EN. Compared with the operation of the traditional grid model, the proposed model has significant advantages and provides a theoretical foundation for optimizing the operation of a system integrating various energy forms.

The results show that the EH structure in the energy network has a significant influence on operational efficiency. Therefore, further research is required on the optimal operation strategy for each EH and the optimization of the EH structure within the entire energy network.

**Acknowledgments:** *This work was supported by the Thai Nguyen University of Technology (TNUT), Thai Nguyen, Vietnam (T2020-B16).*

**REFERENCE**

1. M. Geidl, G. Koeppel, P. Favre-Perrod et al. Energy hubs for the future. *Power Energy Magaz, IEEE*, **2007**, 5(1), 24-30.
2. T. Krause, G. Andersson, K. F. Hlich et al. Multiple- energy carriers: Modeling of production, delivery, and consumption, *Proc IEEE*, **2015**, 99(1), 15-27.
3. X. Xu, H. Jia, D. Wang et al. Hierarchical energy management system for multi-source multi-product microgrids, *Renew Energy*, **2015**, 78, 621-630.
4. Y. B. Zha, T. Zhang, Z. Huang, et al. Analysis of energy internet key technologies, *Sci China*, **2014**, 44(6), 702-713.
5. Q. Sun, R. Han, H. Zhang, et al. A multiagent-based consensus algorithm for distributed coordinated control of distributed generators in the energy Internet, *IEEE Trans Smart Grid*, **2015**, 6(6), 3006-3019.
6. Y. Ma, X. Wang, X. Zhou, et al. *An overview of energy internet*, In: Proceeding of IEEE 2016 Chinese Control and Decision Conference (CCDC), Yinchuan, China, 28-30 May 2016, 6212-6215.
7. T. Ha, Y. Zhang, V. V. Thang, et al. Energy hub modeling to minimize residential energy costs considering solar energy and BESS, *Journal of Modern Power Systems Clean Energy*, **2017**, 5(3), 389-399.
8. T. T. Ha, Y. J. Zhang, J. B. Hao, et al. *Optimal operation of energy hub with different structures for minimal energy usage cost*. In: Proceedings of the 2017 IEEE International conference on power and renewable energy, Chengdu, China, 2017, 31-36.
9. G. Geidl, Martin, Andersson. *A modeling and optimization approach for multiple energy carrier power flow*, In: Power Tech IEEE, St. Petersburg, Russia, 27-30 June 2005, 1-7.
10. M. Geidl. *Integrated modeling and optimization of multi-carrier energy systems*, Zurich, Switzerland, 2007.
11. M. Arnold, R. Negenborn, G. Andersson, et al. Distributed predictive control for energy hub coordination in coupled electricity and gas networks, *Int Syst Cont Auto Sci Engin*, **2010**, 42, 235-273.
12. B. Lu, M. Shahidehpour. Short-term Scheduling of battery in a grid-connected PV/Battery system, *IEEE Trans Power Syst*, **2005**, 20(2), 1053-1061.
13. M. Rastegar, M. Fotuhi-Firuzabad, M. Lehtonen. Home load management in a residential energy hub, *Electric Power System Research*, **2015**, 119, 322-328.
14. X. W. Shen, Y. D. Han, S. Z. Zhu et al. Comprehensive power-supply planning for active distribution system considering cooling, heating and power load balance, *Journal of Modern Power Systems and Clean Energy*, **2015**, 3(4), 485-493.
15. M. X. Liu, Y. Shi, F. Fang. Combined cooling, heating and power systems, *Renewable and Sustainable Energy Reviews*, **2014**, 35, 1-22.
16. M. Mohammadi, Y. Noorollahi, B. Mohammadiivatloo et al. Energy hub: From a model to a concept – A review, *Renewable and Sustainable Energy Reviews*, **2017**, 80, 1512-1527.
17. S. Pazouki, M. R. Haghifam, A. Moser. Uncertainty modeling in optimal operation of energy hub in presence of wind, storage and demand response, *International Journal of Electrical Power and Energy System*, **2014**, 61, 335-345.
18. Gas Commodity Fact Sheet for Maryland Public Service Commission (2014), <http://www.psc.state.md.us/gas/>, accessed 20 Oct. 2016.
19. A. Brooke, D. Kendrick, A. Meeraus. *GAMS, A User's Guide*, AMS Development Corp: Washington, US, 2003.



# Quy trình tính toán độ bền dầm bê tông cốt thép chịu mômen uốn - xoắn đồng thời theo TCVN 5574:2018

Phạm Thị Lan\*, Hoàng Công Duy

*Khoa Kỹ thuật và Công nghệ, Trường Đại học Quy Nhơn, Việt Nam*

*Ngày nhận bài: 22/01/2021; Ngày nhận đăng: 05/04/2021*

## TÓM TẮT

Bài báo này phân tích lý thuyết tính toán độ bền cấu kiện bê tông cốt thép chịu uốn - xoắn đồng thời theo Tiêu chuẩn TCVN 5574:2018. Từ đó đề xuất một quy trình tính toán độ bền của dầm bê tông cốt thép chịu mômen uốn – xoắn đồng thời theo tiêu chuẩn hiện hành của Việt Nam, giúp việc thiết kế kết cấu của các kỹ sư đơn giản hơn.

**Từ khóa:** *Dầm bê tông cốt thép, quy trình tính toán độ bền cấu kiện chịu uốn – xoắn đồng thời, dầm bê tông cốt thép chịu uốn – xoắn đồng thời.*

---

\*Tác giả liên hệ chính.

Email: [ptlan@ftt.edu.vn](mailto:ptlan@ftt.edu.vn)

# Proposing a strength design process of reinforced concrete beams under combined bending and torsion based on TCVN 5574:2018 standard

Pham Thi Lan\*, Hoang Cong Duy

*Faculty of Engineering and Technology, Quy Nhon University, Vietnam*

*Received: 22/01/2021; Accepted: 05/04/2021*

## ABSTRACT

This paper analyzes the theory of calculating the strength of reinforced concrete members subject to combined bending and torsion by the TCVN 5574:2018 standard. And a strength design process of reinforced concrete beams under combined bending and torsion based on the current standard of Viet Nam will be offered, which helps construction engineers' design easier.

**Keywords:** *Reinforced concrete beams, strength design process for members under combined bending and torsion, reinforced concrete beams under bending and torsion.*

## 1. INTRODUCTION

In reinforced concrete structures, there are almost no members under pure torsion, but members under combined bending and torsion are quite common. For example, balcony support beams, side beams, etc. are members where the force acting on them is not in the plane passing through their longitudinal axis.

The torsional bearing capacity of reinforced concrete structures is much worse than their bending bearing capacity. Therefore, in many cases, although the value of the torsional moment is not great, it has a significant influence and causes the appearance of cracks. In the design of reinforced concrete members should avoid or reduce the torsional moment as much as possible.<sup>1,2</sup>

Section 8.1.4 of TCVN 5574:2018 standard presents principles of strength design of reinforced concrete members for torsional

moments. This article will base on these principles to develop a process to apply in the design of reinforced concrete members under combined bending and torsion.

## 2. STRENGTH DESIGN OF REINFORCED CONCRETE MEMBERS WITH RECTANGULAR CROSS-SECTION FOR COMBINED TORSIONAL AND BENDING MOMENTS BASED ON TCVN 5574:2018 STANDARD

### 2.1. Basic provisions

Strength design of reinforced concrete members with rectangular cross-section for torsional moments is performed based on model of spatial sections. In the design based on model of spatial sections, we should consider sections formed by inclined lines, passing on three tensile sides of a member, and closing line passing on the fourth compressive side.

\*Corresponding author:

Email: [ptlan@ft.edu.vn](mailto:ptlan@ft.edu.vn)



The design of reinforced concrete members for torsional moments is performed with regard to strength of spatial sections and a member between them. Concrete strength between spatial sections is characterized by maximum values of torsional moment which is determined by axial tensile resistance of concrete considering stress state in concrete between spatial sections.

Analysis of spatial sections is performed based on equilibrium expressions of all internal and external forces about an axis in the centre of the compression zone of the spatial section. Internal moments include moment which is sustained by rebars passing along the member axis; by rebars passing across the member axis, crossing the spatial section and placed in the compression zone of the spatial section and at the tension member side opposite to the compression zone of the spatial section. Then internal forces sustained by reinforcement are determined corresponding to design values of tensile resistance of longitudinal and transverse reinforcement.

In the design, we should consider all positions of a spatial section with compression zone at bottom, lateral and top sides of a member. Analysis for combined torsional and bending moments, as well as torsional and shear forces is performed according to equilibrium expressions between the respective force factors.

**2.2. Strength design of reinforced concrete members for combined torsional and bending moments**

Section 8.1.4.3 of TCVN 5574:2018 standard shows that the design of members under combined bending and torsion should comply with the following two conditions:

*2.2.1. Condition on the strength of a member between spatial sections*

Strength design of a member between spatial sections should comply with the condition (1):<sup>3</sup>

$$T \leq 0.1R_bhb^2 \tag{1}$$

Where :

T : Torsional moment due to external loads in the normal section of a member.

R<sub>b</sub> : Design axial compressive resistance of concrete for first group limit states.

b, h : Dimensions of a cross-section (b ≤ h).

*2.2.2. Condition on the strength of spatial sections*

Scheme of forces at the design of a spatial section for torsional moments is shown in Figure 1.<sup>3</sup>

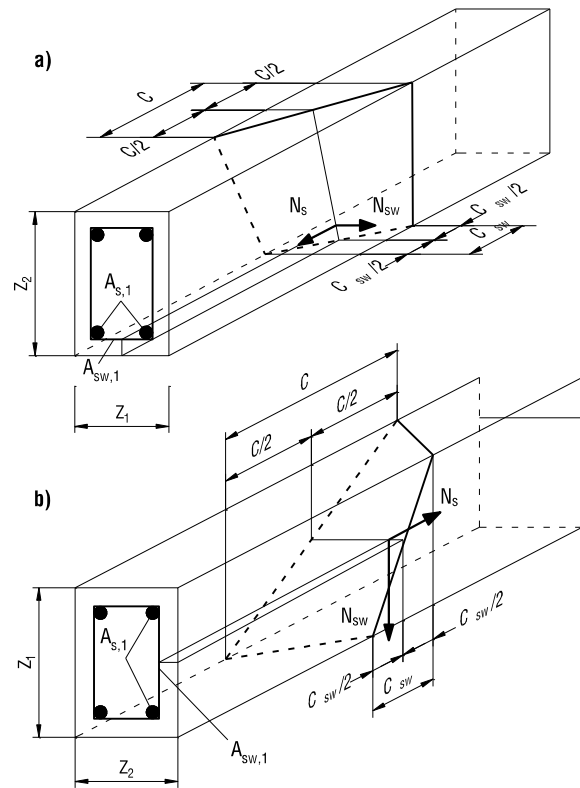


**Figure 1.** Scheme of forces at the design of a spatial section for torsional moments  
a) Tensile reinforcement at bottom side; b) Tensile reinforcement at lateral side

Strength design of a spatial section is performed according to the condition (2):<sup>3</sup>

$$T \leq T_0 \sqrt{1 - \left(\frac{M}{M_0}\right)^2} \tag{2}$$

Where :

T: Torsional moment due to external load in a spatial section;

$T_0$ : Torsional moment due to external load in a spatial section;

M: Bending moment due to external load in a normal section;

$M_0$ : Ultimate bending moment sustained by a normal section.

For design of combined torsional and bending moments, the spatial section with tensile reinforcement should be considered, when tensile reinforcement is located at the tensile side due to the bending moment, that is at the side normal to the plane of bending moment.

Torsional moment T due to external load is determined in a normal section located in the middle of the projection length C along the longitudinal axis of a member. Bending moment M due to external load is determined in a normal section as well.

Ultimate torsional moment  $T_0$  is determined by the formula:

$$T_0 = T_{sw} + T_s \quad (3)$$

Where:

$T_{sw}$ : Torsional moment sustained by reinforcement with a spatial section in cross direction with respect to the axis of a member:

$$T_{sw} = 0.9N_{sw} Z_2 \quad (4)$$

$T_s$ : Torsional moment sustained by reinforcement with a spatial section in longitudinal direction:

$$T_s = 0.9N_s \frac{Z_1}{C} Z_2 \quad (5)$$

$N_{sw}$ : Force in reinforcement located in cross direction:

$$N_{sw} = q_{sw,l} C_{sw} \quad (6)$$

$q_{sw,l}$ : Force in this reinforcement per unit length of a member:

$$q_{sw,l} = \frac{R_{sw} A_{sw,l}}{s_w} \quad (7)$$

$A_{sw,l}$ : sectional area of reinforcement in the cross direction;

$s_{sw}$ : Spacing of reinforcement in the cross direction;

$C_{sw}$ : Projection length of the tensile side of a spatial section on the longitudinal axis of a member:

$$C_{sw} = \delta C \quad (8)$$

$\delta$  - Coefficient considering ratio of cross-section dimensions:

$$\delta = \frac{Z_1}{2Z_2 + Z_1} \quad (9)$$

C - Projection length of the compressive side of a spatial section on the longitudinal axis of a member;

$N_s$ : Force in longitudinal reinforcement in the referred side:

$$N_s = R_s A_{s,l} \quad (10)$$

$A_{s,l}$ : Sectional area of longitudinal reinforcement in the referred side;

$Z_1$  and  $Z_2$ : length of the cross-sectional side at the referred tensile side and the length of another cross-sectional side (Figure 1).

**Note:**

+ The ratio  $\varphi_w$  should comply with the condition:

$$0.5 \leq \varphi_w = \frac{q_{sw,l} Z_1}{R_s A_{s,l}} \leq 1.5 \quad (11)$$

In case exceeds the stated values, the design should consider reinforcement ( $A_{s,l}$  and  $A_{sw,l}$ ) within the stated values.

+ The design is performed for spatial sections located along the length of a member at the most critical projection length of a spatial section C on the longitudinal axis. C is determined by the method of iterative approximation, calculate the derivative of the second member of condition (3) according to C and then assumed equal to 0.

$$\Rightarrow C = \sqrt{\frac{R_s A_{s,l} (2Z_2 + Z_1)}{q_{sw,l}}} \quad (12)$$

And C should comply with the condition:

$$C \leq \begin{cases} 2Z_2 + Z_1 \\ Z_1 \sqrt{2/\delta} \end{cases} \quad (13)$$

Ultimate bending moment  $M_0$  is determined by the problem of checking the load bearing capacity of the bending members. The steps to calculate  $M_0$  of rectangular cross-section with single reinforcement are done as follows:<sup>1-4</sup>

$$\text{Calculate: } \xi = \frac{R_s A_s}{R_b Z_1 (Z_2 - a)} \quad (14)$$

$$\Rightarrow \alpha_m = \xi(1 - 0.5\xi) \quad (15)$$

$$\Rightarrow M_0 = \alpha_m R_b Z_1 (Z_2 - a)^2 \quad (16)$$

**2.3. Strength design of reinforced concrete members for combined torsional and shear force**

Section 8.1.4.4 of TCVN 5574:2018 standard shows that the design of members under combined torsional moment and shear force should comply with the following two conditions:

*2.3.1. Condition on the strength of a member between spatial sections*

Strength design of a member between spatial sections should comply with the condition (17):<sup>3</sup>

$$T \leq T_0 \left( 1 - \frac{Q}{Q_0} \right) \quad (17)$$

Where :

T : Torsional moment due to external load in a normal section;

$T_0$ : Torsional moment sustained by a member between spatial sections and assumed equal to:

$$T_0 = 0.1 R_b h b^2 \quad (18)$$

Q: Shear force due to external load in the same normal section;

$Q_0$ : Ultimate shear force sustained by concrete between inclined sections and assumed equal to:

$$Q_0 = 0.3 R_b b h_0 \quad (19)$$

*2.3.2. Condition on the strength of spatial sections*

- Strength design of a spatial section is performed according to (17) with the following values:

T: Torsional moment due to external load in a spatial section;

$T_0$ : Torsional moment sustained by a spatial section;

Q: Shear force in an inclined section;

$Q_0$ : Ultimate shear force sustained by an inclined section.

- In the design for combined torsional moment and shear force, the spatial section with tensile reinforcement should be considered, when tensile reinforcement is located at one tensile side due to shear force, that is at the side parallel to the plane of shear force.

- Torsional moment T due to external load is determined in a normal section located in the middle of the projection length C along the longitudinal axis of a member. Shear force Q due to external load is determined in the normal section as well.

- Ultimate torsional moment  $T_0$  is determined according to the formula (3).

- Ultimate shear force  $Q_0$  is determined according to the formula (20):<sup>1-4</sup>

$$Q_0 = Q_b + Q_{sw} \quad (20)$$

Where  $Q_{sw}$ ,  $Q_b$  : shear force sustained by transverse reinforcement and concrete:

$$Q_{sw} = 0.75 q_{sw} C' \quad (21)$$

Where  $C'$  should comply with the condition:  $h_0 \leq C' \leq 2h_0$

$$q_{sw} = \frac{R_{sw} A_{sw}}{s} \quad (22)$$

$Q_b$  is determined as follows:

If  $q_{sw} \geq 0.25 R_{bt} b$ ,  $Q_b$  is determined by the formula:

$$Q_b = \frac{1.5 R_{bt} b h_0^2}{C'} \quad (23)$$

If  $q_{sw} < 0.25R_{bt}b$ ,  $Q_b$  is determined by the formula:

$$Q_b = \frac{6q_{sw}h_0^2}{C'} \quad (24)$$

Where  $0.5R_{bt}bh_0 \leq Q_b \leq 2.5R_{bt}bh_0$  (or  $0.6h_0 \leq C' \leq 3h_0$ ).

$C'$  is the most critical projection length of a spatial.  $C'$  is determined by the method of iterative approximation, calculate the derivative of the second member of condition (20) according to  $C'$  and then assumed equal to 0.

$$\Rightarrow C' = \sqrt{\frac{2R_{bt}bh_0^2}{q_{sw}}} \quad (25)$$

**2.4. The strength design process of reinforced concrete beams under combined bending and torsion**

**Problem in words:** known  $M, T, Q, b, h, R_b, R_{bt}, R_s, R_{sc}, R_{sw}, \xi_R$ . Requirement: calculate and arrange the reinforcement.

**Perform the following steps:**

**Use the problem: calculate the longitudinal reinforcement support bending moment  $M$ :**<sup>3</sup>

1. Assume  $a \Rightarrow h_0 = h - a$

2. Calculate  $\alpha_m$ :  $\alpha_m = \frac{M}{R_b bh_0^2}$  (26)

3. Calculate  $\xi$ :

$$\xi = 1 - \sqrt{1 - 2\alpha_m} \leq \xi_R \quad (27)$$

4. Calculate area of tensile reinforcement section:

$$A_s = \frac{\xi R_b bh_0}{R_s} \quad (28)$$

5. Select and reinforce the longitudinal reinforcement  $\Rightarrow$  the actual value of  $a, a', h_0$  ( $A'_s$  provided by structural requirements).

**Use the problem: calculate the transverse reinforcement support shear force  $Q \Rightarrow A_{sw}, s$ :**<sup>3</sup>

6. Select the transverse reinforcement according to the conditions:

-  $\phi_d \geq 6 \text{ mm}$

$$- q_{sw} = \frac{R_{sw} A_{sw}}{s} \quad (29)$$

$$- s \leq \begin{cases} s_{max} = \frac{R_{bt} bh_0^2}{Q} \\ 0.5h_0 \\ 300 \text{ mm} \end{cases} \quad (30)$$

7. Check the condition:

$$Q \leq Q_0 \quad (31)$$

Where:  $Q_0$  is determined according to (20)

If the condition (31) is not satisfied, reselect the transverse reinforcement according to step 6 until the condition (31) is satisfied, then move to step 8.

**Design for combined torsional moment (T) and bending moment (M):**

8. Check the condition (1).

If the condition (1) is not satisfied, increase the cross-sectional size ( $b, h$ ) or increase the grade of compressive strength of concrete ( $B$ ) until the condition (1) is satisfied, then go to step 9.

9. Check the condition (11), where:  $Z_1 = b; Z_2 = h$  and  $A_{s,1}, A_{sw,1}$  are tensile reinforcement at bottom side  $b$  (Figure 1a).

If the condition (11) is not satisfied, adjust  $A_{s,1}, A_{sw,1}$  into the design until the condition (11) is satisfied, then move to step 10.

10. Calculate  $C$  according to formula (12).

11. Calculate  $\delta$  according to formula (9).

12. Calculate  $C_{sw}$  according to formula (8).

13. Calculate  $N_{sw}$  according to formula (6).

14. Calculate  $T_{sw}$  according to formula (4).

15. Calculate  $N_s$  according to formula (10).

16. Calculate  $T_s$  according to formula (5).

17. Calculate  $T_0$  according to formula (3).

18. Calculate  $\xi$  according to formula (14).

19. Calculate  $\alpha_m$  according to formula (15).

20. Calculate  $M_0$  according to formula (16).

21. Check the condition (2).

If the condition (2) is not satisfied, increase the cross-sectional size (b,h) or increase longitudinal reinforcement, transverse reinforcement and then repeat steps from 9 to 21 until the condition (2) is satisfied and go to step 22.

**Design for combined torsional moment (T) and shear force (Q):**

22. Calculate  $T_0$  according to formula (18).

23. Calculate  $Q_0$  according to formula (19).

24. With  $T_0$  and  $Q_0$  just calculated in steps 22, 23, check the condition (17).

If the condition (17) is not satisfied, increase the cross-sectional size (b, h) or increase the grade of compressive strength of concrete (B) until the condition (17) is satisfied, then move to step 25.

25. Check the condition (11), where:  $Z_1 = h$ ;  $Z_2 = b$  and  $A_{s,1}$ ,  $A_{sw,1}$  are tensile reinforcement at lateral side h (Figure 1b).

If the condition (11) is not satisfied, adjust  $A_{s,1}$ ,  $A_{sw,1}$  into the design until the condition (11) is satisfied, then move to step 25.

26. Perform steps from 10 to 17.

27. Calculate  $Q_0$  according to formula (20).

28. With  $T_0$  and  $Q_0$  just calculated above, check the condition (17).

If the condition (17) is not satisfied, increase the cross-sectional size (b, h) or increase longitudinal reinforcement, transverse reinforcement and then repeat steps from 25 to 28 until the condition (17) is satisfied → **Finish**.

**2.5. Example**

A beam with rectangular cross-section:  $b = 300$ ;  $h = 600$ ,  $h$  - height of rectangular. Grade of compressive strength of concrete: B20. Bending moment:  $M = -160$  kNm, torsional moment:  $T = 40$  kNm, shear force:  $Q = 120$  kN. Longitudinal reinforcement: CB400-V, transverse

reinforcement: CB300-T. Requirement: calculate and arrange the reinforcement.

**Data:** Concrete:  $R_b = 11.5$  MPa,  $R_{bt} = 0.9$  MPa ; longitudinal reinforcement:  $R_s = R_{sc} = 350$  MPa; transverse reinforcement:  $R_{sw} = 210$  MPa;  $\xi_R = 0,583$ .<sup>3</sup>

**Perform the following steps:**

**Use the problem: calculate the longitudinal reinforcement support bending moment M:**

1. Assume  $a = 40$ ;  $h_0 = 600 - 40 = 560$  mm

$$2. \alpha_m = \frac{M}{R_b b h_0^2} = \frac{160 \times 10^6}{11.5 \times 300 \times 560^2} = 0.148$$

3.

$$\xi = 1 - \sqrt{1 - 2\alpha_m} = 1 - \sqrt{1 - 2 \times 0.148} = 0.161 \leq \xi_R = 0.583$$

4. Area of tensile reinforcement section:

$$A_s = \frac{\xi R_b b h_0}{R_s} = \frac{0.161 \times 11.5 \times 300 \times 560}{350} = 889 \text{ mm}^2$$

5. Provide for the longitudinal reinforcement as follows:

$A_s = 4\phi 18 = 1018 \text{ mm}^2$ ;  $A'_s = 2\phi 16 = 402 \text{ mm}^2$ ; structural reinforcement in the middle of edge h:  $2\phi 14 = 308 \text{ mm}^2$

Concrete cover: 25 mm

$a = 25 + 18/2 = 34$  mm ;  $h_0 = 566$  mm;  $a' = 25 + 16/2 = 33$  mm

**Use the problem: calculate the transverse reinforcement support shear force Q:**

6. Transverse reinforcement  $\phi 10$  with  $A_{sw} = 2 \times 78.5 = 157 \text{ mm}^2$

Distance between stirrups  $s = 100$  mm.

7. Check the condition (31):

$$q_{sw} = \frac{R_{sw} A_{sw}}{s} = \frac{210 \times 157}{100} = 329.7 \text{ N/mm} > 0.25 R_{bt} b = 67.5 \text{ MPa}$$

$$C' = \sqrt{\frac{2R_{bt} b h_0^2}{q_{sw}}} = \sqrt{\frac{2 \times 0.9 \times 300 \times 560^2}{329.7}} = 717 \text{ mm}$$

With:  $0.6h_0 \leq C' \leq 3h_0$ , take  $C' = 717$  mm calculate:

$$Q_b = \frac{1.5R_{bt}bh_0^2}{C'} = \frac{1.5 \times 0.9 \times 300 \times 560^2}{717} = 177138 \text{ N}$$

With:  $h_0 \leq C' \leq 2h_0$ , take  $C' = 717 \text{ mm}$  calculate:

$$Q_{sw} = 0.75q_{sw}C' = 0.75 \times 329.7 \times 717 = 177296 \text{ N}$$

$$\Rightarrow Q_0 = Q_b + Q_{sw} = 177138 + 177296 = 354434 \text{ N} = 354.434 \text{ kN}$$

We see that  $Q = 120 \text{ kN} < Q_0 = 354.434 \text{ kN}$

$\Rightarrow$  The reinforcement is arranged as shown in Figure 2a.

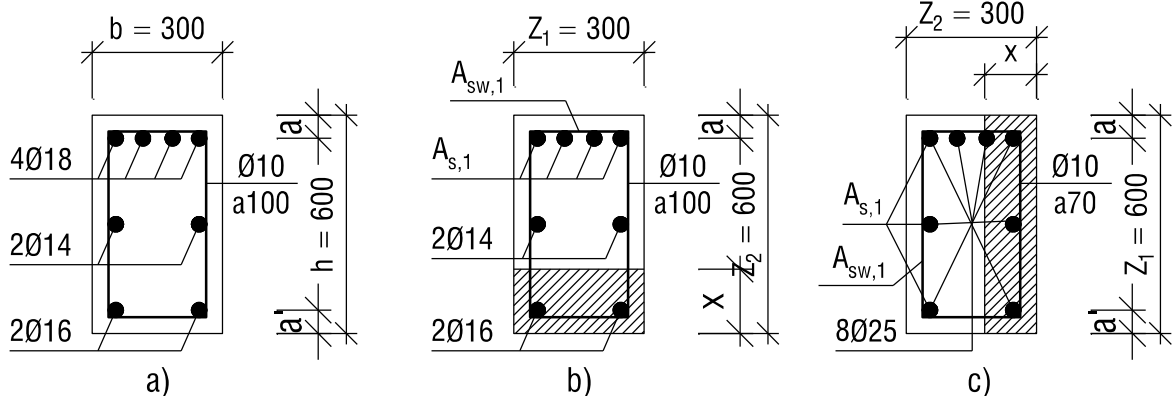


**Figure 2.** Beam cross section and calculation diagram

From Figure 2b, we have:

$$Z_1 = b = 300 \text{ mm}; Z_2 = h = 600 \text{ mm}$$

$$A_{s,1} = 4\phi 18 = 1018 \text{ mm}^2; A_{sw,1} = \phi 10 = 78.5 \text{ mm}^2$$

$$q_{sw,1} = q_{sw}/2 = 164.85 \text{ N/mm}$$

We see that:

$$\frac{q_{sw,1}Z_1}{R_s A_{s,1}} = \frac{164.85 \times 300}{350 \times 1018} = 0.139 < 0.5$$

So to adjust the above ratio, we reduce  $A_{s,1}$  into the calculation:

$$\text{Take } A_{s,1} = 1\phi 18 = 255 \text{ mm}^2$$

$$\Rightarrow 0.5 < \frac{q_{sw,1}Z_1}{R_s A_{s,1}} = \frac{164.85 \times 300}{350 \times 255} = 0.554 < 1.5$$

10.

$$C = \sqrt{\frac{R_s A_{s,1} (2Z_2 + Z_1)}{q_{sw,1}}} = \sqrt{\frac{350 \times 255 (2 \times 600 + 300)}{164.85}} = 901 \text{ mm}$$

**Design for combined torsional moment (T) and bending moment (M):**

The scheme for the design is shown in Figure 2b.

8. Check the condition (1):

$$0.1R_b hb^2 = 0.1 \times 11.5 \times 600 \times 300^2 = 62.1 \times 10^6 \text{ Nmm} = 62.1 \text{ kNm.}$$

$$\text{So: } T = 40 \text{ kNm} < 0.1R_b hb^2 = 62.1 \text{ kNm.}$$

9. Condition on the strength of spatial sections:

We see that:

$$C = 901 \text{ mm} < \begin{cases} 2Z_2 + Z_1 = 1500 \text{ mm} \\ Z_1 \sqrt{2/\delta} = 300 \sqrt{2/0.2} = 949 \text{ mm} \end{cases}$$

$$11. \delta = \frac{Z_1}{2Z_2 + Z_1} = \frac{300}{2 \times 600 + 300} = 0.2$$

$$12. C_{sw} = \delta C = 0.2C = 180.2 \text{ mm}$$

$$13. N_{sw} = q_{sw,1} C_{sw} = 164.85 \times 180.2 = 29705.97 \text{ N}$$

$$14. T_{sw} = 0.9 N_{sw} Z_2 = 0.9 \times 29705.97 \times 600 = 16.041 \times 10^6 \text{ Nmm}$$

$$15. N_s = R_s A_{s,1} = 350 \times 255 = 89250 \text{ N}$$

16.

$$T_s = 0.9 N_s \frac{Z_1}{C} Z_2 = 0.9 \times 89250 \times \frac{300}{901} \times 600 = 16.047 \times 10^6 \text{ Nmm}$$

$$17. T_0 = T_{sw} + T_s = 16.041 \times 10^6 + 16.047 \times 10^6 = 32.088 \times 10^6 \text{ Nmm} = 32.088 \text{ kNm}$$

$$18. \xi = \frac{R_s A_s}{R_b Z_1 (Z_2 - a)} = \frac{350 \times 1018}{11.5 \times 300 \times 566} = 0.182$$

19.  $\alpha_m = \xi(1-0.5\xi) = 0.182(1-0.5 \times 0.182) = 0.166$

20.  $M_0 = \alpha_m R_b Z_1 (Z_2 - a)^2 = 0.166 \times 11.5 \times 300 \times 566^2 = 183.468 \times 10^6 \text{ Nmm} = 183.468 \text{ kNm}$

21. We see that:

$$T = 40 \text{ kNm} > T_0 \sqrt{1 - \left(\frac{M}{M_0}\right)^2} = 32.088 \sqrt{1 - \left(\frac{160}{183.468}\right)^2} = 15.702 \text{ kNm}$$

⇒ **The member does not have enough load bearing capacity.**

Re-select the longitudinal reinforcement:  
 $A_s = 4\phi 25 = 1963 \text{ mm}^2$ ;  $A'_s = 2\phi 25 = 982 \text{ mm}^2$ ;  
 structural reinforcement in the middle of edge  
 h:  $2\phi 25 = 982 \text{ mm}^2$

Concrete cover: 25 mm

$a = 25 + 25/2 = 37.5 \text{ mm}$ ;  $h_0 = 562.5 \text{ mm}$ ;  $a' = 25 + 25/2 = 37.5 \text{ mm}$

Transverse reinforcement:  $\phi 10$  with  $A_{sw} = 2 \times 78.5 = 157 \text{ mm}^2$ .

Distance:  $s = 70 \text{ mm}$ .

⇒ **Repeat from step 9 to 21:**

9. Take  $A_{s,1} = 4\phi 25 = 1963 \text{ mm}^2$ ;  $A_{sw,1} = \phi 10 = 78.5 \text{ mm}^2$

$q_{sw,1} = R_{sw} A_{sw,1} / s = 210 \times 78.5 / 70 = 235.5 \text{ N/mm}$

We see:  $\frac{q_{sw,1} Z_1}{R_s A_{s,1}} = \frac{235.5 \times 300}{350 \times 1963} = 0.103 < 0.5$

To adjust the above ratio, we reduce  $A_{s,1}$  into the calculation:

Take  $A_{s,1} = 400 \text{ mm}^2$

$0.5 < \frac{q_{sw,1} Z_1}{R_s A_{s,1}} = \frac{235.5 \times 300}{350 \times 400} = 0.505 < 1.5$

10.

$$C = \sqrt{\frac{R_s A_{s,1} (2Z_2 + Z_1)}{q_{sw,1}}} = \sqrt{\frac{350 \times 400 (2 \times 600 + 300)}{235.5}} = 944 \text{ mm}$$

We see that:

$$C = 944 \text{ mm} < \begin{cases} 2Z_2 + Z_1 = 1500 \text{ mm} \\ Z_1 \sqrt{2/\delta} = 300 \sqrt{2/0.2} = 949 \text{ mm} \end{cases}$$

11.  $\delta = 0.2$

12.  $C_{sw} = 0.2C = 188.8 \text{ mm}$

13.  $N_{sw} = q_{sw,1} C_{sw} = 235.5 \times 188.8 = 44462.4 \text{ N}$

14.  $T_{sw} = 0.9 N_{sw} Z_2 = 0.9 \times 44462.4 \times 600 = 24.010 \times 10^6 \text{ Nmm}$

15.  $N_s = R_s A_{s,1} = 350 \times 400 = 140000 \text{ N}$

16.

$$T_s = 0.9 N_s \frac{Z_1}{C} Z_2 = 0.9 \times 140000 \times \frac{300}{944} \times 600 = 24.025 \times 10^6 \text{ Nmm}$$

17.  $T_0 = T_{sw} + T_s = 24.010 \times 10^6 + 24.025 \times 10^6 = 48.035 \times 10^6 \text{ Nmm} = 48.035 \text{ kNm}$

18.  $\xi = \frac{R_s A_s}{R_b Z_1 (Z_2 - a)} = \frac{350 \times 1963}{11.5 \times 300 \times 562.5} = 0.354$

19.  $\alpha_m = \xi(1-0.5\xi) = 0.354(1-0.5 \times 0.354) = 0.291$

20.  $M_0 = \alpha_m R_b Z_1 (Z_2 - a)^2 = 0.291 \times 11.5 \times 300 \times 562.5^2 = 318.029 \times 10^6 \text{ Nmm} = 318.029 \text{ kNm}$

21. We see that:

$$T = 40 \text{ kNm} < T_0 \sqrt{1 - \left(\frac{M}{M_0}\right)^2} = 48.035 \sqrt{1 - \left(\frac{160}{318.029}\right)^2} = 41.513 \text{ kNm}$$

*Conclusion:* So that the member has enough capacity to bear combined torsional moment and bending moment, we need the amount of reinforcement.: tensile longitudinal reinforcement  $A_s = 4\phi 25$ , CB400-V and stirrup  $\phi 10$ , CB300-T,  $s = 70 \text{ mm}$ .

**Design for combined torsional moment (T) and shear force (Q):**

The scheme for the design is shown in Figure 2c.

22.  $T_0 = 0.1 R_b h b^2 = 62.1 \text{ kNm}$ .

$$23. Q_0 = 0.3R_b b h_0 = 0.3 \times 11.5 \times 300 \times 562.5 = 582187.5 \text{ N} = 582.188 \text{ kN}$$

24. Check the condition (17):

$$T = 40 \text{ kN} \leq T_0 \left(1 - \frac{Q}{Q_0}\right) = 62.1 \left(1 - \frac{120}{582.188}\right) = 49.3 \text{ kN} \Rightarrow \text{Satisfied}$$

25. Condition on the strength of spatial sections:

From Figure 2c, we have:

$$Z_1 = h = 600 \text{ mm}; Z_2 = b = 300 \text{ mm}$$

$$A_{s,1} = 3\phi 25 = 1473 \text{ mm}^2; A_{sw,1} = \phi 10 = 78.5 \text{ mm}^2$$

$$q_{sw,1} = 235.5 \text{ N/mm}$$

$$\text{We see: } \frac{q_{sw,1} Z_1}{R_s A_{s,1}} = \frac{235.5 \times 600}{350 \times 1473} = 0.274 < 0.5$$

To adjust the above ratio, we reduce  $A_{s,1}$  into the calculation:

$$\text{Take } A_{s,1} = 800 \text{ mm}^2$$

$$\Rightarrow 0.5 < \frac{q_{sw,1} Z_1}{R_s A_{s,1}} = \frac{235.5 \times 600}{350 \times 800} = 0.505 < 1.5$$

26. Perform steps from 10 to 17.

$$C = \sqrt{\frac{R_s A_{s,1} (2Z_2 + Z_1)}{q_{sw,1}}} = \sqrt{\frac{350 \times 800 (2 \times 300 + 600)}{235.5}} = 1194 \text{ mm}$$

We see:

$$C = 1194 \text{ mm} < \begin{cases} 2Z_2 + Z_1 = 1200 \text{ mm} \\ Z_1 \sqrt{2/\delta} = 600 \sqrt{2/0.5} = 1200 \text{ mm} \end{cases}$$

$$\delta = \frac{Z_1}{2Z_2 + Z_1} = \frac{600}{2 \times 300 + 600} = 0.5$$

$$C_{sw} = \delta C = 0.5C = 597 \text{ mm}$$

$$N_{sw} = q_{sw,1} C_{sw} = 235.5 \times 597 = 140593.5 \text{ N}$$

$$\Rightarrow T_{sw} = 0.9 N_{sw} Z_2 = 0.9 \times 140593.5 \times 300 = 37.960 \times 10^6 \text{ Nmm}$$

$$N_s = R_s A_{s,1} = 350 \times 800 = 280000 \text{ N}$$

$$T_s = 0.9 N_s \frac{Z_1}{C} Z_2 = 0.9 \times 280000 \times \frac{600}{1194} \times 300 = 37.990 \times 10^6 \text{ Nmm}$$

$$\Rightarrow T_0 = T_{sw} + T_s = 37.960 \times 10^6 + 37.990 \times 10^6 = 75.95 \times 10^6 \text{ Nmm} = 75.95 \text{ kNm}$$

27. Calculate  $Q_0 = (20)$ :

$$C' = \sqrt{\frac{2R_{bt} b h_0^2}{q_{sw}}} = \sqrt{\frac{2 \times 0.9 \times 300 \times 562.5^2}{2 \times 235.5}} = 602 \text{ mm}$$

$$\text{We see that } 0.6h_0 = 337.5 \text{ mm} < C' = 602 \text{ mm} < 3h_0 = 1687.5 \text{ mm}$$

$$\Rightarrow Q_b = \frac{1.5R_{bt} b h_0^2}{C'} = \frac{1.5 \times 0.9 \times 300 \times 562.5^2}{602} = 212.865 \times 10^3 \text{ N} = 212.865 \text{ kN}$$

$$\text{We see that } h_0 = 562.5 \text{ mm} < C' = 602 \text{ mm} < 2h_0 = 1125 \text{ mm}$$

$$\Rightarrow Q_{sw} = 0.75 q_{sw} C' = 0.75 \times 2 \times 235.5 \times 602 = 212.657 \times 10^3 \text{ N} = 212.657 \text{ kN}$$

$$\Rightarrow Q_0 = Q_b + Q_{sw} = 212.865 + 212.657 = 425.552 \text{ kN}$$

28. We see that:

$$T = 40 \text{ kNm} < T_0 \left(1 - \frac{Q}{Q_0}\right) = 75.95 \left(1 - \frac{120}{425.552}\right) = 54.533 \text{ kNm}$$

**Conclusion:** The member has enough capacity to bear combined torsional moment and shear force → End.

### 3. CONCLUSION

From the content presented above, we see that:

Design standard for concrete and reinforced concrete structures TCVN 5574:2018 presents principles of strength design of reinforced concrete members for combined torsional and bending moments, but the formulas are quite complicated and there is no specific design procedure for this type of member. Therefore, building a process to concretize the calculation steps is applicable and can be applied more easily in the design of structures.



Although still using the model of spatial sections according to the ultimate internal force method, but the principles of strength design of reinforced concrete members for combined torsional and bending moments provided in the TCVN 5574:2018 Standard have many changes compared to those provided in the old Standard TCVN 5574:2012.<sup>4</sup> Besides, the strength design process of reinforced concrete beams under combined bending and torsion based on TCVN 5574:2018 standard proposed in Section 2.4 is still quite complicated, especially the adjustment of the amount of longitudinal and transverse reinforcement ( $A_{s,1}$  and  $A_{sw,1}$ ) into the design leads to results that may still be subjective by the designer.

From the calculation example in Section 2.5, it can be seen that the torsional bearing capacity of reinforced concrete structures is much worse than their bending bearing capacity. Therefore, in many cases, although the value of the torsional moment is not great, it has a significant influence and causes the appearance of cracks. In the design of reinforced concrete members should avoid or reduce the torsional moment as much as possible. In some cases, when the value of the torsional moment cannot be limited, we need to design the strength of

reinforced concrete members for combined torsional and bending moments.

The assessment of the strength design process of reinforced concrete beams under combined bending and torsion is based on TCVN 5574:2018 standard compared to TCVN 5574:2012 standard and some advanced standards in the world as well as quantifying the influence of torsional moment on the bearing capacity of the member will be presented in the next issue.

## REFERENCES

1. Dinh Cong Nguyen. *Practice calculating reinforced concrete members*, Construction Publishing House, Hanoi, 2007.
2. Quang Minh Phan, The Phong Ngo, Dinh Cong Nguyen. *Reinforced concrete structures - basic members*, Science and technics Publishing House, Hanoi, 2008.
3. Vietnam Institute for Building Science and Technology, *TCVN 5574:2018 national standard: Design of concrete and reinforced concrete structures*, Hanoi, 2018.
4. Vietnam Institute for Building Science and Technology. *TCVN 5574:2012 national standard: Design of concrete and reinforced concrete structures*, Hanoi, 2012.



# Ảnh hưởng của một số phân hữu cơ vi sinh đến sinh trưởng và năng suất của măng tây xanh (*Asparagus officinalis* L.) trồng tại thành phố Quy Nhơn, tỉnh Bình Định

Nguyễn Thị Y Thanh\*, Bùi Hồng Hải, Đoàn Công Thiên, Hồ Tân

*Khoa Khoa học Tự Nhiên, Trường Đại học Quy Nhơn, Việt Nam*

*Ngày nhận bài: 22/02/2021; Ngày nhận đăng: 26/04/2021*

## TÓM TẮT

Cây măng tây (*Asparagus officinalis* L.), có giá trị dinh dưỡng cao và chứa nhiều chất có hoạt tính sinh học, được canh tác cách đây hơn 2000 năm và hiện trồng ở hơn 60 quốc gia. Du nhập vào nước ta từ những năm 1960 và trồng ở nhiều nơi nhưng chủ yếu ở tỉnh Ninh Thuận. Trong xu hướng sản xuất măng tây an toàn và bền vững, việc sử dụng loại phân hữu cơ vi sinh (HCVS) phù hợp giúp cải tạo đất, tăng chuyển hóa các chất giúp cây trồng hấp thụ dinh dưỡng tốt hơn là giải pháp hữu hiệu. Do đó, nghiên cứu được thực hiện nhằm đánh giá ảnh hưởng của một số loại phân HCVS trên thị trường đến sinh trưởng, năng suất chồi và chất lượng măng tây. Thí nghiệm được thiết kế theo khối hoàn toàn ngẫu nhiên của 5 công thức: 4 loại phân HCVS (Tribat T-MB, Đầu trâu HCMK7 Bokashi-Trichoderma+TE, Quế Lâm 01, Sông Gianh) và đối chứng - không bón phân HCVS. Mỗi công thức 3 lần lặp lại. Các chỉ tiêu sinh trưởng được đo bằng thước dây và thước Panme, hàm lượng diệp lục được xác định bằng máy so màu quang phổ, hàm lượng vitamin C xác định bằng sắc ký lỏng hiệu năng cao. Kết quả nghiên cứu cho thấy bón bổ sung phân HCVS đặc biệt phân HCVS Sông Gianh bước đầu giúp tăng chiều cao thân cây, hàm lượng diệp lục, đường kính thân, số thân (7,62 thân/cây), số chồi thu hoạch (7,9 chồi/cây), đường kính chồi (8,8 mm), trọng lượng chồi (12,55 g/chồi), hàm lượng vitamin C (341 mg/100g), năng suất thu hoạch trong 1 tháng đạt 1,6 tấn/ha. Vì vậy, bón bổ sung phân HCVS Sông Gianh bước đầu phù hợp với trồng măng tây xanh Hà Lan F1 Radius trong điều kiện canh tác ở thành phố Quy Nhơn, tỉnh Bình Định.

**Từ khóa:** *Cây măng tây (Asparagus officinalis), năng suất, phân hữu cơ vi sinh, sinh trưởng.*

\*Tác giả liên hệ chính.

Email: [nguyenthithanh@qnu.edu.vn](mailto:nguyenthithanh@qnu.edu.vn)

# Effect of some micro-organic fertilizers on growth and spear yield of *Asparagus officinalis* L. planted in Quy Nhon city, Binh Dinh province

Nguyen Thi Y Thanh\*, Bui Hong Hai, Doan Cong Thien, Ho Tan

*Faculty of Natural Sciences, Quy Nhon University, Vietnam*

*Received: 22/02/2021; Accepted: 26/04/2021*

## ABSTRACT

*Asparagus officinalis* L. which is high in nutrient content and bioactive compounds was cultured more than 2000 years ago and planted in more than 60 countries. This plant was imported into Vietnam in the 1960s and grown in many provinces, mainly in Ninh Thuan province. Toward the safe and sustainable production of asparagus, the use of micro-organic fertilizer (MOF) is an effective solution. The experiment was designed to evaluate the effect of some MOFs on growth, spear yield and some quality indicators of asparagus spear. The experiment was laid out as a randomized complete block design with three replications of 5 treatments (4 different MOFs: Tribat T-MB, Bokashi-Trichoderma + TE, Que Lam 01, Song Gianh and control). The results showed that adding MOFs, especially Song Gianh MOF initially, increased stem height, chlorophyll content, stem diameter, number of stems (7.62 stems.crown<sup>-1</sup>), number of harvested spears (7.9 spears.crown<sup>-1</sup>), spear diameter (8.8mm), spear weight (12.55 g. spear<sup>-1</sup>), vitamin C content (341 mg.100g<sup>-1</sup>), and spear yield in 1 harvest month was 1.6 tons/hectares. Therefore, the Song Gianh micro-organic fertilizer is concluded as initially suitable to asparagus cultivation in the local conditions.

**Keywords:** *Asparagus officinalis*, micro-organic fertilizer, spear yield, growth.

## 1. INTRODUCTION

*Asparagus (Asparagus officinalis* L.) which belongs to Lily family (Liliaceae) is originated from the eastern Mediterranean and Asia Minor. This perennial herb has been cultivated for more than 2000 years ago. Recently, more than 60 countries around the world have grown asparagus including the United States, Italy, Netherlands, Canada, Germany and other western developed countries. The cultivation, processing and scientific research of asparagus have extended to developing countries. China and Peru have become the world's largest exporters of asparagus, taking over two-thirds

world export market.<sup>1</sup> *Asparagus* is rich in protein, fat, vitamins and mineral, and its contents are five times higher than these of other normal vegetables.<sup>2</sup> *Asparagus* has also been used as medicine since ancient times. 94 different bioactive compounds of asparagus spears have been identified,<sup>3</sup> including steroidal saponins (asparagosides), polyphenols, anthocianins, fructans (asparagose and asparagosine), ferulic acid, minerals, vitamins and flavonoids, etc. with many pharmacological effects such as antitumor, antibacterial, antioxidant, hypolipidemic, diabetes, decompression, immunomodulatory, antiepileptic and other effects.<sup>4-6</sup> *Asparagus*

---

\*Corresponding author.

Email: [nguyenthiythanh@qnu.edu.vn](mailto:nguyenthiythanh@qnu.edu.vn)

was imported to Vietnam in the 1960s and the cultivation regions are increasingly expanding.<sup>7</sup> Ninh Thuan province is considered as a main region for asparagus cultivation with approximately 411 hectares. Meanwhile, Binh Dinh province has suitable natural conditions for asparagus growth, but its cultivation has currently only been researched and piloted. The field production is not yet conducted.

The use of chemical fertilizers for farming is currently increasing in Asia. Asian countries have used over 250 kg of NPK per hectare in 2020, as twice the world average level.<sup>8-9</sup> Long-term use of chemical fertilizers has contributed to negative consequences, including reducing the soil organic matter content, declining agricultural soil quality, increasing in soil acidification and environmental pollution.<sup>10,11</sup> Recent trends of agriculture in the world as well as in Vietnam are towards safe and sustainable agriculture. Chemical fertilizers could be replaced by micro-organic fertilizers (MOFs) to yield positive impacts. MOFs are rich in organic matter and nutrient elements that improve many soil aspects, such as soil physical properties, porosity, soil microbial community structure and biochemical properties. In addition, MOFs also contain microbes that prevent diseases and increase plant resistance, enhance agricultural product quality, provide 30-60 kg of N per year, improve fertility, and increase the amount of humus in the soil.<sup>8,9</sup> The microorganisms in MOFs have the ability to mobilize, facilitate unavailable soil nutrient availability to become available form for better absorption and increase the effectiveness of inorganic fertilizers.<sup>12-14</sup> Moreover, MOF trade marks on market are very diverse and finding suitable MOF for crop and cultivation soil is important. The objective of this study is to evaluate the effects of some MOFs on the growth and spear yield of asparagus, for contributing to eliminate the chemical fertilizers use, to improve the soil properties and the sustainability of asparagus cultivation in local area.

## 2. MATERIALS AND METHODS

### 2.1. Materials

Radius F1 green asparagus variety is originated from Netherlands. Three months asparagus crowns that were provided by Linh Dan Ninh Thuan Co., Ltd., have appropriately grown in local conditions with high spear yield, high quality and economic efficiency.

Fertilizers used include: NPK 16:16:8+TE fertilizer (Garsoni Vietnam Co. Ltd.), Tribat T-MB MOF (Green Saigon Biotechnology Co., Ltd.), Bokashi-Trichoderma + TE MOF (Binh Dien Fertilizer JSC.), Que Lam 01 MOF (Que Lam Group JSC.), Song Gianh MOF (Song Gianh Corporation). These are popular micro-organic fertilizers on Vietnam market with high quality and trusted by farmers.

### 2.2. Methods

#### 2.2.1. Experimental design

The experiment was carried out from February to June 2020 at the Experimental and research garden for Biology and Agriculture at Quy Nhon University (13.758511N, 109.216792E). The experiment used sandy soil with 86% sand and 0.5% humus. The weather condition includes average temperature of 28.9 - 30.1 °C, average humidity of 72-78%, total rainfall of 88 mm per month, and total sunshine hours of 224 hours per month.

The experiment was laid out as a randomized complete block design with 5 treatments (Treat.) and three replications. The basal fertilizer consists of 20 tons of manure + 1.200 kg NPK 16:16:8+TE fertilizer per hectare (400 kg for soil preparation and 800 kg for experiment period, according to the cultivation process proposed by the Linh Dan Ninh Thuan Co., Ltd.).<sup>15</sup> The MOFs tested include 4 supplemental MOFs and NPK fertilizer used as the control. The amount applied that is average dose of manufacturer's instructions, were calculated for 5 experiment months (Table 1).

**Table 1.** Definition of treatments

No.	Treat.	MOF kind, descriptions and dose of experimented fertilizer
1	Treat.1 (Control)	3.6 kg of NPK fertilizer 16:16:8+TE, including N (16%), P <sub>2</sub> O <sub>5</sub> (16%), K <sub>2</sub> O (8%), MgO (2%), B (100 ppm), Zn (100ppm), Fe (100 ppm), Mn (100 ppm).
2	Treat.2	NPK fertilizer (Control) + 30kg of Tribat T-MB MOF, including organic matter (15%), N (1%), P <sub>2</sub> O <sub>5</sub> (1%), K <sub>2</sub> O (1%), <i>Trichoderma sp.</i> (1x10 <sup>6</sup> CFU/g), pH <sub>H<sub>2</sub>O</sub> (≥5), humidity (30%).
3	Treat.3	NPK fertilizer (Control) + 15kg of HCMK7 Bokashi-Trichoderma+TE MOF, including organic matter (18%), N (2%), P <sub>2</sub> O <sub>5</sub> (2%), pH <sub>H<sub>2</sub>O</sub> (5), B (300 ppm), Cu (300 ppm), Zn (500 ppm), <i>Trichoderma sp.</i> (1x10 <sup>6</sup> CFU/g), humidity (30%).
4	Treat.4	NPK fertilizer (Control) + 48kg of Que Lam 01 MOF, including organic matter (15%), nitrogen fixing microorganisms (1x10 <sup>6</sup> CFU/g), Phosphate solubilizing microbes (1x10 <sup>6</sup> CFU/g), cellulose degrading microbes (1x10 <sup>6</sup> CFU/g); Ca, Mg, S, B, Cu, Fe, Mn, Zn, humic acid, and growth regulator, humidity (≤ 30%).
5	Treat.5	NPK fertilizer (Control) + 45 kg of Song Gianh MOF, including organic matter (15%), P <sub>2</sub> O <sub>5</sub> (1.5%), humic acid (2.5%), Ca (1%), Mg (0.5%), S (0.3%), <i>Bacillus</i> (1x10 <sup>6</sup> CFU/g), <i>Azotobacter</i> (1x10 <sup>6</sup> CFU/g), <i>Aspergillus sp.</i> (1x10 <sup>6</sup> CFU/g), pH <sub>H<sub>2</sub>O</sub> (5), humidity (30%).

The experiment area of 200 m<sup>2</sup> included protection path around with 3 blocks of 50 m<sup>2</sup> (5.5 m in width and 9.0 m in length). Each block consisted of five plots/beds (5 m in length and 1.2 m in width) where we transplanted one row of 10 asparagus crowns with 50 cm between crowns, equivalent of 17.000 crowns per hectare.

*2.2.2. Cultivation process*

*Soil preparation:* the soil is plowed 30 cm in deep, chopped, removed weeds and stones, diged a trench of 40 cm in wide and 30 cm in deep, interspace of 1.2 m. We put basal fertilizer to trench, added 1,200 kg of lime powder per hectare and trichoderma inoculant. After fertilizing, the soil was digged 2-3 times and dried for 30 days before transplanting.<sup>7,15</sup>

*Transplanting, fertilizing and caring* (according to instructions of Linh Dan Ninh Thuan Co., Ltd.):<sup>15</sup> The bed was digged the holes of 40x40cm with 50 cm apart. The corressponding fertilizer of each treatment was laid into holes and mixed with soil. Then, asparagus crowns were vertically transplanted so that the stem

base is 10cm above the natural ground. The root was covered by soil layer of 5-10 cm in thick to protect the root neck and hold the stems upright. After transplanting, we plugged two stakes and used nylon line tentioned to prevent falling trees. During growing, it is necessary to gradually raise the line for keeping the stems always upright. Plants were daily watered by the drip irrigation system in the morning to maintain the humidity of 60-70%. For each 15 days, plants were periodically fertilized and pruned the branches below 50 cm and the weak and old stems. 4-6 healthy stems per asparagus crown were kept for spear production. We cut the stem apex over 1.5 m in high for promoting spear emergence. It is necessary to regularly visit field for catching asparagus pests and treating diseases, such as soil worms, asparagus beetle, beet armyworm, green worms, and anthracnose.<sup>7,16</sup>

*Harvesting:* The asparagus spears were daily harvested since the 5<sup>th</sup> month after transplanting. After 15 days harvesting, the fertilizer with equal dose in the first month was applied. After a harvest month, it is necessary

to stop harvesting spears for replacing the old, weak and diseased asparagus stems.

### 2.2.3. Indicators and measurement

*Growth and development characteristics:* we marked 5 crowns in each plots (equivalent of 15 crowns for a treatment). The stem growth of marked crowns were measured every 4 days, including stem height (cm): distance from the ground level to stem apex, using a tape measure; Stem diameter (mm) measured at 2 cm above ground level with a micrometer; Number of pruned stems (pruned stems.crown<sup>-1</sup>); Stem number per crown (stems.crown<sup>-1</sup>); The leaf chlorophyll content determined by using spectrophotometry.

*Spear yield parameters:* Spear diameter (cm) measured at spear butt (about 2 cm above ground level) with a micrometer; Number of harvested spears per crown (harvested spears.crown<sup>-1</sup>): number of harvested spears with 25-30 cm in length until the end of 5<sup>th</sup> month after transplanting (June 30, 2020); Ratio of market spears (%) = (Number of each spear grade divides to total number of harvested spears) x 100. There are 3 spear grades, including grade I spears (9-12 mm in diameter or more and 19-23 cm in length), grade II spears (6-9 mm in diameter and 19-23 cm in length), grade III spears (3-6mm in diameter and 17-23 cm in length); average spear weight (g.spear<sup>-1</sup>): average weight of harvested spear; Net spear yield (tons.ha<sup>-1</sup>): total weight of harvested spears of treatment was converted to unit of ton.ha<sup>-1</sup>; Economic profit = Total revenue – total cost.

*Quality properties:* Dry matter content (%): asparagus spears were dried at 103 °C to constant weight for 72 hours; Fiber content (%): according to FAO test method 14/7 p.230-231 (1986);

Protein content (mg.100g<sup>-1</sup>) was determined according to the FAO test method 14/7 p.221-223 (1986); Vitamin C content (mg.100g<sup>-1</sup> fresh spear) was determined by using high performance liquid chromatography (TCVN 8977:2011).

### 2.2.4. Statistical analysis

The data of results were analyzed by using MS. Excel 2007 and Statistix (ver. 8.0). The experimental results were statistically analyzed by one-way ANOVA analysis with LSD (least significant difference) test for multiple comparisons at a 5% significance level.

## 3. RESULTS AND DISCUSSIONS

### 3.1. Asparagus stem growth

Three months asparagus plants which grown in the nursery were dug and cut off whole stems. After transplanting in the experimental field, asparagus crowns sprouted first spear and second spear at 7-10 days and 30-35 days after transplanting, respectively. The spears became stems during growth times. The heights of first stems and second stems at different growth times are shown in Table 2.

The data in Table 2 show that asparagus stem height increased sharply at 8-12 days after sprouting (DAS) and slowed down after that. The second stems are higher than first stems measured at same DAS. The growths of first stems and second stems of treatments were not statistical different. The height is 110.27 - 124.6 cm for first stems and 134.57- 147.13 cm for second stems. Except for Treat.5, first stems had superior height of 124.6 cm after 16 DAS. So, the asparagus crowns used the nutrients from rhizomes and soil fertilizer. The microorganisms in MOFs did not affect on plant growth in the early period after transplanting.

**Table 2.** Height of first stems and second asparagus stems at different growth times (cm)

Treat.	First stems				Second stems			
	4 DAS	8 DAS	12 DAS	16 DAS	4 DAS	8 DAS	12 DAS	16 DAS
<b>Treat.1</b>	4.57 <sup>b</sup>	61.9 <sup>c</sup>	102.57 <sup>b</sup>	110.27 <sup>b</sup>	42.0 <sup>a</sup>	101.3 <sup>a</sup>	125.67 <sup>b</sup>	134.57 <sup>b</sup>
<b>Treat.2</b>	5.14 <sup>b</sup>	68.87 <sup>bc</sup>	102.9 <sup>b</sup>	111.17 <sup>b</sup>	41.47 <sup>a</sup>	101.9 <sup>a</sup>	128.1 <sup>ab</sup>	139.2 <sup>ab</sup>
<b>Treat.3</b>	5.21 <sup>b</sup>	73.6 <sup>b</sup>	104.33 <sup>b</sup>	112.43 <sup>b</sup>	40.77 <sup>a</sup>	102.23 <sup>a</sup>	129.8 <sup>ab</sup>	142.13 <sup>ab</sup>
<b>Treat.4</b>	7.52 <sup>ab</sup>	75.59 <sup>b</sup>	105.1 <sup>b</sup>	111.07 <sup>b</sup>	47.37 <sup>a</sup>	109.23 <sup>a</sup>	135.4 <sup>a</sup>	147.13 <sup>a</sup>
<b>Treat.5</b>	8.97 <sup>a</sup>	90.4 <sup>a</sup>	115.87 <sup>a</sup>	124.6 <sup>a</sup>	41.37 <sup>a</sup>	103.93 <sup>a</sup>	133.5 <sup>ab</sup>	142.67 <sup>ab</sup>
<b>CV(%)</b>	<b>9.05</b>	<b>18.46</b>	<b>12.19</b>	<b>11.6</b>	<b>8.82</b>	<b>11.19</b>	<b>10.16</b>	<b>11.08</b>
<b>LSD<sub>0.05</sub></b>	<b>3.15</b>	<b>9.96</b>	<b>9.43</b>	<b>9.62</b>	<b>8.94</b>	<b>8.45</b>	<b>9.65</b>	<b>11.38</b>

Note: Mean followed by the same letter is not significantly different within the columns according to LSD test at a 5% significance level; CV (coefficient variance); DAS is the day after sprouting.

### 3.2. Asparagus stem diameter

The stem diameter is an important growth indicator. At 40 days after transplanting, asparagus crowns had 3 stems. The results of the stem diameters are shown in Table 3.

**Table 3.** Effect of MOFs on asparagus stem diameter (mm)

Treat.	First stems	Second stems	Third stems
<b>Treat.1</b>	5.03 <sup>a</sup>	6.63 <sup>b</sup>	7.37 <sup>b</sup>
<b>Treat.2</b>	5.13 <sup>a</sup>	6.77 <sup>ab</sup>	8.77 <sup>a</sup>
<b>Treat.3</b>	5.13 <sup>a</sup>	7.2 <sup>ab</sup>	8.77 <sup>a</sup>
<b>Treat.4</b>	5.17 <sup>a</sup>	7.1 <sup>ab</sup>	8.57 <sup>a</sup>
<b>Treat.5</b>	5.33 <sup>a</sup>	7.37 <sup>a</sup>	8.97 <sup>a</sup>
<b>CV(%)</b>	<b>16.03</b>	<b>13.94</b>	<b>15.86</b>
<b>LSD<sub>0.05</sub></b>	<b>0.60</b>	<b>0.71</b>	<b>0.98</b>

Note: Mean followed by the same letter is not significantly different within the columns according to LSD test at a 5% significance level; CV (coefficient variance).

The data in Table 3 show that the stem diameter increased gradually through stem sets. In the first stems, there was no significant difference in stem diameter between the treatments. In the second stems and third stems, the asparagus stem diameter was different between the treatments. The treatments supplemented with MOFs had

larger stem diameter compared with control and the Treat.5 had superior stem diameter (7.37 mm for the second stems and 8.97 mm for third stems). Thus, the additional MOFs affected on the asparagus growth as increasing the stem diameter, and the Song Gianh MOF is initially more suitable for green asparagus than other MOFs. Because of MOF compositions, especially Song Gianh MOF provided a large amount of organic matter and mineral elements N, Mg, S, P, the additional microorganisms which promoted the ability converting and using carbon sources, soil nutrition,<sup>14</sup> fixed nitrogen for better absorption.<sup>17</sup> Furthermore, the humic acid enhanced the micro and macronutrients absorption,<sup>18</sup> thereby promoting plant growth.<sup>19,20</sup>

### 3.3. Leaf chlorophyll content and number of asparagus stems

Leaf chlorophyll content at 50 days after transplanting was shown in Table 4. The analysis results showed that the leaf chlorophyll content of treatments were statistically significant difference. The chlorophyll content of treatments supplemented with MOFs was higher than those of control. In which, Treat.5 had the highest chlorophyll a and chlorophyll b content (0.89 and 2.43 mg.g<sup>-1</sup> fresh leaf weight, respectively) and the lowest in control (1.52 mg.g<sup>-1</sup> fresh leaf weight). The MOF addition, especially additional



Song Gianh MOF provided supplemental Mg, S, K and microorganisms that improve nutrients and mineral absorption.<sup>14,20</sup> The mineral elements

(Potassium and Sulfur) activated the enzymes that catalyze chlorophyll synthesis and Nitrogen is also an essential component of chlorophyll.<sup>21</sup>

**Table 4.** Effect of MOFs on leaf chlorophyll content, stem number and number of pruned stems

Treat.	Number of pruned stems (pruned stems.crown <sup>-1</sup> )	Stem number (stems.crown <sup>-1</sup> )	Chlorophyll a (mg.g <sup>-1</sup> )	Chlorophyll b (mg.g <sup>-1</sup> )	Chlorophyll a+ b (mg.g <sup>-1</sup> )
Treat.1	4.36 <sup>a</sup>	6.27 <sup>ab</sup>	1.04 <sup>c</sup>	0.48 <sup>c</sup>	1.52 <sup>d</sup>
Treat.2	4.00 <sup>a</sup>	5.67 <sup>b</sup>	1.07 <sup>d</sup>	0.50 <sup>d</sup>	1.57 <sup>c</sup>
Treat.3	4.67 <sup>a</sup>	6.67 <sup>ab</sup>	1.42 <sup>c</sup>	0.76 <sup>c</sup>	2.18 <sup>b</sup>
Treat.4	4.31 <sup>a</sup>	7.23 <sup>ab</sup>	1.62 <sup>a</sup>	0.80 <sup>b</sup>	2.42 <sup>a</sup>
Treat.5	4.15 <sup>a</sup>	7.61 <sup>a</sup>	1.54 <sup>b</sup>	0.89 <sup>a</sup>	2.43 <sup>a</sup>
<b>CV(%)</b>	<b>13.63</b>	<b>11.62</b>	<b>0.52</b>	<b>1.53</b>	<b>0.76</b>
<b>LSD<sub>0,05</sub></b>	<b>2.00</b>	<b>2.03</b>	<b>0.01</b>	<b>0.02</b>	<b>0.3</b>

Note: Mean followed by the same letter is not significantly different within the columns according to LSD test at a 5% significance level; CV (coefficient variance).

During asparagus growth, the weak, old and diseased stems are pruned and the healthy stems were kept for spear production. The number of stems pruned and the number of stems kept for four months after transplanting are presented in Table 4. The data in Table 4 show that the number of pruned stems in the treatments were stable (4-4.46 pruned stems.crown<sup>-1</sup>) and the means are not statistical significant difference. However, the number of healthy stems kept was

different between the treatments, and Treat.5 had the highest number of stems (7.61 stems.crown<sup>-1</sup>) and Treat.2 had the lowest number of stems (5.67 stems.crown<sup>-1</sup>).

**3.4. Asparagus spear yield and yield parameters**

Since 5<sup>th</sup> month after transplanting, asparagus crowns produced harvest spears. The number, diameter and weight of harvested spears are statistically analyzed and presented in Table 5.

**Table 5.** Effect of MOFs on asparagus spear yield components in one harvest month

Treat.	Number of harvested spears (harvested spears.crown <sup>-1</sup> )	Spear diameter (mm)	Spear weight (g.spear <sup>-1</sup> )	Spear yield (tons.ha <sup>-1</sup> )	Total market spears (spears)	Rate of market spear grades (%)		
						Grade I	Grade II	Grade III
Treat.1	5.3 <sup>c</sup>	6.89 <sup>b</sup>	9.31 <sup>b</sup>	0.78	75	15.39	53.84	30.77
Treat.2	5.63 <sup>b</sup>	7.29 <sup>a</sup>	11.04 <sup>ab</sup>	1.04	85	30.77	38.46	30.77
Treat.3	6.1 <sup>b</sup>	7.39 <sup>a</sup>	11.77 <sup>ab</sup>	1.18	90	15.39	69.22	15.39
Treat.4	6.8 <sup>a</sup>	8.58 <sup>a</sup>	12.5 <sup>ab</sup>	1.39	100	31.58	57.89	10.53
Treat.5	7.9 <sup>a</sup>	8.8 <sup>a</sup>	12.55 <sup>a</sup>	1.6	115	44.44	38.89	16.37
<b>CV(%)</b>	<b>17.48</b>	<b>10.94</b>	<b>15.30</b>	-	-	-	-	-
<b>LSD<sub>0,05</sub></b>	<b>1.28</b>	<b>1.99</b>	<b>1.30</b>	-	-	-	-	-

Note: Mean followed by the same letter is not significantly different within the columns according to LSD test at a 5% significance level; CV (coefficient variance).

The number of harvested spears of each crown in treatments had a significant difference. The treatments complemented with MOFs had higher number of harvested spears compared with the control (5.3 harvested spears.crown<sup>-1</sup>) and the Treat.5 had a highest harvest spears (7.9 harvested spears.crown<sup>-1</sup>), followed by Treat.4 (6.8 harvested spears.crown<sup>-1</sup>), Treat.3 (6.1 harvested spears.crown<sup>-1</sup>), Treat.2 (5.63 harvested spears.crown<sup>-1</sup>). The diameter and weight of harvested spears in treatments supplemented with MOFs were also higher than those in the control, but the difference was not statistical significant. However, the harvested spears of Treat.5 possessed the best diameter and weight (8.8 mm and 12.55 g.spear<sup>-1</sup>, respectively), followed by Treat.4 (8.58mm and 12.5 g.spear<sup>-1</sup>), Treat.3 (7.39 mm and 11.77 g.spear<sup>-1</sup>), Treat.2 (7.29 mm and 11.04 g.spear<sup>-1</sup>) and the smallest harvested spears in control (6.89 mm and 9.31 g.spear<sup>-1</sup>, respectively).

The data collected from 15 asparagus crowns of each treatment showed that the total number of harvested spears and the rate of spear market grades at treatments supplemented with MOFs were higher than those in the control. Treat.5 had the best results (115 harvested spears, 44.44% grade I spears and 38.89% grade II spears), followed by Treat.4 (100 harvested spears, 31.58% grade I spears and 57.89% grade II spears). Asparagus spear yield for one harvest month was highest in Treat.5 (1.6 tons.ha<sup>-1</sup>.month<sup>-1</sup>), followed by Treat.4 (1.39 tons.ha<sup>-1</sup>.month<sup>-1</sup>), Treat.3 (1.18 tons.ha<sup>-1</sup>.month<sup>-1</sup>), treat.2 (1.04 tons.ha<sup>-1</sup>.month<sup>-1</sup>) and the lowest spear yield in control (0.78 tons.ha<sup>-1</sup>.month<sup>-1</sup>).

The experimental results could be explained by the supplemental MOFs, especially Song Gianh MOF and Que Lam 01 MOF that provide nutrients and other utilities. The additional microbiome promote metabolizing nutrients,<sup>13</sup> fixing nitrogen.<sup>17</sup> Moreover, the

humic acid enhances micro and macronutrients absorption.<sup>18</sup> These factors consequently increase the chlorophyll content, synthesis of organic compounds,<sup>19</sup> and nutrient accumulation in the spears. So, the diameter, weight and number of harvested spears were enhanced.

### 3.5. Asparagus spear quality

The analysis data of asparagus spear quality was presented in Table 6. The dry matter content of spears ranged from 8.34 to 9.54% and the treatments supplemented with MOF had higher dry matter content than that in control, but there is not statistically significant difference. The fiber content of spears (2.0 - 2.2%) and total protein (1.8 - 2.2%) decreased slightly in the treatments supplemented with MOFs, but the difference was not statistical significant. The vitamin C content of asparagus spears in treatments supplemented with MOF is higher than that in control (278 mg.100 g<sup>-1</sup> fresh spears) and Treat.5 had the highest content (341 mg.100 g<sup>-1</sup> fresh spears).

**Table 6.** Effect of MOFs on quality characteristics of asparagus spears

Treat.	Dry matter content (%)	Fiber content (%)	Total protein content (%)	Vitamin C (mg.100g <sup>-1</sup> )
Treat.1	8.34 <sup>b</sup>	2.2	2.2	278
Treat.2	9.16 <sup>ab</sup>	2.2	2.1	282
Treat.3	9.26 <sup>ab</sup>	2.1	2.0	321
Treat.4	9.59 <sup>a</sup>	2.1	2.1	318
Treat.5	9.54 <sup>a</sup>	2.0	1.8	341
CV(%)	<b>6.68</b>	-	-	-
LSD <sub>0.05</sub>	<b>1.12</b>	-	-	-

Note: Mean followed by the same letter is not significantly different within the columns according to LSD test at a 5% significance level; CV (coefficient variance).

**3.6. Profit of asparagus cultivation**

**Table 7.** Effect of MOFs on cost and profit of asparagus cultivation

*Unit: 1,000 VND*

<b>Treat.</b>	<b>Treat. 1</b>	<b>Treat. 2</b>	<b>Treat. 3</b>	<b>Treat. 4</b>	<b>Treat. 5</b>
<b>Costs</b>					
Crowns	360	360	360	360	360
NPK fertilizer	43.2	43.2	43.2	43.2	43.2
Labor	200	200	200	200	200
Manure	84	84	84	84	84
Trichoderma	75	75	75	75	75
Other costs	70	70	70	70	70
MOF	0	390	300	576	540
<b>Total cost</b>	<b>832</b>	<b>1,222</b>	<b>1,132</b>	<b>1,408</b>	<b>1,372</b>
<b>Total income</b>	<b>105</b>	<b>129</b>	<b>138</b>	<b>203</b>	<b>214</b>
<b>Profit compared with control</b>	<b>0</b>	<b>24</b>	<b>33</b>	<b>98</b>	<b>109</b>

Note: Asparagus spear price of current market at Quy Nhon city): Grade I (120,000 VND.kg<sup>-1</sup>), Grade II (70,000 VND.kg<sup>-1</sup>), Grade III (40,000 VND.kg<sup>-1</sup>).

Asparagus culture needs a high initial investment but the harvest time is long, possibly up to 5-7 years.<sup>7</sup> Total cost and total income (for a harvest month) in treatments are shown in the Table.7. Research data shows that the profit of treatment complemented with MOF is higher than that in control. The highest profit is in Treat.5 (109,000 VND), followed Treat.4 (98,000 VND), Treat.3 (33,000 VND) and Treat.2 (24,000 VND).

**4. CONCLUSIONS**

MOF complementation, especially Song Gianh MOF during asparagus cultivation stages initially enhanced the stem height, stem diameter, chlorophyll content, number of stems (7.62 stems.crown<sup>-1</sup>), number of harvested spears (7.9 harvested spears.crown<sup>-1</sup>), average spear diameter (reaching to 8.8 mm), spear weight (12.55 g.spear<sup>-1</sup>), vitamin C content (reaching 341 mg.100g<sup>-1</sup>), asparagus spear yield reaching 1.6

tons.ha<sup>-1</sup> for one harvest month. It is proposed to continue further studies on using supplemental Song Gianh MOF in the cultivation process of Netherland F1 Radius green asparagus to assess completely its suitability for asparagus cultivation conditions in Quy Nhon city, Binh Dinh province.

**Acknowledgements:** *This research is conducted within the framework of science and technology projects at institutional level of Quy Nhon University under the project code T2020.665.13.*

**REFERENCES**

1. J. Schwarz, E. Mathijs. Globalization and the sustainable exploitation of scarce groundwater in coastal Peru, *Journal of Cleaner Production*, **2017**, *147*, 231-241.
2. S. Hu. Asparagus - the king of vegetables, *China Inspection and Quarantine*, **2000**, *46* [in Chinese].
3. C. Jiménez-Sánchez, J. Lozano-Sánchez, C. Rodríguez-Pérez, A. Segura-Carretero, A. Fernández-Gutiérrez. Comprehensive, untargeted, and qualitative RP-HPLC-ESI-QTOF/MS2 metabolite profiling of green asparagus (*Asparagus officinalis*), *Journal of Food Composition and Analysis*, **2015**, *46*, 78-87.
4. A. E. Al-Snafi. The pharmacological importance of *Asparagus officinalis* – A review, *Journal of Pharmaceutical Biology*, **2015**, *5*(2), 93-98.
5. Q. Guo, N. Wang, H. Liu, Z. Li, L. Lu and C. Wang. The bioactive compounds and biological functions of *Asparagus officinalis* L. – A review, *Journal of Functional Foods*, **2020**, *65*, 103727.
6. J. S. Negi, et al. Chemical constituents of Asparagus, *Pharmacogn Rev*, **2010**, *4*(8), 215-220.
7. L. Cam and Le Hong Trieu. *Techniques for planting and growing green asparagus (Asparagus)*, Hai Phong publishing house, 2011 [in Vietnamese].
8. Le Thi Thu Tra. *Micro-organic fertilizers and bio-organic fertilizers in agricultural production*,

- Western highlands Agriculture and forestry science Institute (WASI), 2016 <<http://wasi.org.vn/phan-huu-co-vi-sinh-va-huu-co-sinh-hoc-trong-san-xuat-nong-nghiep/>>, accessed on 2<sup>nd</sup> December 2020 [in Vietnamese].
9. Nguyen The Dang, Nguyen Tuan Anh, Nguyen Duc Nhuan and Nguyen Thi Mao. *Organic agriculture textbook*, Agricultural publishing house, Hanoi, 2012 [in Vietnamese].
  10. C. Lazcano, M. Gómez-Brandón, P. Revilla, J. Domínguez. Short-term effects of organic and inorganic fertilizer on soil microbial community structure and function, *Biol Fertil Soils*, **2012**, *49*, 723–733.
  11. C.-c. Ning, P.-d. Gao, B.-q. Wang., W.-p. Lin, N.-h. Jiang, and K.-z. Cai. Impacts of chemical fertilizer reduction and organic amendments supplementation on soil nutrient, enzyme activity and heavy metal content, *Journal of Integrative Agriculture*, **2017**, *16*(8), 1819-1831.
  12. M. Diacono, F. Montemurro. Long-term effects of organic amendments on soil fertility, A review, *Agronomy for Sustainable Development*, **2010**, *30*, 401-422.
  13. Pham Tien Hoang. Organic fertilizers in the integrated plant nutrient management system. *Journal of Soil Science*, **2003**, *8*, 120 – 126 [in Vietnamese].
  14. H. Ke, H. HuaXing, L. WeiSheng, L. YuanJin, W. LiBin. Effect of microbial organic fertilizer application on soil microbial activity, *Chinese Journal of Eco-Agriculture*, **2010**, *18*(2), 303-306.
  15. Nguyen Van Tam. *Techniques for planting and asparagus intensive farming (Internal documentation)*, Linh Dan Ninh Thuan Co. Ltd., 2017 [in Vietnamese].
  16. C. Quansheng. Technical specifications about control of diseases and pests in green asparagus, *Anhui Agricultural Science Bulletin*, **2007**, *18*.
  17. K. Blankenau, H.W. Kuhlmann, H. Olf. Effect of microbial nitrogen immobilization during the growth period on the availability of nitrogen fertilizer for winter cereals, *Biology and Fertility of Soils*, **2000**, *32*, 157–165.
  18. Z. Varanini and R. Pinton. *Humic acid substances and plant nutrition*, In: Behnke HD., Lüttge U., Esser K., Kadereit J.W., Runge M. (eds) *Progress in Botany*, Springer, Berlin, 1995.
  19. Y. Chen, C. Clapp, H. Magen. Mechanisms of plant growth stimulation by humic substances: the role of organo-iron complexes, *Soil Science and Plant Nutrition*, **2004**, *50*, 1089 -1095.
  20. S. Nardi, D. Pizzeghello, A. Muscolo, A. Vianello. Physiological effects of humic substances on higher plants, *Soil Biology and Biochemistry*, **2002**, *34*, 1527–1536.
  21. H. Marchner. *Mineral nutrition of higher plant*, Institute of plant University of Hohenheim Federal Republic of Germany, 1996.

# Sự hội tụ địa phương của một kiểu phương pháp Newton gần đúng sử dụng mô hình tối ưu trong bài toán con

Trần Ngọc Nguyên, Nguyễn Văn Vũ\*

*Khoa Toán và Thống kê, Trường Đại học Quy Nhơn, Việt Nam*

*Ngày nhận bài: 23/02/2021; Ngày nhận đăng: 26/04/2021*

## TÓM TẮT

Bài báo này tập trung vào nghiên cứu lược đồ lặp kiểu Newton gần đúng giải các phương trình suy rộng bao hàm ánh xạ đa trị trong trường hợp hữu hạn chiều. Chúng tôi đề xuất một chiến lược cập nhật động các bước lặp mới bằng cách đưa vào tại mỗi bước một mô hình quy hoạch toán học dựa trên dạng tuyến tính hóa của phần đơn trị xuất hiện trong phát biểu bài toán gốc. Chúng tôi cũng đưa ra kết quả phân tích hội tụ địa phương của lược đồ được đề xuất và áp dụng để xây dựng một thuật toán cấu trúc cho một lớp quan trọng là các bài toán bù. Một vài thực nghiệm số cũng được xem xét nhằm đánh giá bước đầu tính khả thi thực tiễn của phương pháp.

**Từ khóa:** *Ánh xạ đa trị, phương trình suy rộng, phương pháp Newton, tính nửa ổn định.*

---

\*Tác giả liên hệ chính.

Email: [nguyenvanvu@qnu.edu.vn](mailto:nguyenvanvu@qnu.edu.vn)

# Local convergence of an inexact Newton-type method involving optimization model on subproblems

Tran Ngoc Nguyen, Nguyen Van Vu\*

*Faculty of Mathematics and Statistics, Quy Nhon University, Vietnam*

*Received: 23/02/2021; Accepted: 26/04/2021*

## ABSTRACT

This paper deals with inexact Newton-type scheme for solving generalized equation governed by set-valued mappings defined on finitely dimensional spaces. We proposed a new dynamical updating strategy by adapting in a mathematical program modeling based on the linearization of the single-valued part at each step. We investigated the local convergence behavior of the proposed framework and applied it to design a structural algorithm for solving complementarity problems. Implementation of several numerical tests was also considered to illustrate the feasibility of such framework.

**Keywords:** *Set-valued mapping, generalized equation, Newton-type method, semistability.*

## 1. INTRODUCTION

The Newton (or Newton-Raphson) method together with its extensions have been well-known in the literature as among of popular and efficient strategies for finding the zeros to a system of nonlinear functions. This is due to the good behavior of concrete algorithms designed from such manner, especially, the high growth of the convergence under mild assumptions on the input data. particularly, when the functions defining the system are sufficiently smooth (of  $C^{1,1}$  class for example), the corresponding Newton-based algorithms might be locally quadratically convergent (see<sup>1</sup>).

As motivated from certain problems in applications, many authors have extended the classical Newton framework to deal with the general model called by *generalized equation* (GE). Mathematically, an abstract GE defined on finite dimensional spaces can be formulated as inclusions involved set-valued map

$$0 \in \Phi(x) + N(x), \quad (1)$$

where, the single-valued term  $\Phi : \mathbb{R}^n \rightarrow \mathbb{R}^m$  is assumed to be smooth up to the necessary order, and

the set-valued part  $N : \mathbb{R}^n \rightrightarrows \mathbb{R}^m$  has closed graph. Problem of type (1) covers many concrete situations under the suitable choice of  $N$ . One of the most important case is the variational inequalities<sup>2</sup> which is closely related to mathematical program induced by selecting  $N$  to be the normal cone mapping associated with feasible region. For the sack of further reading, we refer to.<sup>1,3</sup> and the references therein.

One of the earliest framework dealing with abstract problem (1) is the famous Josephy-Newton method.<sup>1,4</sup> The core idea behind is to perturb (1) by replacing  $\Phi$  with its linearization at each step and searching the next iterate as a solution to the auxiliary problem

$$0 \in \Phi(x^k) + \Phi'(x^k)(x - x^k) + N(x). \quad (2)$$

Here and in what follows,  $x^k$  is meant to be the  $k^{\text{th}}$  iterate of the principal loop, and  $\Phi'$  stands for the first-order derivative of  $\Phi$ . More general, (2) can be subsumed as a particular case of the following scheme

$$0 \in A(x^k, x) + N(x), \quad (3)$$

in which a perturbed term  $A(x^k, \cdot)$  is in the position of  $\Phi$ . (The typical Josephy-Newton framework

---

\*Corresponding author.

Email: [nguyenvanvu@qnu.edu.vn](mailto:nguyenvanvu@qnu.edu.vn)

is induced from (3) if we let  $A(u, v) = \Phi(u) + \Phi'(u)(v-u)$ . Under some mild assumptions, the reference methods will produce an iterative sequence  $(x^k)$  that converges to a solution of (1) with linear/superlinear/quadratic rate. The readers should consult<sup>1,3,5,6</sup> and the references therein for more about those topics.

As mentioned in,<sup>1</sup> one of the sharpest trend for the study of local convergence of (2) was appeared in the work,<sup>7</sup> and then, was considered in the later paper.<sup>8</sup> Another line for dealing with (2), sometimes is said to be semilocal convergence result, was begun at least from the work,<sup>9</sup> and then, by some later ones, e.g.<sup>6,10,11</sup> Perhaps the major difference between the two aforementioned strategies is that, the local convergence involves the information concerning an existing solution, while the other one almost concentrates on initial guess point.

Toward the numerical implementation aspect, the Newton-type frameworks mentioned above operate as follows: after getting an iterate, one constructs a partial linearization system corresponding to the original problem, and then solve exactly the immediate system to produces the next step. (Particularly, (2) and (3) are typical in such a manner.) Being quite different, some authors proposed several inexact schemes in order to solve variational inclusion (1). For instance, the paper<sup>12</sup> introduced an abstract iterative scheme based on the subproblem

$$(\Phi(x^k) + \Phi'(x^k)(x - x^k) + N(x)) \cap R_k(x^k, x) \neq \emptyset \quad (4)$$

for a family of set-valued maps  $R_k : \mathbb{R}^n \times \mathbb{R}^n \rightarrow \mathbb{R}^m$ . While the authors<sup>1</sup> developed the algorithms for (1) using the updating process obtained by considering the perturbed inclusion

$$0 \in \Phi(x^k) + \Phi'(x^k)(x - x^k) + \Omega(x^k, x - x^k) + N(x) \quad (5)$$

whenever  $x^k$  is present. The inexact models allow us to apply suitably dynamical strategy of selecting the solvers to handle auxiliary problems that still ensure the convergence of overall process.

The current paper follows the idea of inexact Newton-type methods proposed in the literature with a few relaxations. Suppose now an iterate  $x^k \in \mathbb{R}^n$  is known, then we would compute next step  $x^{k+1}$  via the perturbed GE

$$0 \in \Phi(x^k) + \Phi'(x^k)(x^{k+1} - x^k) + w^k + N(x^{k+1}), \quad (6)$$

for a perturbation term  $w^k \in \mathbb{R}^m$ . The performance of the overall procedure is strongly concerned with

how efficiently one selects  $w^k$  and solve the inclusion (6). For instance, with aim of obtaining locally superlinear convergence of the resulting sequence  $(x^k)$ , we can require that  $w^k$  satisfies the condition

$$\|w^k\| = o(\|x^{k+1} - x^k\| + \|x^k - x^*\|) \quad (7)$$

as mentioned,<sup>1</sup> where  $x^*$  is assumed to be an existing solution. Unfortunately, this dynamical choice for  $w^k$  seems to be slightly difficult to verify in practice, since it involves a posterior estimation. To avoid that drawback, we proposed a modified version of (7) by solving simultaneously  $x^{k+1}$  and  $w^k$  with some additional constraints. Precisely, let us introduce several auxiliary variables  $d := x - x^k$ ,  $z \in \mathbb{R}^n$  and consider the optimization problem

$$\begin{aligned} \min_{t \geq 0} \quad & t \\ \text{subject to} \quad & \Phi(x^k) + \Phi'(x^k)(d) + w + z = 0, \\ & \|w\|^2 - t\|d\|^2 \leq 0, \\ & z \in N(x^k + d), \end{aligned} \quad (8)$$

for unknowns  $t, d, w$  and  $z$ . Once an exact/inexact solution to (8) is found, we update the next step  $x^{k+1} = x^k + d^k$  ( $d^k$  is extracted from the previous procedure) and continue. Note that if (7) does hold, problem (8) will admit a feasible solution  $(t_k, d^k, w^k, z^k)$  such that  $t_k \downarrow 0$ . This demonstrates the possibility of implementing (8) in practice with the help of available optimization solvers.

The paper is organized as follows. In the next section we recall some basic notions used throughout the paper. Section 3 is devoted to introduce our generally inexact Newton-type framework and investigate its local convergence. In Section 4, we apply our method to a concrete important class of variational problem. The last section presents some numerical experiments to consider the practical performance of algorithms based on our approach.

## 2. PRELIMINARIES

For the convenience of reading, we start by recalling some notions that will be used through the paper. The convention of notations used in the monograph will be applied throughout the paper. We frequently work with the a set-valued map  $N : \mathbb{R}^n \rightrightarrows \mathbb{R}^m$  assigning to each  $x \in \mathbb{R}^n$  a subset  $N(x) \subset \mathbb{R}^m$  (may be empty). Such an object could be identified with its graph, defined by  $\text{Gr}(N) := \{(x, y) \in \mathbb{R}^n \times \mathbb{R}^m \mid y \in N(x)\}$ . For any usual map  $\Phi : \mathbb{R}^n \rightarrow \mathbb{R}^m$  (equivalent terminology single-valued map), its (Fréchet) derivative will be denoted by  $\Phi'$ . While, notation  $\Phi''$  is meant to be

the second-order corresponding derivative. When  $\Phi$  is real-valued, we write  $\nabla\Phi(x)$  and  $\nabla^2\Phi(x)$  respectively to indicate its gradient vector and Hessian matrix at a given point  $x$ . Conventionally, all single-valued maps appeared in the paper are assumed to be differentiable up to the necessary order.

The problem of our interest is an abstract GE of the form

$$0 \in \Phi(x) + N(x), \tag{9}$$

where  $\Phi : \mathbb{R}^n \rightarrow \mathbb{R}^n$  is a smooth map, and  $N : \mathbb{R}^n \rightrightarrows \mathbb{R}^n$  is set-valued whose graph is a closed set. The closedness assumption to  $\text{Gr}(N)$  allows for preserving the inclusion involving  $N$  after passing to the limit. We are interested in the iterative scheme governed by solving the subproblem of the form

$$0 \in \Phi(x^k) + \Phi'(x^k)(x - x^k) + \Omega(x^k, x - x^k) + N(x), \tag{10}$$

for some set-valued term  $\Omega : \mathbb{R}^n \times \mathbb{R}^n \rightrightarrows \mathbb{R}^n$ . To study the convergence behavior of such scheme, the next definition is useful.

**Definition 1** (Semistable solution,<sup>1</sup>). Suppose that  $x^* \in \mathbb{R}^n$  is a solution to GE (9).  $x^*$  is said to be semistable if for every  $r \in \mathbb{R}^n$  any solution  $u(r)$  to the perturbed inclusion

$$r \in \Phi(x) + N(x) \tag{11}$$

being close enough to  $x^*$  satisfies the estimate

$$\|u(r)\| = O(\|r\|) \text{ as } \|r\| \rightarrow 0. \tag{12}$$

Concern Definition 1, the next result is fruitful when dealing with the local convergence analysis of scheme updated through (10).

**Theorem 2** (<sup>1</sup> Theorem 3.6). Let  $x^*$  be a semistable solution to the GE (9) for which the derivative  $\Phi'$  is continuous at  $x^*$ . Let  $\Omega : \mathbb{R}^n \times \mathbb{R}^n \rightrightarrows \mathbb{R}^n$  be a set-value map satisfying the following assumption: for  $x$  close enough to  $x^*$ , the GE

$$0 \in \Phi(x) + \Phi'(x)(u) + \Omega(x, u) + N(x + u) \tag{13}$$

has a solution  $u(x)$  such that  $u(x) \rightarrow 0$  as  $x \rightarrow x^*$  and the estimate

$$\|\omega\| = o(\|u\| + \|x - x^*\|) \tag{14}$$

holds as  $x \rightarrow x^*$ ,  $u \rightarrow 0$  uniformly for  $\omega \in \Omega(x, u)$ ,  $x \in \mathbb{R}^n$ ,  $u \in \mathbb{R}^n$  obeying the inclusion

$$0 \in \Phi(x) + \Phi'(x)(u) + \omega + N(x + u). \tag{15}$$

Then there exists  $\delta > 0$  such that for any starting point  $x^0 \in \mathbb{R}^n$  close enough to  $x^*$ , there exists a sequence  $(x^k) \subset \mathbb{R}^n$  such that  $x^{k+1}$  is a solution to the GE (10) for each  $k = 0, 1, 2, \dots$ , satisfying

$$\|x^{k+1} - x^k\| \leq \delta. \tag{16}$$

For any such sequence,  $x^k$  converges to  $x^*$  superlinearly. Moreover, the rate of convergence is quadratic provided the derivative  $\Phi'$  is locally Lipschitz-continuous with respect to  $x^*$ , and provided (14) can be replaced with the estimate

$$\|\omega\| = O(\|u\|^2 + \|x - x^*\|^2). \tag{17}$$

Here, superlinear rate of convergence is meant to be  $x^k \rightarrow x^*$  with

$$\limsup_{k \rightarrow \infty} \frac{\|x^{k+1} - x^*\|}{\|x^k - x^*\|} = 0. \tag{18}$$

If the relation

$$\limsup_{k \rightarrow \infty} \frac{\|x^{k+1} - x^*\|}{\|x^k - x^*\|^2} < +\infty \tag{19}$$

is in position of (18), one says that  $x^k \rightarrow x^*$  quadratically. Further, local Lipschitz continuity of  $\Phi'$  w.r.t  $x^*$  is equivalent to the assertion that

$$\limsup_{x \neq x' \rightarrow x^*} \frac{\|\Phi'(x) - \Phi'(x')\|}{\|x - x'\|} < +\infty. \tag{20}$$

### 3. LOCAL ANALYSIS FOR A CLASS OF INEXACT JOSEPHY-NEWTON METHOD VIA OPTIMIZATION MODEL

The current section is devoted to study an iterative scheme of inexact type for solving GE (9) by modifying the well-known Josephy-Newton method in the literature (see more, e.g.<sup>4,6</sup>). Such a framework based on the optimization model (8) in order to update  $x^{k+1} = x^k + d^k$ , where  $d^k$  is computed from an exact/approximating optimum to the nonlinear programming

$$\begin{aligned} \min_{t \geq 0} \quad & t \\ \text{s.t.} \quad & \Phi(x^k) + \Phi'(x^k)(d) + w + z = 0 \\ & d^T d \leq \rho_k^2 \\ & w^T w - t d^T d \leq 0 \\ & z \in N(x^k + d), \end{aligned} \tag{21}$$

where  $(\rho_k)$  is a positive sequence that determines the upper bound for actual step  $d^k$ . Comparing with (8), such a constraint is included to avoid the quite long step and ensure the local convergence property. This model can be viewed as a relaxation of the original subproblem involved in the Josephy-Newton scheme

$$0 \in \Phi(x^k) + \Phi'(x^k)(x - x^k) + N(x) \tag{22}$$

after adding the slack variable  $w$ . Also, (21) is subsumed as a particular case to (18), where  $\Omega(x^k, x - x^k)$  coincides with the  $w$  component of feasible region to problem (21). Algorithm 1 outlines the overall process of our proposed method.



**Remark 3.** The core phase in Algorithm 1 is subproblem defined in (21) which simultaneously generates both the search direction  $d$  and the term of inexactness  $w$ . This is slightly different from the strategy given by (10), where the suitable candidate for  $w$  should be chosen via an existing set-valued map  $\Omega$ . To the practical implementation aspect, our proposed algorithm using optimization model (21) is quite flexible rather than the one by means of (10). Nevertheless, the performance of overall process depends on how efficient we solve (21). Further, for concrete applications, it is also necessary to invoke some reasonable globalization framework in order to avoid the sensitivity when dealing with difficult problems. Those issues should not be in the scope of this paper, and for the analysis here, we assume in general that any of subproblem (21) is solved successfully throughout the principal loop of Algorithm 1.

Concern the behavior of Algorithm 1, we consider some assumptions below.

- (A1). The sequence of parameters  $(\rho_k)$  appear in model (21) is chosen in some manner such that  $\rho_k \downarrow 0$ .
- (A2). The mathematical program (21) admits at least one (optimal or almost optimal) solution that can be successfully computed at each step.
- (A3). The optimal value  $t_k^{opt}$  returned by solving (21) satisfies

$$\limsup_{k \rightarrow \infty} \{t_k^{opt}\} = 0. \tag{23}$$

```

input :  $x^0, \Phi, N$ 
output: sequence  $x^0, x^1, x^2, \dots$ 
 $k \leftarrow 0$ ;
repeat /*principal loop*/
    Set up the model (21);
    Solve the model (exact/inexact);
    if solve (21) successfully then
        Extract  $d^k$  from solution to (21);
        Update  $x^{k+1} \leftarrow x^k + d^k$ ;
         $k \leftarrow k + 1$ 
    else /*subproblem fail*/
        Terminate the loop;
    endif
until stopping criterion reached; /*end loop*/
    
```

**Algorithm 1.** Inexact Newton-type method involving optimization model of subproblems

The next theorem summarizes the local convergence result for the proposed method based on Algorithm 1.

**Theorem 4** (Local analysis for Algorithm 1). *Consider GE (9) whose single-valued part  $\Phi$  is differentiable. Let  $x^*$  be semistable in the sense of Definition 1 and  $\Phi'$  be continuous around  $x^*$ . If all assumptions (A1), (A2) and (A3) are fulfilled, then by starting at  $x^0$  being close enough to  $x^*$ , the sequence  $(x^k)$  generated via Algorithm 1 converges to  $x^*$  superlinearly.*

*Proof.* We notice first that, if we set

$$r^k := \Phi(x^{k+1}) - \Phi(x^k) - \Phi'(x^k)(d^k) - w^k, \tag{24}$$

then it is obvious to see that  $x^{k+1}$  solves the GE

$$r^k \in \Phi(x) + N(x). \tag{25}$$

For the main proof, let us mimic the line of Theorem 2. Choosing some parameters  $\kappa > 0$  and  $0 < \delta, \epsilon < 1$  for which the following does hold: when  $\|r\| \leq 2\epsilon$ , any solution  $u(r)$  to the perturbed GE  $r \in \Phi(u) + N(u)$  with  $\|u(r) - x^*\| \leq 2\delta$  will satisfy the estimate

$$\|u(r) - x^*\| \leq \kappa \|r\|. \tag{26}$$

Scaling  $\epsilon > 0$  if necessary, we can suppose that

$$\|\Phi'(x) - \Phi'(x^*)\| \leq \delta, \forall \|x - x^*\| \leq 2\epsilon. \tag{27}$$

Finally, since  $\rho_k \downarrow 0$ , after skipping a few first indexes, it is possible to require  $\rho_k \leq \epsilon$ .

We now start by  $x^0$  such that  $\|x^0 - x^*\| \leq \epsilon$ . By assumption (A2), (21) produces some triplet  $(t_0, d^0, w^0)$  which solves the GE

$$0 \in \Phi(x^0) + \Phi'(x^0)(d^0) + w^0 + N(x^0 + d^0) \tag{28}$$

such that  $\|w^0\| \leq t_0 \|d^0\|$  and  $\|d^0\| \leq \rho_0$ . As mentioned at the beginning,  $x^1 = x^0 + d^0$  is a solution to the inclusion

$$r^0 \in \Phi(x) + N(x) \tag{29}$$

for  $r^0 = \Phi(x^1) - \Phi(x^0) - \Phi'(x^0)(d^0) - w^0$ . The Taylor's expansion applied to  $\Phi$  yields

$$r^0 = \int_0^1 \{[\Phi'(x^0 + sd^0) - \Phi'(x^0)](d^0)\} ds - w^0. \tag{30}$$

Because of  $\|x^0 - x^*\| \leq \epsilon$  and  $\|d^0\| \leq \rho_0$ , it does hold  $\|x^0 + sd^0 - x^*\| \leq 2\epsilon$  when  $s$  varies in the interval  $[0, 1]$ . Thus, the estimate

$$\|\Phi'(x^0 + sd^0) - \Phi'(x^*)\| \leq \delta \tag{31}$$

is straightforward for  $0 \leq s \leq 1$ . The combination between (27), (30) and (31) gives us

$$\|r^0\| \leq 2\delta \|d^0\| + \|w^0\| \leq (2\delta + t_0) \|d^0\|. \tag{32}$$

Hence, assumption of Theorem 4 implies  $\|r^0\| \leq 2\epsilon$ . Consequently, we obtain

$$\|x^1 - x^*\| \leq \kappa \|r^0\| \leq \kappa(2\delta + t_0) \|d^0\|. \tag{33}$$

Taking into account the inequality  $\|d^0\| \leq \|x^1 - x^*\| + \|x^0 - x^*\|$ , we deduce from (33)

$$\|x^1 - x^*\| \leq \frac{\kappa(2\delta + t_0)}{1 - \kappa(2\delta + t_0)} \|x^0 - x^*\| < \|x^0 - x^*\|, \tag{34}$$

if the following is active

$$2\kappa(2\delta + t_0) < 1. \tag{35}$$

Because  $\delta > 0$  can be made arbitrarily small and  $t_k^{opt} \downarrow 0$ , (35) could be supposed to satisfied.

In summary, under the condition (35) and  $\|x^0 - x^*\| \leq \epsilon$ , we obtain  $x^1$  via Algorithm 1 and moreover

$$\|x^1 - x^*\| \leq \sigma \|x^0 - x^*\| \tag{36}$$

for some  $0 \leq \sigma < 1$ . This shows that the process above still applicable if  $x^1$  is in position of  $x^0$ . As a result, the sequence  $(x^k)$  is well-defined with

$$\|x^{k+1} - x^*\| \leq \sigma \|x^k - x^*\|. \tag{37}$$

It can be derived from (37) that  $\|x^k - x^*\| \rightarrow 0$ . The superlinear rate of convergence is attained by applying the result presented in<sup>1</sup> Proposition 3.4.  $\square$

#### 4. APPLICATION TO NONLINEAR COMPLEMENTARITY PROBLEMS (NCPs)

The NCP corresponding to a smooth map  $F : \mathbb{R}^n \rightarrow \mathbb{R}^n$  could be formulated as follows (see, e.g.<sup>2</sup>)

$$x \geq 0, F(x) \geq 0, x^T F(x) = 0, \tag{38}$$

in which we denote as usual  $x^T$  the transpose of  $x$  being written as a column matrix. If  $F$  coincides with the gradient  $\nabla f$  to a smooth real-valued function  $f : \mathbb{R}^n \rightarrow \mathbb{R}$ , the NCP (38) reduces to the KKT system associated with minimization program<sup>1</sup>

$$\min_x f(x) \quad \text{s.t.} \quad x \geq 0. \tag{39}$$

By setting  $\Phi(x) = F(x)$  and

$$N(x) := \begin{cases} \{z \in \mathbb{R}^n \mid z \leq 0, z^T x = 0\}, & \text{if } x \geq 0 \\ \emptyset, & \text{otherwise,} \end{cases} \tag{40}$$

we recover GE (9) from (38). The optimization model (21) now reads

$$\begin{aligned} \min_{t \geq 0} \quad & t \\ \text{s.t.} \quad & F(x^k) + F'(x^k)(d) + w + z = 0 \\ & z^T(x^k + d) = 0 \\ & -d^T d + \rho_k^2 \geq 0 \\ & -w^T w + td^T d \geq 0 \\ & x^k + d \geq 0 \\ & -z \geq 0. \end{aligned} \tag{41}$$

<sup>1</sup>Homepage: <https://www.gnu.org/software/octave/>

Under such configuration, the iterative process to find a solution of (38) based on our proposed scheme is described in Algorithm 2.

```

input :  $x^0, F$ 
output: sequence  $x^0, x^1, x^2, \dots$ 
 $k \leftarrow 0$ ;
repeat                               /*principal loop*/
    Compute  $\rho_k$ ;
    Set up the model (41);
    Solve the model (exact/inexact);
    if successful solving then
        Extract  $d^k$  from solution to (41);
        Update  $x^{k+1} \leftarrow x^k + d^k$ ;
         $k \leftarrow k + 1$ ;
    else                               /*subproblem fail*/
        Terminate the loop;
    endif
until stopping criterion reached;
    
```

**Algorithm 2.** Inexact Newton-type method for NCP (38)

#### 5. NUMERICAL EXPERIMENTS

We implement Algorithm 2 with open-source software GNU Octave.<sup>1</sup> The testing model involving mathematical program (39) whose objective function  $f : \mathbb{R}^n \rightarrow \mathbb{R}$  belongs to the well-known family of Rosenbrock type<sup>13</sup>

$$f(x) := \sum_{i=1}^{n-1} [r(x_{i+1} - x_i^2)^2 + (x_i - 1)^2], \tag{42}$$

where  $r > 0$  is some parameter. Throughout the tests, each input sample is randomly generated via the built-in program `randn`. To handle subproblems in the form of (41), we invoke some certain hooking solvers `ipopt`,<sup>14</sup> `minos`,<sup>15</sup> `snopt`.<sup>16</sup> At the moment, we benchmark the performance by comparing several features:

- the number of samples that stops at successful criteria;
- the number of samples that assumptions (A2), (A3) are fulfilled throughout the principal loop.

To decide whether termination is optimal or not, we adopt the merit function  $\omega(x) = \|\text{diag}(x)F(x)\|$ , where  $\text{diag}(x)$  is the diagonal matrix whose diagonal entries are components of vector  $x$ . The threshold tolerance for stopping criteria maintained during the test is chosen as  $10^{-6}$ , while the maximum number of iterations in principal loops is set

to be 200. Here, we update dynamically  $\rho_{k+1} := \min(\rho_k, 1/\log(k + 1))$  and check assumption (A3) by comparing with the slowly convergent sequence  $e_k = 1/k$ . Tables 1 and 2 show the benchmarking results obtained after specific test which consists in  $N = 20$  samples of dimension  $n = 5$ .

Features	ipopt	minos	snopt
nb. optimal	4	2	3
nb. limit	16	12	6
nb. failure	0	6	11

**Table 1.** Numerical implementation of Algorithm 2: nb. optimal (resp.nb. limit,nb. failure) indicates the number of founding optimal iterate (reaching limit of threshold/updating fail)

Features	ipopt	minos	snopt
nb. valid	10	13	8
nb. failure	10	6	12
nb. other	0	1	0

**Table 2.** Information concern Assumption (A3): nb. valid (resp. nb. failure, nb. other) shows the number of samples that satisfy (resp. not satisfy, be unsure)

From Table 1, we can see that our proposed model works pretty well. More specifically, the percentage of problems which are successfully solved by our model combined with ipopt, (resp. minos and snopt) is 100%, (resp. 70% and 50%). This means that the successful rate of our model is more than 70%. It is worth noting that ipopt, minos and snopt are general-purposed solvers which are not properly designed for our new model. It is really interesting to propose a particular algorithm for solving (41) which is more efficient than these above solvers.

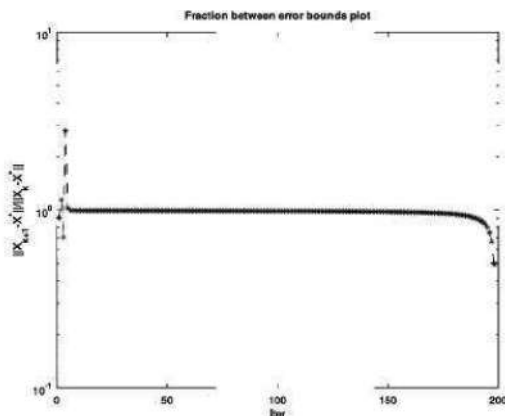


**Figure 1.** Superlinear convergence of Algorithm 2 with ipopt solver

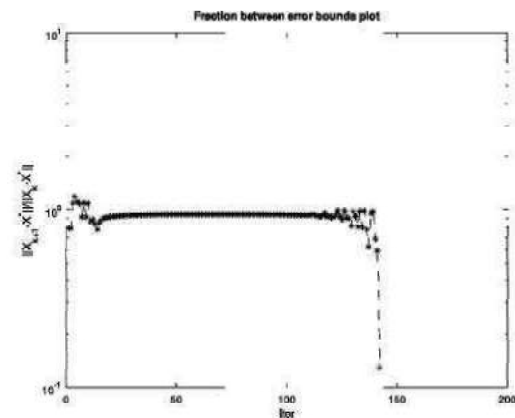


**Figure 2.** Superlinear convergence of Algorithm 2 with minos solver

Table 2 shows us the validity of assumption (A3). It can be seen that over 50% (31/60) of problems satisfy this assumption. According to Theorem 4, Algorithm 2 will attain a superlinear rate of convergence in these problems. To verify this assertion, we plot the behavior of Algorithm 2 when solving a problem satisfying assumption (A3) in Figures 1, 2 and 3. These figures give us the error distance of iterates in one certain successful sample that is extracted randomly. We can see that the error distances decrease faster and faster on last iterations. This implies the superlinear convergence in the corresponding cases.

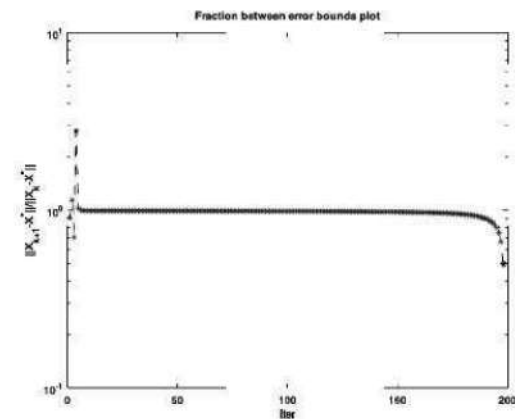


**Figure 3.** Superlinear convergence of Algorithm 2 with snopt solver

**Remark 5.** In Table 2 the only of interest is actually Assumption (A3), because the lack of validity for Assumption (A2) is almost the same with failure of overall process given in Table 1.

**Acknowledgments:** *This research is conducted within the framework of science and technology projects at institution level of Quy Nhon University under the project code T2020.653.01.*

REFERENCES

1. A. F. Izmailov and M. V. Solodov, *Newton-type methods for optimization and variational problems*, Springer International Publishing, 2014.
2. F. Facchinei and J.-S. Pang, *Finite-dimensional variational inequalities and complementarity problems, Vol I*, 1<sup>st</sup> edition, Springer-Verlag New York, 2003.
3. A. L. Dontchev and R. T. Rockafellar, *Implicit functions and solution mappings: A view from variational analysis*, 2<sup>nd</sup> edition, Springer-Verlag New York, 2014.
4. N. H. Josephy, Newton's method for generalized equations, Technical report, University of Wisconsin, Madison, 1979.
5. S. Adly, R. Cibulka, and H. V. Ngai, Newton's method for solving inclusions using set-valued approximations, *SIAM J. Optim.*, **2015**, *25*, 159–184.
6. R. Cibulka, A. L. Dontchev, J. Preininger, V. Veliov, and T. Roubal, Kantorovich-type theorems for generalized equations, *J. Convex Anal.*, **2018**, *25*, 459–486.
7. J. F. Bonnans, Local analysis of Newton-type methods for variational inequalities and nonlinear programming, *Appl. Math. Optim.*, **1994**, *29*, 161–186.
8. A. F. Izmailov, A. S. Kurennoy, and M. V. Solodov, The Josephy–Newton method for semismooth generalized equations and semismooth SQP for optimization, *Set-Valued Var. Anal.*, **2013**, *21*, 17–45.
9. A. L. Dontchev, *Local analysis of a Newton-type method based on partial linearization*, The mathematics of numerical analysis. 1995 AMS-SIAM summer seminar in applied mathematics, July 17–August 11, 1995, Park City, UT, USA. Providence, RI: American Mathematical Society, 1996, 295–306.
10. S. Adly, H. V. Ngai, and V. V. Nguyen, Newton's method for solving generalized equations: Kantorovich's and Smale's approaches, *J. Math. Anal. Appl.*, **2016**, *439*, 396–418.
11. M. H. Rashid, S. H. Yu, C. Li, and S. Y. Wu, Convergence analysis of the Gauss–Newton-type method for Lipschitz-like mappings, *J. Optim. Theory Appl.*, **2013**, *158*, 216–233.
12. A. L. Dontchev and R. T. Rockafellar, Convergence of inexact Newton methods for generalized equations, *Math. Program.*, **2013**, *139*, 115–137.
13. H. H. Rosenbrock, An automatic method for finding the greatest or least value of a function, *The Computer Journal*, **1960**, *3*, 175–184.
14. A. Wächter and L. T. Biegler, On the implementation of an interior-point filter line-search algorithm for large-scale nonlinear programming, *Math. Program.*, **2006**, *106*, 25–57.
15. B. A. Murtagh and M. A. Saunders, *A projected Lagrangian algorithm and its implementation for sparse nonlinear constraints*, Berlin, Heidelberg: Springer Berlin Heidelberg, 1982, 84–117.
16. P. E. Gill, W. Murray, and M. A. Saunders, Snopt: An sqp algorithm for large-scale constrained optimization, *SIAM Review*, **2005**, *47*, 99–131.

## VỀ MỘT PHƯƠNG TRÌNH MA TRẬN

Nguyễn Duy Ái Nhân<sup>1,\*</sup>, Dư Thị Hòa Bình<sup>2</sup>

<sup>1</sup> Khoa Toán, Trường Đại học Khoa học, Đại học Huế, Huế, Việt Nam

<sup>2</sup> Khoa Quản trị Kinh doanh và Du lịch, Trường Đại học Hà Nội, Hà Nội, Việt Nam

Ngày nhận bài: 29/03/2021; Ngày nhận đăng: 26/04/2021

### TÓM TẮT

Trong bài báo này, chúng tôi chỉ ra rằng với  $A, B$  là các ma trận xác định dương và  $M_1, M_2, \dots, M_m$  là các ma trận không suy biến thì phương trình ma trận

$$X^p = A + \sum_{i=1}^m M_i^T \left( B^{\frac{1-t}{2t}} X B^{\frac{1-t}{2t}} \right)^t M_i$$

có nghiệm xác định dương duy nhất  $X^*$ . Ngoài ra, bằng cách sử dụng phương pháp lặp, chúng tôi cũng chỉ ra dãy các ma trận hội tụ về nghiệm  $X^*$  của phương trình trên.

**Từ khóa:** Ma trận xác định dương, phương trình ma trận, định lý điểm bất động, phương pháp lặp.

---

\*Tác giả liên hệ chính.  
Email: nguyenduyainhan@husc.edu.vn

## On a matrix equation

Nguyen Duy Ai Nhan<sup>1,\*</sup>, Du Thi Hoa Binh<sup>2</sup>

<sup>1</sup> Department of Mathematics, University of Sciences, Hue University, Hue, Vietnam

<sup>2</sup> Faculty of Management and Tourism, Hanoi University, Hanoi, Vietnam

Received: 29/03/2021; Accepted: 26/04/2021

### ABSTRACT

In this paper, we consider one matrix equation that involves a matrix generalization of the the weighted geometric mean. More precisely, for positive definite matrices  $A$  and  $B$ , for nonsingular matrices  $M_1, M_2, \dots, M_m$ , we show that the following equation

$$X^p = A + \sum_{i=1}^m M_i^T \left( B^{\frac{1-t}{2i}} X B^{\frac{1-t}{2i}} \right)^t M_i$$

has a unique positive definite solution. We also study the multi-step stationary iterative method for this equation and prove the corresponding convergence.

**Keywords:** Positive definite matrix, matrix equation, fixed point theorem, multi-step stationary iterative method.

### 1. INTRODUCTION

Let  $\mathbb{M}_n$  stand for the algebra of  $n \times n$  complex matrices and let  $\mathcal{P}_n$  denote the normal cone of positive definite matrices in  $\mathbb{M}_n$ . Let  $f$  be a real-valued function which is well-defined on the set of eigenvalues of a Hermitian matrix  $A$ . Then the matrix  $f(A)$  can be defined by means of the functional calculus.

Let  $A, B$  be positive definite matrices, it is well-known that the matrix geometric mean  $A\sharp B = A^{1/2} (A^{-1/2} B A^{-1/2})^{1/2} A^{1/2}$  was firstly defined<sup>1</sup> by Pusz and Woronowicz. They showed that the geometric mean is the unique positive definite solution of the Riccati equation

$$XA^{-1}X = B. \tag{1}$$

In 2005, Lim<sup>2</sup> studied the inverse means problem for the geometric mean and the contra-harmonic mean. Using the Riccati equation (1) as a lemma, for positive definite matrices  $A \leq B$  he studied the following equation

$$X = A + 2BX^{-1}B.$$

He showed that the last equation has a unique positive solution of the form  $X = \frac{1}{2} (A + A\sharp(A + 4BA^{-1}B))$ . Lim and co-authors<sup>3</sup> studied the non-linear equation

$$X = B\sharp(A + X).$$

They proved that this equation has a unique positive definite solution  $X = \frac{1}{2}(B + B\sharp(B + 4A))$ . Interestingly, both results were based on elementary approach by solving the corresponding quadratic equations. Recently, Lee and co-authors<sup>4</sup> studied the following matrix equation

$$X^p = A + M^T(X\sharp B)M.$$

Similar to the approach<sup>5</sup> of Lim and Palfia, they used the Thompson metric and Banach fixed point theorem to show that the equation has a unique positive definite solution. Recently, Zhai and Jin<sup>6</sup> generalized the last equation for  $m$  nonsingular matrices. More precisely, they studied two non-linear matrix equations as follows

\*Corresponding author.

Email: [nguyenduyainhan@husc.edu.vn](mailto:nguyenduyainhan@husc.edu.vn)

$$X^p = A + \sum_{i=1}^m M_i^T (X \sharp B) M_i$$

and

$$X^p = A + \sum_{i=1}^j M_i^T (X \sharp B) M_i + \sum_{i=j+1}^m M_i^T (X^{-1} \sharp B) M_i,$$

where  $p, m, j$  are positive integers such that  $1 \leq j \leq m$ ,  $A, B$  are positive definite matrices and  $M_1, M_2, \dots, M_m$  are nonsingular real matrices.

Recently, Dinh and co-authors studied a more general case of these two equations. They considered similar matrix equations for the weighted matrix geometric mean

$$A \sharp_t B = A^{1/2} \left( A^{-1/2} B A^{-1/2} \right)^t A^{1/2}.$$

Namely, they studied the following matrix equations

$$X^p = A + \sum_{i=1}^m M_i^T (X \sharp_t B) M_i,$$

and

$$X^p = A + \sum_{i=1}^j M_i^T (X \sharp_t B) M_i + \sum_{i=j+1}^m M_i^T (X^{-1} \sharp_t B) M_i,$$

where  $p, m$  are positive integers,  $A, B$  are  $n \times n$  positive definite matrices and  $M_1, M_2, \dots, M_m$  are  $n \times n$  nonsingular real matrices. At the end of the paper, they not only mentioned that the weighted geometric mean  $A \sharp_t B$  is a matrix generalization of  $a^{1-t} b^t$  for two non-negative numbers  $a$  and  $b$  but also noticed that there is another symmetric generalization such as  $\left( A^{\frac{1-t}{2t}} B A^{\frac{1-t}{2t}} \right)^t$  which appears in the definition of the sandwiched quasi-relative entropy<sup>7</sup>  $Tr \left( A^{\frac{1-t}{2t}} B A^{\frac{1-t}{2t}} \right)^t$ .

In this note, we give a detail proof of next theorem:

**Theorem.** *Let  $A, B \in \mathcal{P}_n$ ,  $m$  be positive integers greater than 2, and  $p \geq 1$ . Then, for nonsingular matrices  $M_1, M_2, \dots, M_m$  in  $\mathbb{M}_n$ , the following matrix equation*

$$X^p = A + \sum_{i=1}^m M_i^T \left( B^{\frac{1-t}{2t}} X B^{\frac{1-t}{2t}} \right)^t M_i$$

has a unique positive definite solution  $X^*$  in  $\mathcal{P}_n$ .

We also study the multi-step stationary iterative method for this equation and prove the corresponding convergence.

## 2. MAIN RESULTS

**Definition 1.** (<sup>8</sup> [Definition 2.1.1]) An operator  $T : \mathcal{P}_n \rightarrow \mathcal{P}_n$  is said to be increasing if  $0 < x \leq y$  implies  $Tx \leq Ty$ .

The following lemma is crucial for us to prove the main results in this paper.

**Lemma 2.** (<sup>8</sup> [Theorem 2.1.6]) *Let  $T : \mathcal{P}_n \rightarrow \mathcal{P}_n$  be an increasing operator, and suppose that there exists  $r \in (0, 1)$  for which*

$$T(sx) \geq s^r T(x), \quad x \in \mathcal{P}_n, \quad s \in (0, 1).$$

Then  $T$  has a unique fixed point  $x^* \in \mathcal{P}_n$ .

**Theorem 3.** *Let  $A, B \in \mathcal{P}_n$ ,  $m$  be positive integers greater than 2, and  $p \geq 1$ . Then, for nonsingular matrices  $M_1, M_2, \dots, M_m$  in  $\mathbb{M}_n$ , the following matrix equation*

$$X^p = A + \sum_{i=1}^m M_i^T \left( B^{\frac{1-t}{2t}} X B^{\frac{1-t}{2t}} \right)^t M_i \quad (2)$$

has a unique positive definite solution  $X^*$  in  $\mathcal{P}_n$ .

*Proof.* Let consider the function

$$T(X) = \left( A + \sum_{i=1}^m M_i^T \left( B^{\frac{1-t}{2t}} X B^{\frac{1-t}{2t}} \right)^t M_i \right)^{\frac{1}{p}}.$$

We show that  $T(X)$  satisfies the conditions of Lemma 2, so it has a unique fixed point  $X^*$  in  $\mathcal{P}_n$ . That leads to the fact that Equation (2) has a unique positive definite solution  $X^*$  in  $\mathcal{P}_n$ .

Let  $0 < X_1 \leq X_2$  and  $0 < t < 1$ , we have  $\left( B^{\frac{1-t}{2t}} X_1 B^{\frac{1-t}{2t}} \right)^t \leq \left( B^{\frac{1-t}{2t}} X_2 B^{\frac{1-t}{2t}} \right)^t$ . Consequently,

$$M_i^T \left( B^{\frac{1-t}{2t}} X_1 B^{\frac{1-t}{2t}} \right)^t M_i \leq M_i^T \left( B^{\frac{1-t}{2t}} X_2 B^{\frac{1-t}{2t}} \right)^t M_i, \quad i = 1, 2, \dots, m.$$

Therefore,

$$A + \sum_{i=1}^m M_i^T \left( B^{\frac{1-t}{2t}} X_1 B^{\frac{1-t}{2t}} \right)^t M_i \leq A + \sum_{i=1}^m M_i^T \left( B^{\frac{1-t}{2t}} X_2 B^{\frac{1-t}{2t}} \right)^t M_i.$$

Since  $p \geq 1$ , the function  $x^{\frac{1}{p}}$  is a monotone operator on  $(0, +\infty)$ . We have

$$T(X_1) = \left( A + \sum_{i=1}^m M_i^T \left( B^{\frac{1-t}{2t}} X_1 B^{\frac{1-t}{2t}} \right)^t M_i \right)^{\frac{1}{p}} \leq \left( A + \sum_{i=1}^m M_i^T \left( B^{\frac{1-t}{2t}} X_2 B^{\frac{1-t}{2t}} \right)^t M_i \right)^{\frac{1}{p}} = T(X_2),$$

so the function  $T(X)$  is increasing.

Let  $X \in \mathcal{P}_n$ . For  $t \in (0, 1)$  and  $p \geq 1$ , there exists a constant  $r \in (0, 1)$  such that  $r \geq \frac{t}{p}$ . It is obvious that

$$\left( B^{\frac{1-t}{2t}} (sX) B^{\frac{1-t}{2t}} \right)^t = s^t \left( B^{\frac{1-t}{2t}} X B^{\frac{1-t}{2t}} \right)^t,$$

for any  $s \in (0, 1)$ .

Since  $rp \geq t$ , we have  $s^{rp} \leq s^t < 1$  for all  $s \in (0, 1)$ . Therefore,

$$A + s^t \sum_{i=1}^m M_i^T \left( B^{\frac{1-t}{2t}} X B^{\frac{1-t}{2t}} \right)^t M_i \geq s^{rp} \left( A + \sum_{i=1}^m M_i^T \left( B^{\frac{1-t}{2t}} X B^{\frac{1-t}{2t}} \right)^t M_i \right).$$

By the monotonicity of the function  $x^{\frac{1}{p}}$ , we have

$$T(sX) = \left( A + s^t \sum_{i=1}^m M_i^T \left( B^{\frac{1-t}{2t}} X B^{\frac{1-t}{2t}} \right)^t M_i \right)^{\frac{1}{p}} \geq \left( s^{rp} \left( A + \sum_{i=1}^m M_i^T \left( B^{\frac{1-t}{2t}} X B^{\frac{1-t}{2t}} \right)^t M_i \right) \right)^{\frac{1}{p}} = s^r \left( A + \sum_{i=1}^m M_i^T \left( B^{\frac{1-t}{2t}} X B^{\frac{1-t}{2t}} \right)^t M_i \right)^{\frac{1}{p}} = s^r T(X).$$

Thus,  $T(X)$  satisfies all conditions of Lemma 2. In other words, Equation (2) has a unique positive solution  $X^* \in \mathcal{P}_n$ .  $\square$

Now, let  $X_1, X_2, \dots, X_m$  be initial matrices in  $\mathcal{P}_n$  and consider the multi-step stationary iterative method for the equation (2) as following

$$X_{lm+j} = \left( A + \sum_{i=1}^m M_i^T \left( B^{\frac{1-t}{2t}} X_{(l-1)m+j} B^{\frac{1-t}{2t}} \right)^t M_i \right)^{\frac{1}{p}} \tag{3}$$

for  $l = 1, 2, 3, \dots$  and  $j = 1, 2, \dots, m$ .

In the following theorem, we show that the matrix sequence  $\{X_k\}$  generated by (3) converges to  $X^*$ .

**Theorem 4.** For any  $X_1, X_2, \dots, X_m \in \mathcal{P}_n$ , the sequence of matrices  $\{X_k\}$  generated by (3) converges to the unique positive definite solution  $X^*$  of the equation (2).

*Proof.* For matrices  $X_1, X_2, \dots, X_m$  and  $X^*$ , there exists  $a \in (0, 1)$  such that

$$aX^* \leq X_j \leq a^{-1}X^*, \quad j = 1, 2, \dots, m. \tag{4}$$

We show that for any  $b \in \mathbb{N}$  we have

$$a^{rb} X^* \leq X_k \leq a^{-rb}, \quad k = bm+j \quad (j = 1, 2, \dots, m) \tag{5}$$

for some  $r \in (0, 1)$  and  $r \geq \frac{t}{p}$ . Then, according

to the fact that  $\lim_{b \rightarrow \infty} a^{rb} = \lim_{b \rightarrow \infty} a^{-rb} = 1$  and the Squeeze theorem in the normal cone  $\mathcal{P}_n$ , it implies that  $\{X_k\}$  converges to  $X^*$ .

Now, we prove (5) by using the method of mathematical induction. For  $b = 0$ , the inequality (5) reduces to the case of (4). Assume that (5) is true for  $b = q - 1$  for some positive interger  $q$ , it means

$$a^{r^{q-1}} X^* \leq X_{(q-1)m+j} \leq a^{-r^{q-1}} X^* \tag{6}$$

for  $k = (q - 1)m + j$  and  $j = 1, 2, \dots, m$ .

Since  $X_{qm+j} = T(X_{(q-1)m+j})$  and  $T(X)$  is increasing, it implies from (6) that

$$T(a^{r^{q-1}} X^*) \leq T(X_{(q-1)m+j}) = X_{qm+j} \leq T(a^{-r^{q-1}} X^*).$$

Moreover,  $T(sX) \geq s^r T(X)$  in the case  $s \in (0, 1)$  and  $T(sX) \leq s^r T(X)$  in the case  $s > 1$ . Therefore,

$$T(a^{r^{q-1}} X^*) \geq \left( a^{r^{q-1}} \right)^r T(X^*) = a^{r^q} T(X^*) = a^{r^q} X^*$$



and

$$T\left(a^{-r^{q-1}}X^*\right) \leq a^{-r^q}T(X^*) = a^{-r^q}X^*.$$

So, we have

$$a^{r^q}X^* \leq X_{qm+j} \leq a^{-r^q}X^*.$$

Thus, (5) is true, and  $\{X_k\}$  converges to  $X^*$ .  $\square$

**REFERENCES**

1. W. Pusz, S.L. Woronowicz. Functional calculus for sesquilinear forms and the purification map, *Reports on Mathematical Physics*, **1975**, 8(2), 159-170.
2. Y. Lim. Inverse mean problem of geometric and contraharmonic means, *Linear Algebra Appl*, **2005**, 408, 221-229.
3. C. Jung, H.M. Kim, Y. Lim. On the solution of the nonlinear matrix equation  $X^n = f(X)$ , *Linear Algebra Appl*, **2009**, 430, 2042-2052.
4. H. Lee, H.M. Kim, J. Meng. On the nonlinear

matrix equation  $X^p = A + M^T(X \# B)M$ , *Journal of Computational Analysis and Applications*, **2020**, 373, 112380.

5. Y. Lim, M. Palfia. Matrix power means and the Karcher mean, *Journal of Functional Analysis*, **2012**, 262, 1498-1514.
6. C. Zhai, Z. Jin. Solvability for two forms of nonlinear matrix equations, *Bulletin of the Iranian Mathematical Society*, **2020**, <https://doi.org/10.1007/s41980-020-00431-4>.
7. M. Wilde, A. Winter, D. Yang. Strong converse for the classical capacity of entanglement-breaking and Hadamard channels via a sandwiched Renyi relative entropy, *Communications in Mathematical Physics*, **2014**, 331, 593-622.
8. D. Guo, V. Lakshmikantham. *Nonlinear Problems in Abstract Cones*, Academic Press, New York, 1988.



# Xác định sự xuất hiện vết nứt bằng phương pháp biến đổi Wavelet

Hoàng Công Vũ\*, Nguyễn Thị Thảo Nguyên

Khoa Kỹ thuật và Công nghệ, Trường Đại học Quy Nhơn, Việt Nam

Ngày nhận bài: 28/12/2020; Ngày nhận đăng: 09/04/2021

## TÓM TẮT

Ở bài báo này, độ nhạy của chuyển vị tấm có vết nứt sau khi dùng Phương pháp Phần tử hữu hạn mở rộng (eXtended Finite Element Method - XFEM) và biến đổi Wavelet được phân tích. Sự ảnh hưởng của chiều dài vết nứt và vị trí vết nứt được nghiên cứu. Các giá trị chuyển vị thu được từ bài toán tĩnh được tính toán bằng XFEM và phương pháp Newmark dựa trên mô hình phần tử đẳng tham số tứ giác 4 nút. Các giá trị chuyển vị dùng cho biến đổi Wavelet được nội suy trên cơ sở các hàm dạng, tọa độ và giá trị chuyển vị tại các nút của phần tử tấm. Kết quả khảo sát cho thấy chuyển vị của tấm có vết nứt sau khi biến đổi Wavelet tỏ ra rất nhạy đối với chiều dài và vị trí vết nứt.

**Từ khóa:** *Extended Finite Element Method (XFEM), tấm có vết nứt, chuyển vị, Wavelet.*

\*Tác giả liên hệ chính.

Email: hcvu@ftt.edu.vn

# Identification of cracks in structure by Wavelet transform method

Hoang Cong Vu\*, Nguyen Thi Thao Nguyen

*Faculty of Engineering and Technology, Quy Nhon University, VietNam*

*Received: 28/12/2020; Accepted: 09/04/2021*

## ABSTRACT

In this paper, sensitivity for the transverse displacements of the plate with a crack is analyzed using the Extended Finite Element Method (XFEM) and the Wavelet transform. The effects of the crack length and location are investigated. The transverse displacements obtained from the static analysis are studied by using the XFEM and the Newmark method based on an 4-node quadrilateral isoparametric element. The transverse displacements for transformation are interpolated by the shape functions, the coordinates, and the transverse displacements of the nodes of every element. The examined results show that the transformed transverse displacements are very sensitive to the crack length and location.

**Keywords:** *Extended Finite Element Method (XFEM), cracked plates, transverse displacements, Wavelet.*

## 1. INTRODUCTION

Technical diagnostic is an area that attracts many researchers around the world as well as in Viet Nam. Technical diagnostic has a particularly important role to technical objects. Especially, the discovery and assessment of defects and impairments in the structure have been receiving much interest from many authors to research. These impairments have a very large effect on construction capacity and longevity.

There have been many studies of analytical, numerical and experimental methods. Accordingly, the use of numerical methods is very effective in solving the cracked problems. And the Finite Element Method (FEM), has become a tool in use since an early age. However, in some cases FEM has become complicated, such as simulating the movement of non-continuous domains which leads to redivision of the element mesh. The Extended Finite Element Method (XFEM) offers us a new way

to model the crack independence of the element mesh; therefore, there is no need to redivide the element grid. Recently, some authors have used XFEM and Wavelet transforms to study the cracked structures. Bachene et al<sup>1</sup> combined the 9-node isonality element with XFEM to analyze the plate's vibration according to the Mindlin plate theory. Natarajan et al,<sup>2</sup> analyzed natural frequencies of cracked functionally graded material plates by the extended finite element method. Douka et al<sup>3</sup> identified the crack location and depth of the rectangular plates by analyzing Wavelet. Sun. et al<sup>4</sup> analyzed the sensitivity of the transverse displacements of the cracked plate by Wavelet transform.

The paper uses the Wavelet tool to identify cracks in structure. The transverse displacements obtained from the static analysis are studied by using the XFEM and the Newmark method. The transition displacements values found in the paper will be verified using ANSYS software and

---

\*Corresponding author:

Email: [hcvu@ftt.edu.vn](mailto:hcvu@ftt.edu.vn)

previous published studies to test the accuracy and effectiveness of the proposed method.

**2. THEORETICAL FORMULATION**

**2.1. XFEM Model**

This paper uses the 4-node quadrilateral isoparametric element. The plate element has three degrees of freedom in each node, which are three independent displacements: transverse displacements  $w$  and rotating angles  $\beta_x, \beta_y$ .<sup>5</sup>

The elements of independent displacement quantities are interpolated according to the corresponding node displacements:

$$w = \sum_{i=1}^4 N_i w_i, \beta_x = \sum_{i=1}^4 N_i \beta_{xi}, \beta_y = \sum_{i=1}^4 N_i \beta_{yi} \quad (1)$$

where:  $w_i, \beta_{xi}, \beta_{yi}$  corresponds to the values of the function  $w$  and  $\beta_x, \beta_y$  at node  $i$ , or the degrees of freedom of node  $i$ ;  $N_i$  are the shape functions according to the following natural coordinates:<sup>5</sup>

$$N_1 = -\frac{1}{4}(1-r)(1-s), N_2 = \frac{1}{4}(1+r)(1-s),$$

$$N_3 = \frac{1}{4}(1+r)(1+s), N_4 = \frac{1}{4}(1-r)(1+s) \quad (2)$$

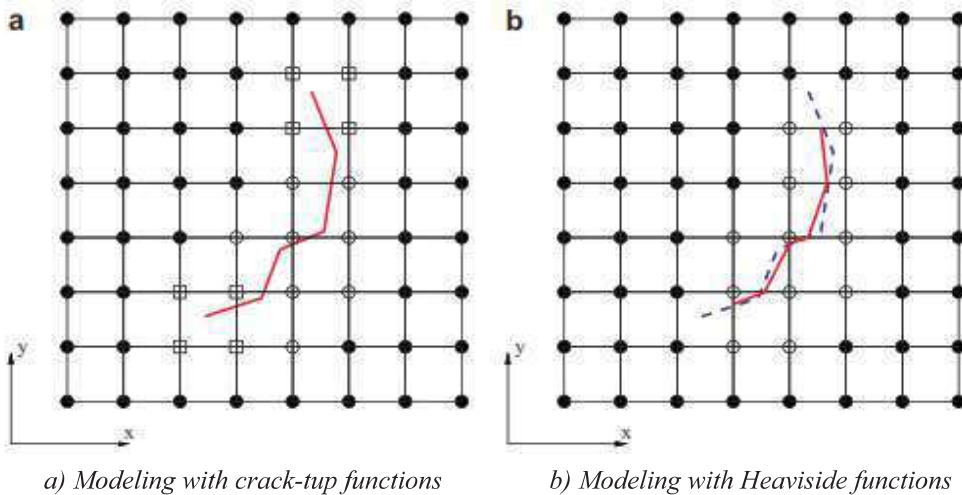
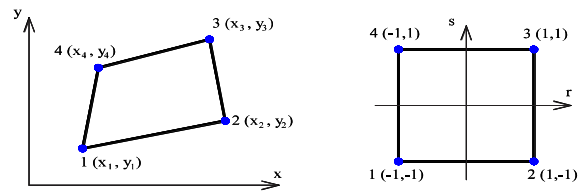


**Figure 2.** Crack modeling using XFEM approach

Examine a point  $x$  in the element domain, the displacement approximation at point  $x$  is calculated as follows:<sup>6</sup>

$$\mathbf{u}^h(\mathbf{x}) = \sum_{i \in N^{fem}} N_i(\mathbf{x}) \mathbf{u}_i + \sum_{j \in N^{enr}} H(\mathbf{x}) N_j(\mathbf{x}) \mathbf{a}_j + \sum_{k \in N^{enr}} N_k(\mathbf{x}) \sum_{\alpha=1}^4 \mathbf{B}_{\alpha k}(\mathbf{x}) \mathbf{b}_{\alpha k} \quad (4)$$



a) Physical co-ordinate system  
b) Natural co-ordinate system

**Figure 1.** Isoparametric element in the form of a 4-node quadrilateral

The displacement vector of the node  $\mathbf{u}_e$  is made up of 12 components:<sup>6</sup>

$$\mathbf{u}_e^T = \{w_1 \beta_{x1} \beta_{y1} \dots w_4 \beta_{x4} \beta_{y4}\}^T \quad (3)$$

The advantage of using enrichment functions in XFEM is that the crack is independent of the element mesh compared to FEM, which means that the element mesh at the crack location must not be redistributed like FEM. For crack modeling, two types of enrichment functions are used: the Heaviside functions and crack-tip functions (Fig. 2).

where:  $\mathbf{u}^h(\mathbf{x})$  is displacement approximation at point  $\mathbf{x}$

$\mathbf{u}_i$  is the vector of degrees of freedom associated with node  $i$

$\mathbf{a}_j$  is the vector of degrees of freedom of the node added by the Heaviside function

$\mathbf{b}_{\alpha k}$  is the vector of degrees of freedom of the node complemented by the asymptote function at the crack-tip

$\mathbf{N}^{fem}, \mathbf{N}^{enr}, \mathbf{N}^{asy}$  is the set of non-expanding nodes, nodes bisected by cracks and nodes containing crack-tip

$N_i(\mathbf{x}), N_j(\mathbf{x}), N_k(\mathbf{x})$  and are the corresponding shape functions of the standard element, edge complements, and crack-tip complement element

$H(\mathbf{x})$  is additional function or Heaviside discontinuous function

$\mathbf{B}_{\alpha k}(\mathbf{x})$  is extension function at crack-tip

Extension function at crack-tip  $\mathbf{B}_{\alpha k}$  known as branch functions:

$$\mathbf{B}_{\alpha k} = [B_1, B_2, B_3, B_4] \quad (5)$$

where:  $B_1(r, \theta) = \sqrt{r} \sin\left(\frac{\theta}{2}\right)$   $B_2(r, \theta) = \sqrt{r} \cos\left(\frac{\theta}{2}\right)$

$B_3(r, \theta) = \sqrt{r} \sin \theta \sin\left(\frac{\theta}{2}\right)$   $B_4(r, \theta) = \sqrt{r} \sin \theta \cos\left(\frac{\theta}{2}\right)$

where  $(r, \theta)$  are polar coordinates determined at crack-tip.

### 2.2. Static equilibrium equation of cracked plate<sup>6</sup>

The system of equations for analysis of static behavior of cracked plate by XFEM:

$$\mathbf{K} \cdot \mathbf{u}^h = \mathbf{f} \quad (6)$$

where:  $\mathbf{K}$  is the overall stiffness matrix

$\mathbf{u}^h$  is the vector of nodal freedom

$\mathbf{f}$  is the external load vector. The overall stiffness matrix and the external load vector assembled from element stiffness matrix  $\mathbf{K}^e$  and element vector  $\mathbf{f}^e$ , where:

$$\mathbf{K}_{ij}^e = \begin{bmatrix} \mathbf{K}_{ij}^{uu} & \mathbf{K}_{ij}^{ua} & \mathbf{K}_{ij}^{ub} \\ \mathbf{K}_{ij}^{au} & \mathbf{K}_{ij}^{aa} & \mathbf{K}_{ij}^{ab} \\ \mathbf{K}_{ij}^{bu} & \mathbf{K}_{ij}^{ba} & \mathbf{K}_{ij}^{bb} \end{bmatrix} \quad (7)$$

$$\mathbf{f}_i^e = \left\{ \mathbf{f}_i^u \quad \mathbf{f}_i^a \quad \mathbf{f}_i^{b1} \quad \mathbf{f}_i^{b2} \quad \mathbf{f}_i^{b3} \quad \mathbf{f}_i^{b4} \right\}^T \quad (8)$$

$$\mathbf{u}^h = \left\{ \mathbf{u} \quad \mathbf{a} \quad \mathbf{b}_1 \quad \mathbf{b}_2 \quad \mathbf{b}_3 \quad \mathbf{b}_4 \right\}^T \quad (9)$$

Where

$$\mathbf{K}_{ij}^{rs} = \int_{\Omega^e} (\mathbf{B}_i^r)^T \mathbf{D}_b \mathbf{B}_j^s d\Omega + \int_{\Omega^e} (\mathbf{S}_i^r)^T \mathbf{D}_s \mathbf{S}_j^s d\Omega \quad (10)$$

$(r, s = \mathbf{u}, \mathbf{a}, \mathbf{b})$

Include the standard element ( $\mathbf{uu}$ ), Heaviside extension element ( $\mathbf{aa}$ ), extension element at crack-tip ( $\mathbf{bb}$ ),  $\mathbf{D}_b$  is the matrix of elastic coefficients due to bending,  $\mathbf{D}_s$  is the matrix of elastic coefficients due to shear,  $\mathbf{B}$  is bending deformation matrix, and  $\mathbf{S}$  is shear deformation matrix.

### 3. CALCULATING CRACKED PLATE DISPLACEMENT USING XFEM

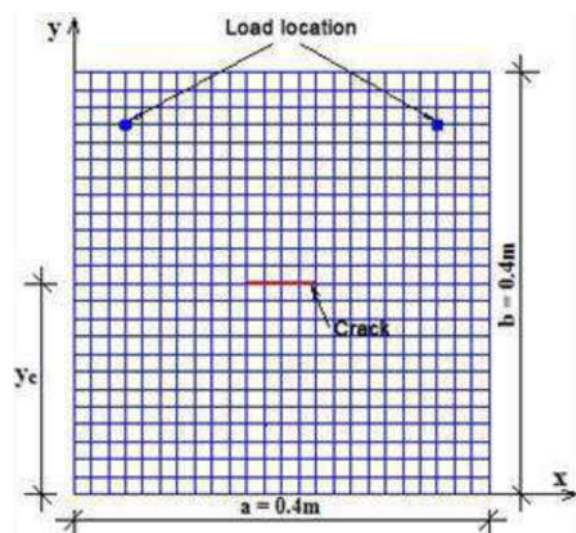


Figure 3. Static plate problem model

**Problem 1:** Examine a bending thin plate with a crack (Fig. 3), a single with geometric parameters, material properties and load: the plate length  $a = 0.4 \text{ m}$ ; the plate width  $b = 0.4 \text{ m}$ , the plate thickness  $h = 0.0005 \text{ m}$ , the crack is in symmetry through the axis  $x = 0.2 \text{ m}$ , and parallel to the axis  $y$ , the crack location  $y_c = 0.2 \text{ m}$ , crack length changes  $c = 0.04, 0.06, 0.08, 0.10, 0.12 \text{ m}$ ; Elastic modulus  $E = 71 \times 10^9 \text{ N/m}^2$ , Poisson coefficient  $\mu = 0.3$ ; concentrated load  $P = 2.5 \text{ N}$ , located at the coordinates  $(x = 0.05 \text{ m}, y = 0.35 \text{ m})$  and  $(x = 0.35 \text{ m}, y = 0.35 \text{ m})$ .

Problem modeling with mesh  $25 \times 25$ . The maximum displacement calculation results for the plate are written in the Matlab equation with the displacement location at node 388. To test

the reliability, the results is compared with the result of the solution using the ANSYS program, through the use of the SHELL281 element to simulate a cracked plate.

**Table 1.** Maximum displacement ( $w_{\max} (\times 10^{-3} m)$ ) of cracked plate

Crack length $c$ (m)	0	0.04	0.06	0.08	0.10	0.12
$w_{\max}$ -FEM (ANSYS) ( $\times 10^{-3} m$ )	1.4398	1.4655	1.4750	1.4884	1.5043	1.5300
$w_{\max}$ -FEM <sup>7</sup> ( $\times 10^{-3} m$ )	-	1.427	-	1.426	-	1.427
$w_{\max}$ -XFEM (MATLAB) ( $\times 10^{-3} m$ )	1.4388	1.4395	1.4398	1.4534	1.4691	1.4806
Percentage of error with ANSYS	0.0695	1.7741	2.3864	2.3515	2.3400	3.2288
Percentage of error with FEM <sup>7</sup>	-	0.8760	-	1.9215	-	3.7561

From the results shown in Table 1, when the crack length increases by  $0.04, 0.06, 0.08, 0.10, 0.12 m$  the maximum displacement of the plate also increases. This corresponds to the physical nature of the problem model (like the crack length increases, plate stiffness decreases causing displacement to increases)

XFEM and FEM<sup>7</sup> for Problem 1 with the crack, length changes, it can be seen that the error result also depends on the crack length. The longer the fracture is, the greater the error. The maximum error is 3.7561% when crack length  $c = 0.12 m$ .

Comparison to the results between XFEM(MATLAB) and FEM(ANSYS) for Problem 1 with the crack length changes, it can be seen that the error result depends on the crack length. Specifically, the longer the crack is, the greater the error: the maximum error is 3.2288% when crack length  $c = 0.12 m$ .

The results of these calculations indicate that the program written in MATLAB for a cracked plate is completely reliable.

Comparison to the the results between

**Problem 2:** The same problem parameters as Problem 1. Crack length of the plate  $c = 0.04 m$ ; the crack location varies by  $y_c = 0.05, 0.10, 0.20, 0.30, 0.35 m$ .

The maximum displacement result (node position 338), is shown in Table 2.

**Table 2.** Maximum displacement ( $w_{\max} (\times 10^{-3} m)$ ) of cracked plate

Crack location $y_c$ (m)	0.05	0.10	0.20	0.30	0.35
$w_{\max}$ -ANSYS ( $\times 10^{-3} m$ )	1.4537	1.4532	1.4655	1.4445	1.4448
$w_{\max}$ -MATLAB ( $\times 10^{-3} m$ )	1.4388	1.4387	1.4395	1.4422	1.4404
Error (%)	1.0250	0.9978	1.7741	0.1592	0.3045

From the results shown in Table 2, the error between Matlab and Ansys programs was relatively low (1.7741% at the largest). This result shows the high reliability of Matlab program.

**4. CRACKED PLATE DISPLACEMENT THROUGH WAVELET TRANSFORM**

The following problems are taken from the figures in Section 3 respectively, the set containing 961 displacement values of the plate

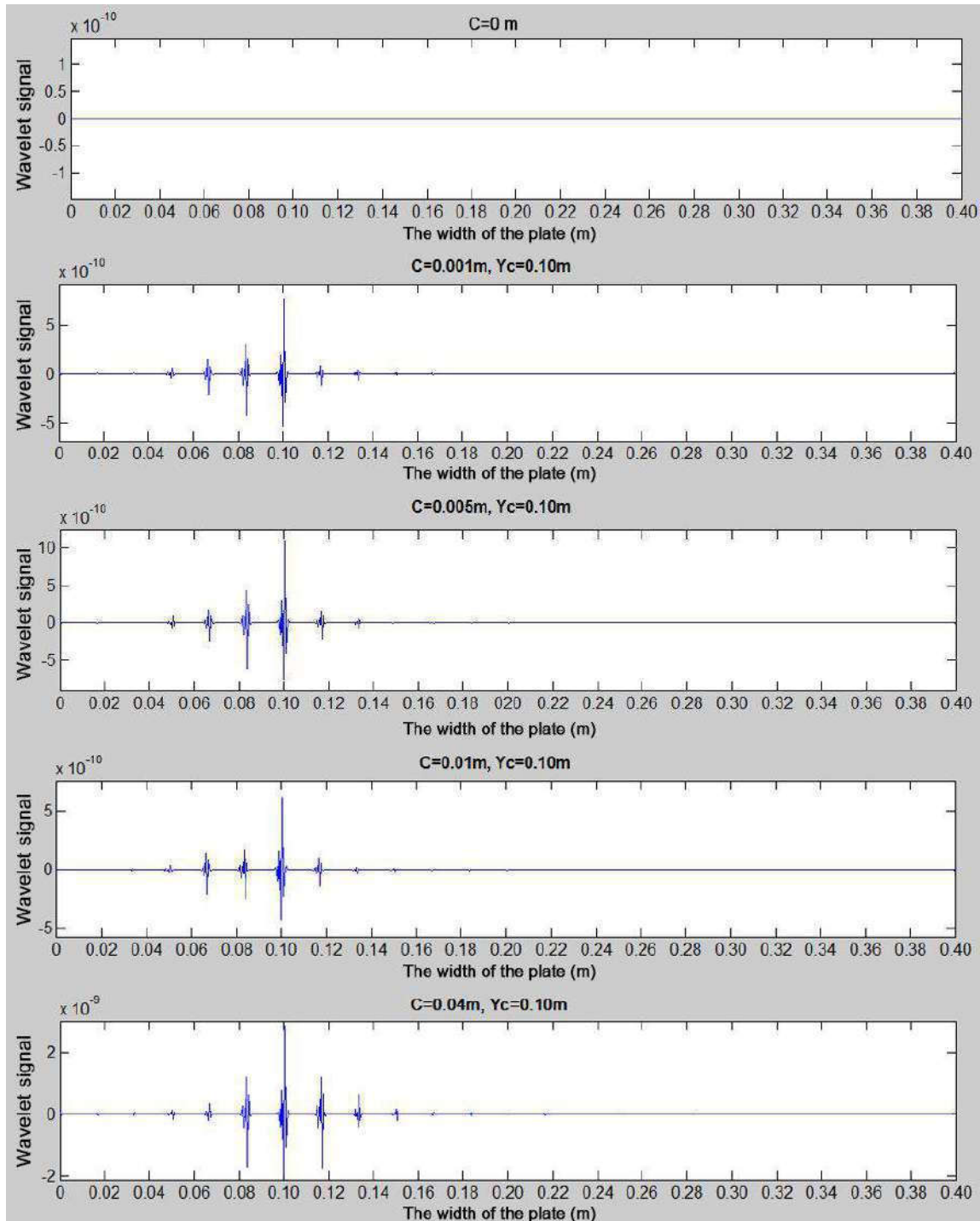
used to transform Wavelet along the axis  $y$ , at the location  $x = 0.2$ . The author uses Wavelet *sym4* in the symlets kinship to identify cracks in the structure.

*Analysis results*

During the process of continuous Wavelet transformations, it is possible to effectively observe the sensitivity of the signal at the crack

location of the plate.

**Problem 1:** A four-segments simply support bending plate and the concentrated load  $P = 2.5 N$ , located at the coordinates  $(x = 0.05 m, y = 0.35 m)$  and  $(x = 0.35 m, y = 0.35 m)$ ; crack location of the unchanged fissure ( $y_c = 0.10 m$ ), crack length changes ( $c = 0.001, 0.005, 0.01, 0.04, 0.06, 0.08, 0.10, 0.12 m$ ).





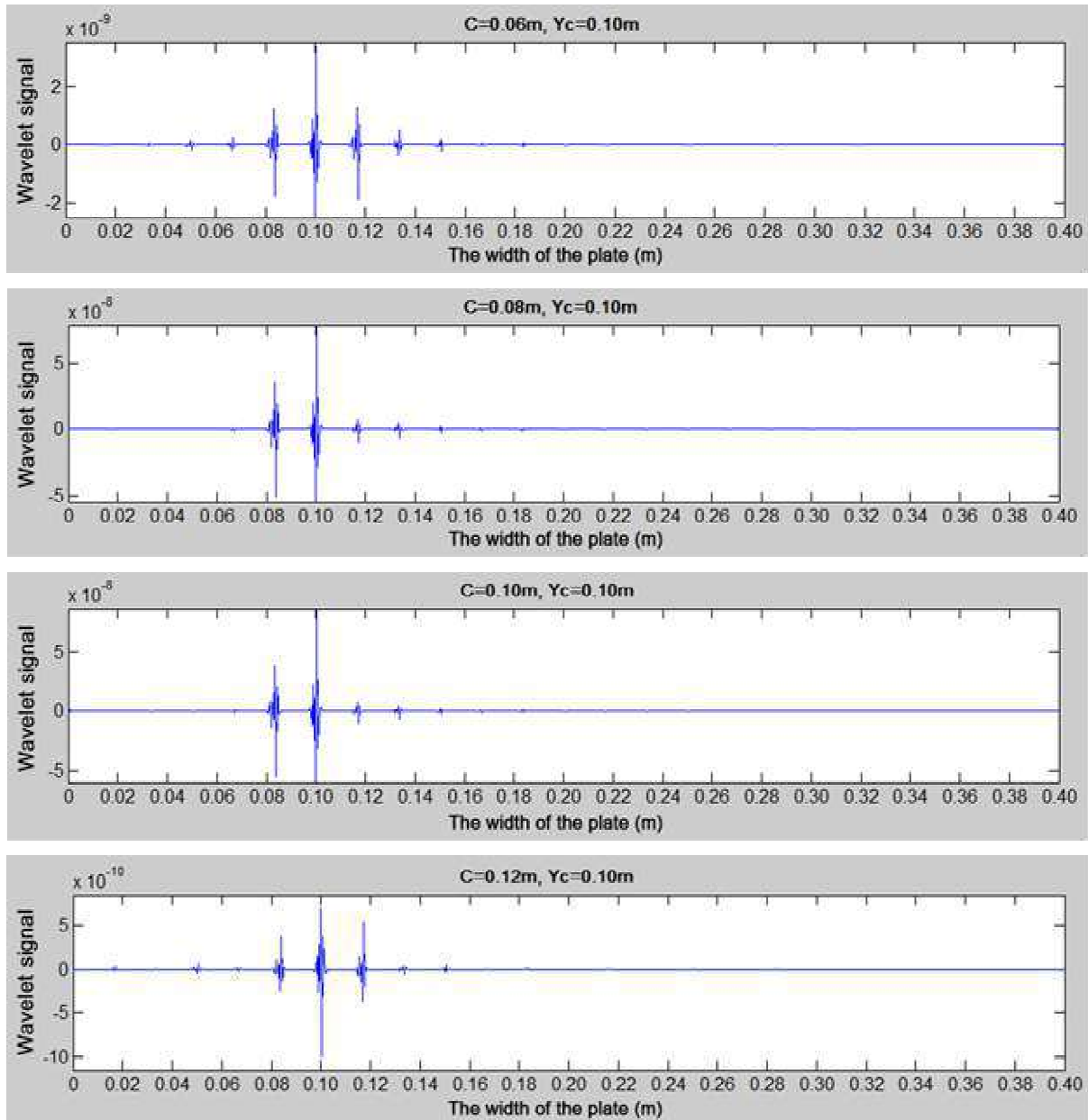


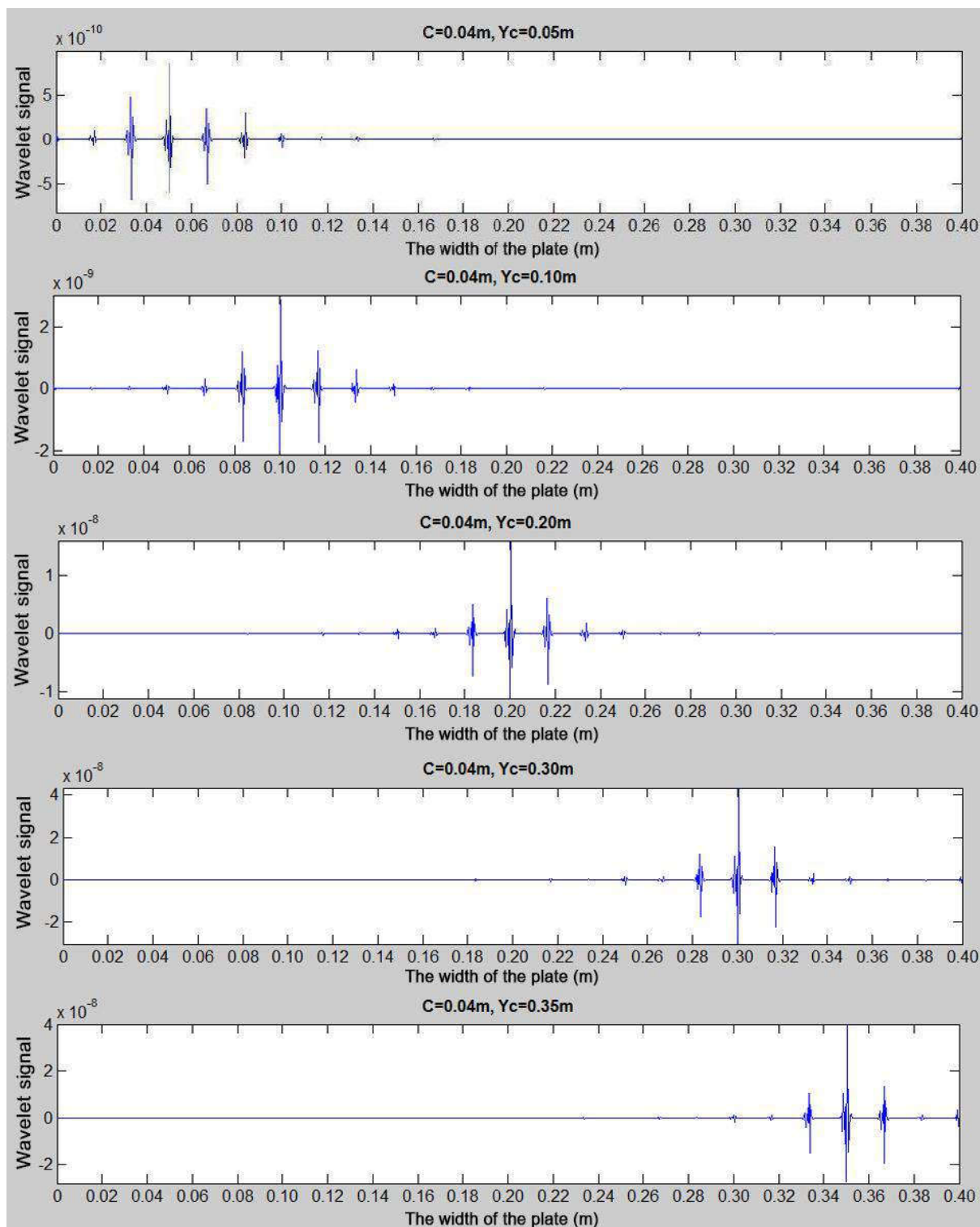
**Figure 4.** Graph of wavelet signals of static load plate displacement when crack length changes

**Problem 2:** A four-sided unbending plate and the load  $P = 2.5 \text{ N}$ , located at the coordinates  $(x = 0.05 \text{ m}, y = 0.35 \text{ m})$  và  $(x = 0.35 \text{ m}, y = 0.35 \text{ m})$ ;

**Case 1:** The crack length is constant ( $c = 0.04 \text{ m}$ ),

the crack location changes ( $y_c = 0.05, 0.10, 0.20, 0.30, 0.35 \text{ m}$ ).

**Case 2:** The crack length is constant ( $c = 0.005 \text{ m}$ ), the crack location changes ( $y_c = 0.033, 0.20, 0.367 \text{ m}$ ).



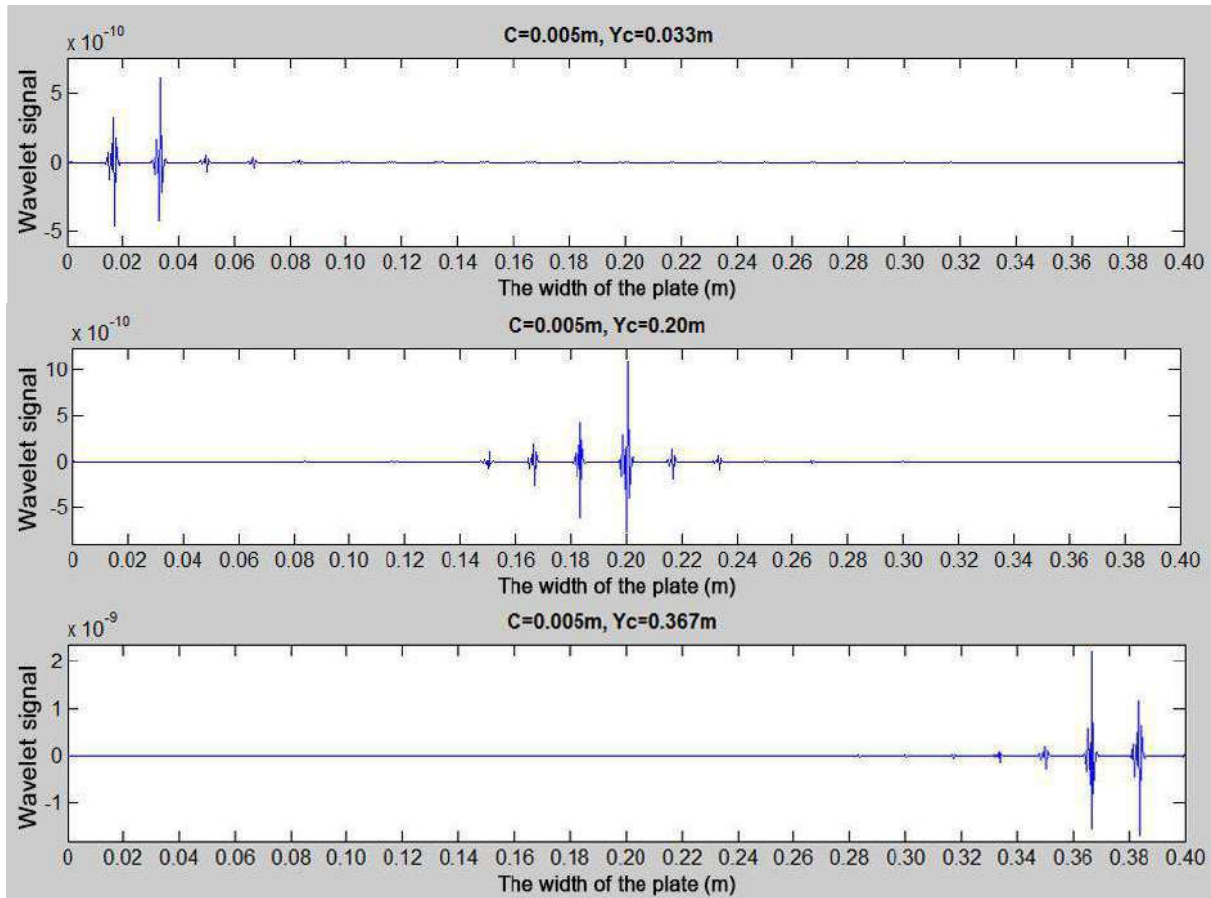


**Figure 5.** Graph of wavelet signals of static load plate displacement when crack position changes

The sudden signal change is shown clearly in different crack lengths and different crack locations (Fig. 5). In particular, as the crack length increases 0.001, 0.005, 0.01, 0.04, 0.06, 0.08, 0.10, 0.12 m the “leap” of the error signal increases:  $1.3 \times 10^{-9}$ ,  $1.7 \times 10^{-9}$ ,  $1.2 \times 10^{-9}$ ,  $5 \times 10^{-9}$ ,  $6 \times 10^{-9}$ ,  $130 \times 10^{-9}$ ,  $150 \times 10^{-9}$ ,  $170 \times 10^{-9}$  m and the error signal also increases at the crack locations: 0.05, 0.10, 0.20, 0.30, 0.35 m (the crack length  $c = 0.04$  m) and the crack locations: 0.033, 0.20, 0.367 m (the crack length  $c = 0.005$  m). When the crack is located at the load location the signal changes greater and more clearly. When the crack length is small ( $c = 0.05$  m) and far from the load location ( $y_c = 0.033$  m), the Wavelet signal graph shows exact crack location. But when the crack length is very small ( $c=0.001$  m), the error signal at the crack location is still very clear (Fig. 4)

**5. CONCLUSIONS**

The paper showed XFEM's ability to efficiently

apply and Wavelet transforms to identify cracks in the cracked plate. The analysis results show that the displacement computing program by XFEM is very reliable. The examined results show that the transformed transverse displacements are very sensitive to the crack length and location. This opens up the possibility of developing the problem of any cracked plate, developing cracks in the complex dynamic load-bearing plate that will be presented in later studies.

**REFERENCES**

1. M. Bachene et al. Vibration analysis of cracked plates using the extended finite element method, *Archive of Applied Mechanics*, **2009**, 79, 249–262.
2. S. Natarajan et al. Natural frequencies of cracked functionally graded material plates by the extended finite element method, *Composite Structures*, **2011**, 93, 3082–3092.

3. E. Douka et al. Crack identification in plates using wavelet analysis, *Journal of Sound and Vibration*, **2002**, 270, 279-295.
4. H. Y. Sun et al. *Sensitivity analysis for the transverse displacements of a cracked plate using the spatial wavelet approach*, ASME 2005 International Design Engineering Technical Conferences & Computers and Information In Engineering Conference, Long Beach, California USA, September 24-28, 2005.
5. S. S. Rao. *The finite element method in engineering*, Second Edition, Pergamon Press, 1989.
6. S. Mohammadi. *Extended finite element method*, School of Civil Engineering University of Tehran, Iran, 2008.
7. Nguyen Thi Hien Luong, Pham Ngoc Tien. *Sensitivity analysis of plate displacement with cracks by Wavelet transform method*, Proceedings of the 8<sup>th</sup> National Scientific Conference on Mechanics of Deformed Solids, Hanoi, 6-7/12/2007.

# Tối ưu hóa dựa trên thiết kế tổng hợp trung tâm (CCD) cho quá trình chuyển hóa axit béo tự do trong dầu chiết xuất từ bã cà phê thành diesel sinh học

Phan Thị Thanh Phương<sup>1</sup>, Võ Văn Tiến<sup>1</sup>, Nguyễn Việt Quang<sup>1</sup>,  
Lê Thị Thanh Ngân<sup>1</sup>, Đặng Nguyên Thoại<sup>1,2,\*</sup>

<sup>1</sup>Khoa Khoa học Tự nhiên, Trường Đại học Quy Nhơn, Việt Nam

<sup>2</sup>Trung tâm Hỗ trợ sinh viên và Quan hệ doanh nghiệp, Trường Đại học Quy Nhơn, Việt Nam

Ngày nhận bài: 26/03/2021; Ngày nhận đăng: 22/04/2021

## TÓM TẮT

Hiện nay, dầu chiết xuất từ bã cà phê (WCGO) đã chứng minh là nguồn nguyên liệu phù hợp để sản xuất diesel sinh học. Tuy nhiên, vì hàm lượng axit béo tự do (FFA) cao trong dầu được trích ly từ bã cà phê nên cần có quá trình tiền xử lý. Trong nghiên cứu này, phản ứng este hóa giữa FFA trong dầu được chiết xuất từ bã cà phê với methanol được thực hiện trong thiết bị phản ứng khuấy trộn, làm việc gián đoạn. Phương pháp bề mặt đáp ứng (RSM) được áp dụng để thiết lập các thí nghiệm, phân tích, đánh giá và tối ưu hóa kết quả thực nghiệm. Các điều kiện thực nghiệm bao gồm: tỷ lệ mol giữa methanol/WCGO (5 – 10 mol/mol), hàm lượng xúc tác H<sub>2</sub>SO<sub>4</sub>/WCGO (1 – 10% kl), nhiệt độ phản ứng (50 – 70 °C) và thời gian phản ứng (60 – 120 phút). Ảnh hưởng của các điều kiện thực nghiệm đã được đánh giá và kiểm tra nhờ phương pháp RSM. Mô hình hồi quy cho quá trình chuyển hóa FFA trong WCGO thành biodiesel đã được xác thực bởi hệ số tương quan cao ( $R^2 = 0,923$ ). Độ chuyển hóa FFA đạt được 90% (ứng với hàm lượng FFA cuối cùng đạt 0,7% kl) với tỷ lệ mol MeOH/WCGO là 8,18 mol/mol, hàm lượng xúc tác H<sub>2</sub>SO<sub>4</sub>/WCGO là 8,74% kl trong thời gian phản ứng 90 phút tại nhiệt độ 60 °C. Cuối cùng, một vài chỉ tiêu quan trọng của sản phẩm ester hóa được kiểm tra phù hợp cho các giai đoạn tiếp theo của quá trình sản xuất diesel sinh học.

**Từ khóa:** Diesel sinh học, bã cà phê, WCGO, este hóa, RSM.

\*Tác giả liên hệ chính.

Email: dangnguyenthoai@qnu.edu.vn

# Central composite design-based optimization for conversion of free fatty acids in oil extracted from coffee grounds into biodiesel

Phan Thi Thanh Phuong<sup>1</sup>, Vo Van Tien<sup>1</sup>, Nguyen Viet Quang<sup>1</sup>,  
Le Thi Thanh Ngan<sup>1</sup>, Dang Nguyen Thoai<sup>1,2,\*</sup>

<sup>1</sup>Faculty of Natural Sciences, Quy Nhon University, Vietnam

<sup>2</sup>Center for Student Support and Enterprise Relations, Quy Nhon University, Vietnam

Received: 26/03/2021; Accepted: 22/04/2021

## ABSTRACT

Extracted oil from waste coffee grounds (WCGO) has proven to be a suitable source to produce biodiesel. However, they need to be pretreated because of high free fatty acid (FFA) content in WCGO. In this study, the esterification reaction between FFA in extracted oil from coffee grounds with methanol was performed in a batch reactor. Response surface methodology (RSM) was applied to establish experiment, synthesize, evaluate, and optimize the experiment results. The factors included: MeOH/WCGO molar ratio (5 – 10 mol/mol), H<sub>2</sub>SO<sub>4</sub>/WCGO catalyst content (1 – 10 wt.%), temperature (50 – 70 °C) and reaction time (60 – 120 min). The effects of these factors were evaluated and tested as per RSM. The regression model of conversion of FFA in WCGO to biodiesel was established with a high correlation coefficient ( $R^2 = 0.923$ ). The FFA conversion of 90% (final FFA content of 0.70 wt%) was achieved with the MeOH/WCGO molar ratio of 8.18 mol/mol, H<sub>2</sub>SO<sub>4</sub>/WCGO catalyst content of 8.74 wt.% for 90 min at 60 °C. Finally, some important properties of the esterified oil were checked for the suitability for the next stage of biodiesel production.

**Keywords:** Biodiesel, Waste coffee ground, WCGO, esterification, RSM.

## 1. INTRODUCTION

In general, biodiesel is defined as fatty acid alkyl esters produced from alternative resources via esterification, transesterification or two-step reactions. Its properties are acceptable to be used directly or mixed with petroleum diesel.<sup>1</sup> At the present, the basic resources to produce biodiesel is cooking oils thanks to its low FFA content. Nevertheless, depending on edible vegetable oils is a major drawback to commercial target because of high price and food security.<sup>2</sup> Therefore, many non-edible oils including

waste cooking oil, Jatropha oil and waste coffee ground oils (WCGO) have been more and more attractive as renewable resources for biodiesel production with low cost.<sup>1,2</sup>

Vietnam is a country in the top two of the leading coffee producing countries in the world, only after Brazil. In 2019, approximately 2.6 million 60 kg bags of coffee was consumed in Vietnam.<sup>3</sup> By considering this huge amount, the re-use process of WCGO should be made. The WCGOs contains 11 – 20 wt.% of oil hang on its kind.<sup>4,5</sup> WCGO is convinced to become a

---

\*Corresponding author:

Email: dangnguyenthaoi@qnu.edu.vn

novel feedstock to create biodiesel. Nonetheless, inedible oils accommodate a high FFA (> 2 wt.%) to be easy to react with the alkaline catalysts to form soap via the saponification reaction. This process take to losing of catalyst and ester and grow the manufacture cost.<sup>1</sup> Therefore, WCGO needs to be treated by esterification reaction to remove FFA as much as possible before transesterification reaction to make biodiesel.

In this work, the esterification of WCGO in the existence of H<sub>2</sub>SO<sub>4</sub> as a homogeneous acid catalyst was performed to lessen the FFA content. The aims of this task were: (a) investigating the acid-catalyzed esterification reaction; (b) evaluating the influence of MeOH/WCGO molar ratio, H<sub>2</sub>SO<sub>4</sub>/WCGO catalyst content, temperature and reaction time on the FFA conversion in WCGO; (c) employing response surface methodology (RSM) to design, analyze, and optimize the experimental conditions; and (d) determining some properties of the esterified oil.

**2. MATERIALS AND METHODS**

**2.1. Materials**

Waste coffee grounds (WCGs) were collected from coffee shops in Quy Nhon City, Vietnam. Methanol (MeOH, purity > 99 wt.%) and sulfuric acid (H<sub>2</sub>SO<sub>4</sub>, purity > 98 wt.%) were purchased from Xilong Scientific Co., Ltd., China. Etanol (EtOH, purity > 99 wt.%) was obtained from Cemaco Vietnam Co., Ltd. – Ho Chi Minh city Branch, Vietnam.

**2.2. Extraction of WCGO**

First, the WCGs were dried in sunlight for 24 hours to remove its wetness. Second, the dried

WCGs were extracted by using ethanol. This mixture was mixed in 15 minutes and then it was disparted from the WCGs by filter.<sup>4</sup> Next, the WCGO was disparted from the solvent by utilizing a vacumn rotary evaporation. The WCGO was kept in the stove in 5 hours at 105 °C to separate any ethanol remaining in the extracted WCGO.

**2.3. Esterification procedure**

The esterification process was conducted in a 0.5-liter three-necked round-bottom flask attached to a thermometer, with magnetic stirring at stirring speed of 600 rpm, reflux by water at 20 °C to liquefy the MeOH vapour. The parameters for experiment were chosen and shown as in Table 1. First, the WCGO was preheated up to the temperature extended to the called value. Next, the mix of MeOH and H<sub>2</sub>SO<sub>4</sub> (98 wt.%) were added into flask. After finished reaction, the product was poured into the separating tube and settled in 90 min to discrete into two phases (oil phase and aqueous phase). Then, the aqueous phase was taken out of the oil phase, the oil phase was washed with hot water to unfasten the catalyst and the alcohol out of oil phase. This procedure was conducted at 70 °C, three times without swaying and three times with swaying. The washed oil phase was dried completely by the reheating at 110 °C in 120 minutes.

All experiments were done three times to approximate mistake. Experiments parameters were planned with different conditions including MeOH/WCGO molar ratio (5-10 mol/mol), catalyst content (1-10 wt% H<sub>2</sub>SO<sub>4</sub>/WCGO), reaction temperature (50-70 °C) and reaction time (60-120 minutes).

**Table 1.** Experimental parameters used in esterification of WCGO

Variables			Limit and coded level				
Variables	Symbol	Unit	-α	-1	0	+1	+α
MeOH/WCGO molar ratio	X <sub>1</sub>	mol/mol	5	6.25	7.5	8.75	10
H <sub>2</sub> SO <sub>4</sub> /WCGO catalyst content	X <sub>2</sub>	wt.%	1	3.25	5.5	7.75	10
Reaction temperature	X <sub>3</sub>	°C	50	55	60	65	70
Reaction time	X <sub>4</sub>	min	60	75	90	105	120

**2.4. FFA analysis and FFA conversion**

The initial FFA content of the WCGO and the final product were determined based on ASTM D664. First, the sample was accurately weighted about 1 – 10 g into a conical vessel. Then, 50 mL of ethanol was attached and vigorous swung to diffuse this sample. Phenolphthalein was attached about 3 – 5 drops as an indicator. The mix was titrated with 0.1N NaOH up to emerging a continuing pink. The FFA content and FFA conversion were caculated according to the following equations:

$$\%FFA = \frac{(V \times C \times 267.5) \times 100}{1000 \times m} \quad (1)$$

$$X = \frac{\%FFA_o - \%FFA}{\%FFA_o} * 100\% \quad (2)$$

Herein, V and C are volume (mL) and concentration (mol/L) of NaOH, m is the sample weight (g) and 267.5 is the average molecular weight of WCGO’s fatty acid (g/mol).<sup>6</sup>

**2.5. Experiment designs**

Response surface methodology (RSM) is one of modern statistical methods used to determine response behavior.<sup>7</sup> The central composite

design (CCD) was applied to discover the best conditions for the wanted FFA conversion. The CCD combines five levels (coded  $-\alpha$ ,  $-1$ ,  $0$ ,  $+1$ ,  $+\alpha$ , as in Table 1). The parameters, such as Fischer’s test (F-value), the probability (p-value), correlation coefficient (R), coefficient of determination ( $R^2$ ) were utilized to predict the show of the response of the esterification process. In addition, diagnostic plots, such as standardized residual and run number plot, expected normal value and residuals plot, studentized residuals and predicted values plot, predicted values and real values plot were also employed to estimate of the model. The second order polynomial regression model equation is generally indicated as in Eq. (3).

$$Y = \beta_o + \sum_{i=1}^4 \beta_i X_i + \sum_{i=1}^3 \sum_{j=i+1}^4 \beta_{ij} X_i X_j + \sum_{i=1}^4 \beta_{ii} X_i^2 \quad (3)$$

Herein, Y is the predicted response (FFA conversion);  $\beta_o$ ,  $\beta_i$ ,  $\beta_{ii}$ ,  $\beta_{ij}$  are the regression coefficients ( $\beta_o$  is the constant term,  $\beta_i$  is a linear term,  $\beta_{ii}$  is a quadratic term and  $\beta_{ij}$  is an interaction term);  $X_i$ ,  $X_j$  are coded independent factors.

**Table 2.** The coded independent factors, experimental results and predicted values

Run	Independent Variables				FFA conversion (%)			Run	Independent Variables				FFA conversion (%)		
	X <sub>1</sub>	X <sub>2</sub>	X <sub>3</sub>	X <sub>4</sub>	Expe- riment	Pre- dict	Resi- dual		X <sub>1</sub>	X <sub>2</sub>	X <sub>3</sub>	X <sub>4</sub>	Expe- riment	Pre- dict	Resi- dual
1	6.25	3.25	55	75	70.23	71.12	-0.89	16	8.75	7.75	65	105	94.98	94.17	0.81
2	8.75	3.25	55	75	66.89	68.39	-1.50	17	5	5.5	60	90	77.36	79.11	-1.75
3	6.25	7.75	55	75	88.45	86.47	1.98	18	10	5.5	60	90	85.83	82.21	3.62
4	8.75	7.75	55	75	82.69	85.15	-2.46	19	7.5	1	60	90	65.03	67.44	-2.41
5	6.25	3.25	65	75	80.32	79.52	0.80	20	7.5	10	60	90	98.06	93.79	4.27
6	8.75	3.25	65	75	79.45	76.65	2.80	21	7.5	5.5	50	90	76.55	74.87	1.68
7	6.25	7.75	65	75	83.79	85.12	-1.34	22	7.5	5.5	70	90	79.97	79.78	0.19
8	8.75	7.75	65	75	80.01	83.67	-3.66	23	7.5	5.5	60	60	86.51	85.31	1.20
9	6.25	3.25	55	105	74.23	72.36	1.87	24	7.5	5.5	60	120	97.71	97.05	0.66
10	8.75	3.25	55	105	78.17	76.92	1.25	25	7.5	5.5	60	90	79.66	78.77	0.89
11	6.25	7.75	55	105	88.80	91.68	-2.88	26	7.5	5.5	60	90	77.27	78.77	-1.50
12	8.75	7.75	55	105	95.07	97.66	-2.59	27	7.5	5.5	60	90	81.69	78.77	2.92
13	6.25	3.25	65	105	81.13	78.75	2.38	28	7.5	5.5	60	90	80.07	78.77	1.30
14	8.75	3.25	65	105	79.41	83.17	-3.76	29	7.5	5.5	60	90	75.54	78.77	-3.23
15	6.25	7.75	65	105	88.05	88.33	-0.28	30	7.5	5.5	60	90	78.38	78.77	-0.39



**Table 3.** ANOVA results for the adjusted regression model

Source/Term	Degree of freedom (DF)	Coefficient	Sum of squares (SS)	Mean squares (MS)	F-value	P-value*	Remarks
Model	14		1751.0	125.07	12.84	<0.0001	Significant
$\beta_0$		80.76				0.55	Insignificant
Linear	4						
$X_1$	1	-13.04				0.224	Insignificant
$X_2$	1	11.32				0.04827	Significant
$X_3$	1	3.807				0.249	Insignificant
$X_4$	1	-2.777				0.00543	Significant
Square	4						
$X_1^2$	1	0.303				0.439	Insignificant
$X_2^2$	1	0.09109				0.451	Insignificant
$X_3^2$	1	-0.01440				0.555	Insignificant
$X_4^2$	1	0.01379				0.000106	Significant
Interaction	6						
$X_1X_2$	1	0.126				0.657	Insignificant
$X_1X_3$	1	-0.00550				0.965	Insignificant
$X_1X_4$	1	0.09723				0.03374	Significant
$X_2X_3$	1	-0.217				0.007	Significant
$X_2X_4$	1	0.02946				0.222	Insignificant
$X_3X_4$	1	-0.00667				0.531	Insignificant
Residual	15		146.10	9.740			
Lack of fit (LOF)	10		122.25	12.23	2.5636	0.155	Insignificant
Pure error	5		23.84	4.769			
Total	20		1897.1				

R<sup>2</sup>: 0.923; adjusted R<sup>2</sup>: 0.851; R<sup>2</sup> for prediction: 0.611

\*P-value < 0.05: statistically significant at the confident level of 95%

**3. RESULTS AND DISCUSSION**

**3.1. Regression model and statistical analysis for the FFA conversion in WCGO**

The experimental and foreseen results of the FFA conversion in WCGOs were shown in Table 2. As per RSM, the full factorial CCD was utilized to fix the acquired data to Eq. (3). As the results, the best fit model was described in Eq. (4):

$$FFA\ Conversion\ (\%) = 11.32X_2 - 2.777X_4 + 0.01379X_4^2 + 0.09723X_1X_4 - 0.217X_2X_3$$

The ANOVA results for the adapted regression model were summarized in Table 3. The suitability of the designed model was evaluated as per F-value, P-value, R<sup>2</sup>, and lack of fit (LOF).<sup>7,8</sup> At 95% confidence level,

F-value and P-value were 12.84 and below 0.0001, respectively. Correlation coefficient,  $R^2$ , illustrated that 92.3% of the FFA conversion variation was influenced by independent variables as in Table 1. Only 7.7% of this variation was from randomly errors. Moreover, the LOF ( $0.155 > 0.05$ ) shown that the LOF was not significant. These values indicated that model term are significant and suitable to forecast the FFA conversion in WCGO.

Also, as shown in Table 3, each term in the regression model was also evaluated to test how well the importance and its interconnection to the FFA conversion in WCGO. A P-value less than 0.05 shows that this term is significant. After withdrawing insignificant terms, by considering the linear, square, and interaction impacts, the linear term of  $H_2SO_4$ /WCGO catalyst content ( $X_2$ ), and reaction time ( $X_4$ ), the square term of reaction time ( $X_4^2$ ), the interaction terms of  $X_1X_4$  and  $X_2X_3$  were significant (as in Eq. 4).

The residual plots were investigated for the model examining in Figure 1a – 1d. The standardized residuals plot for all tests were indicated in Figure 1a. It shows values between  $\pm 1.5$  expressing that the estimation of the fixed model to the response was quite good.<sup>6,8</sup> The expected normal value and residual plot was utilized to express the issuing figure of the data (Figure 1b). This plot was almost linearly indicating that it was normally issued in the model response. The correlation between studentized residuals and predicted values specified that the points were under the meanwhile  $\pm 2.5$  (Figure 1c). This designated that there was no need for variation of the response variable. The predicted values against real benefits were indicated clearly in Figure 1d. The data have linear conduct and are issued near diagonal line. Consequently, the obtained model is acceptable to predict the FFA conversion in WCGO via esterification reaction.

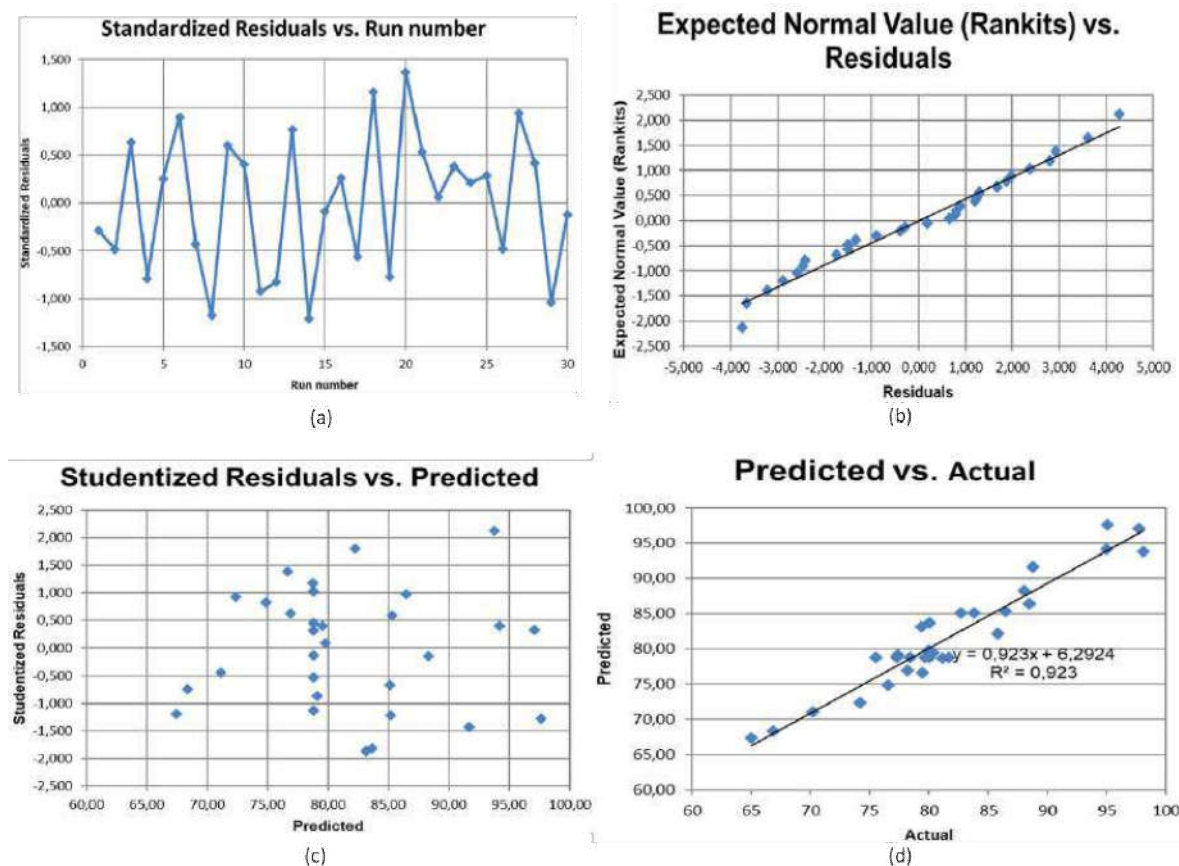


**Figure 1.** (a) standardized residual and run number plot, (b) expected normal value and residuals plot; (c) studentized residuals and predicted values plot; (d) predicted values and actual values plot

**3.2. Interaction effects of the factors on the FFA conversion in WCGO**

The impacts of the interaction factors were shown clearly in Figures 2a – 2f. The slope of the contour will decide the interaction’s degree of this variable to FFA conversion in WCGO – the higher slope is the greater effect gets. The higher slope of the contour of the catalyst content indicated higher effect of this variable in comparison with the molar ratio (Figure 2a). Next, by using at least 1 wt.% of H<sub>2</sub>SO<sub>4</sub> (to WCGO), FFA conversion clearly increase following the increasing of reaction temperature (Figure 2d). In addition, the slope of the catalyst

content (Figure 2e) is higher the slope of the molar ratio (Figure 2c) at the same reaction time. Moreover, at the same temperature range, the FFA conversion can be up to 100% and 84% by using about 9 wt.% of catalyst content (Figure 2d) and 10 mol/mol (Figure 2b). These results proved the importance of H<sub>2</sub>SO<sub>4</sub> catalyst on esterification reaction. Catalyst has a vital effect on the FFA conversion as detailed coefficients in Eq. (4). Hence, the enlargement of catalyst content expedites the speed of the conversion from FFA to esters (biodiesel). These results are consistent with the published results of the previous studies.<sup>6,8</sup>

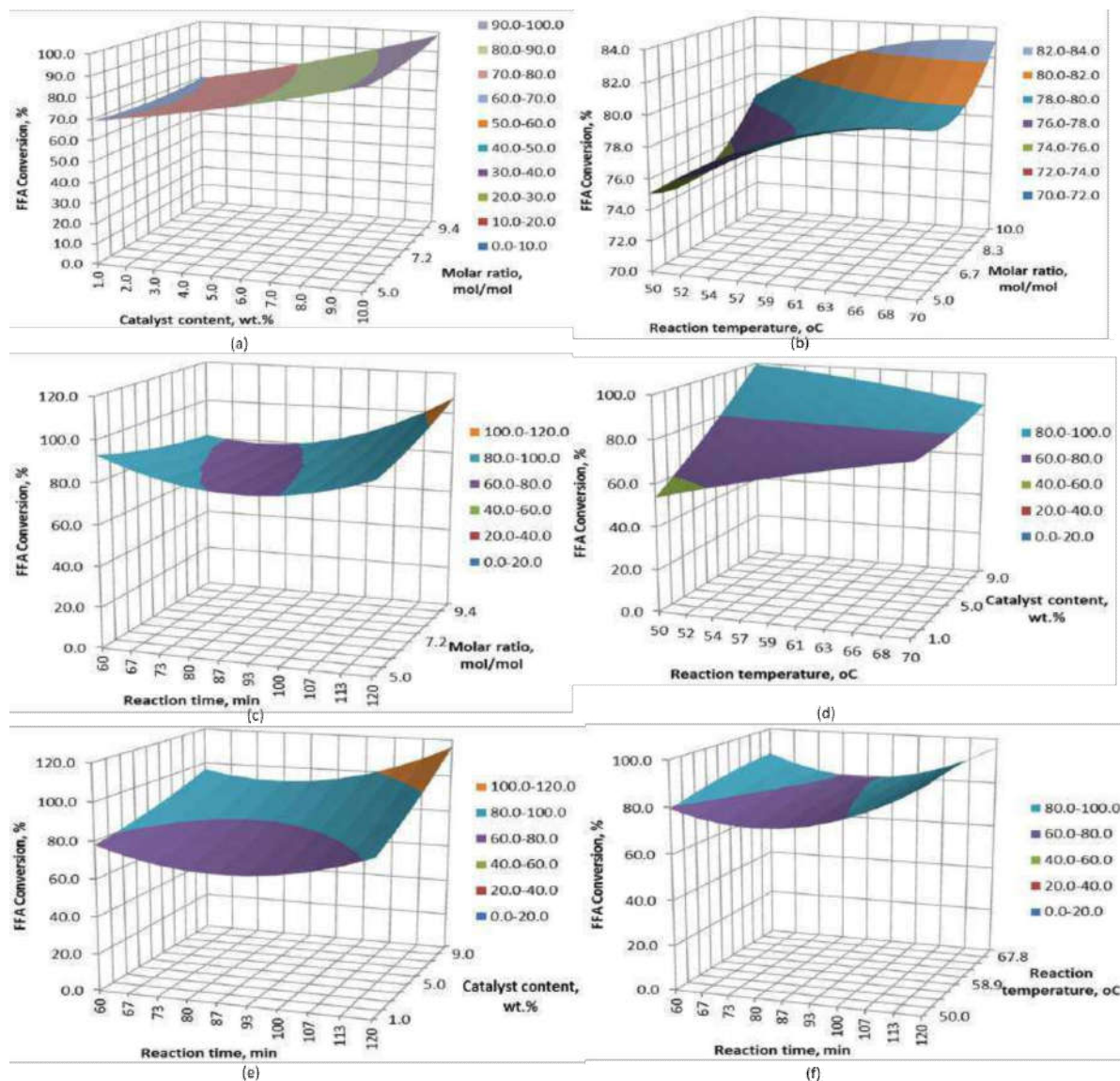


**Figure 2.** Interaction effects of the factors on FFA conversion in WCGO: (a) molar ratio and catalyst content, (b) molar ratio and reaction temperature; (c) molar ratio and reaction time; (d) catalyst content and reaction temperature; (e) catalyst content and reaction time; (f) reaction temperature and time

**3.3. Optimization of variables for the FFA conversion in WCGO**

The aim of this study is to reduce the FFA in WCGO as much as possible. Based on experimental results, the FFA conversion in WCGO changed from 65% to 98%, approximately. With the initial FFA content about 7 wt.%, the experimental condition to gain 90% of FFA conversion (final FFA content about 0.71 wt.%) were chosen to optimize via RSM. The optimum parameters were determined clearly, including the MeOH/WCGO molar ratio of 8.18 mol/mol, H<sub>2</sub>SO<sub>4</sub>/WCGO catalyst content of 8.74 wt.%, reaction temperature of 60 °C and reaction time of 90 min.

**3.4. The fuel properties analysis of the final product**

Some important properties of the esterified oil are shown in Table 4. Most of the properties of the final product met the limits according to standards of European Nations (EU), American Society for Testing and Materials (ASTM) as well as Vietnam (TCVN), except the viscosity at 40 °C. The reason for this problem is that the unsaturated fatty acids (palmitic acid, stearic acid) content in WCGO are quite high.<sup>4,5</sup> The viscosity of the unsaturated fatty acids increases following the decrease of the number of double bonds in the molecule. However, this problem can be solved in the coming stages of biodiesel production as well as in the blending with petroleum based diesel.

**Table 4.** Some properties of the esterified oil

Item	Property	Unit	Test method	Specification	Result
1	FFA content	wt.%	ASTM D664	≤ 1	0.71 ± 0.03
2	Density at 15 °C	kg/m <sup>3</sup>	TCVN 6594 (ASTM D1298)	860 – 900	879 ± 5
3	Viscosity at 40 °C	cSt	ASTM D445	3.5 – 5.0	5.3 ± 0.2
4	Water content	wt.%	TCVN 2631-1993 (ASTM D2709)	≤ 0.05	0.045 ± 0.002
5	Carbon residue	wt.%	TCVN 6324 (ASTM D189)	≤ 0.3	0.29 ± 0.01
6	Sulfated ash	wt.%	EN 14538 (ASTM D874)	≤ 0.02	0.012 ± 0.002
7	Flash point	°C	TCVN 2699-1995 (ASTM D93)	≥ 130	152 ± 2

**4. CONCLUSIONS**

The conversion of FFA in WCGO by esterification using CCD based on RSM was evaluated. Some important conclusions are drawn as follows:

- The proposed model was applied to forecast the influence of variables to lessen the FFA content. The agreement of this model was demonstrated by a high correlation coefficients ( $R^2 = 0.923$ ).
- The FFA content in WCO is decreased from 7 wt.% to 0.7 wt% and 90 % FFA conversion was reached, within the advisable standard to produce biodiesel (max 1 wt.% of FFA).
- The impact of experiment variables for

the acid-catalyzed esterification was explored and optimized as per RSM, such as the MeOH/WCGO molar ratio, H<sub>2</sub>SO<sub>4</sub>/WCGO catalyst content, temperature and reaction time. RSM indicated that the catalyst content are the most important factor to the predicted model.

- Most of the properties of the final esterified oil adapt as per strictly standards. This may be a good cornerstone for the next stages of biodiesel production.

**Acknowledgement:** *This research is conducted within the framework of the student scientific research project for the academic year 2020 - 2021 under the project code S2020.657.21.*

## REFERENCES

1. Dang Nguyen Thoai, C. Tongurai, K. Prasertsit, A. Kumar. Review on biodiesel production by two-step catalytic conversion, *Biocatalysis and Agricultural Biotechnology*, **2019**, *18*, 101023.
2. Z. Al-Hamamre, S. Foerster, F. Hartmann, M. Kröger, M. Kaltschmitt. Oil extracted from spent coffee grounds as a renewable source for fatty acid methyl ester manufacturing, *Fuel*, **2012**, *96*, 70–76.
3. USDA Foreign Agricultural Service, Global Agricultural Information Network, Vietnam Coffee Annual 2019. Available online at <https://asiacom.vn/vietnam-coffee-exports-under-the-top-2-of-the-world/>.
4. D. R. Vardon, B. R. Moser, W. Zheng, K. Witkin, R. L. Evangelista, T. J. Strathmann, K. Rajagopalan, and B. K. Sharma. Complete utilization of spent coffee grounds to produce biodiesel, bio-oil, and biochar, *ACS Sustainable Chemistry & Engineering*, **2013**, *1*, 1286–1294.
5. M. R. Marcelo de Melo, H. M. A. Barbosa, C. P. Passos, C. M. Silva. Supercritical fluid extraction of spent coffee grounds: Measurement of extraction curves, oil characterization and economic analysis, *The Journal of Supercritical Fluids*, **2014**, *86*, 150–159.
6. C. Mueanmasa, R. Nikhoma, J. Kaew-Ona, K. Prasertsit. Statistical optimization for esterification of waste coffee grounds oil using response surface methodology, *Energy Procedia*, **2017**, *138*, 235–240.
7. D. D. Steppan, J. Werner, R. P. Yeater. *Essential regression and experimental design for chemists and engineers*, Electronic Book, 1998.
8. Dang Nguyen Thoai, C. Tongurai, K. Prasertsit, A. Kumar. Predictive Capability Evaluation of RSM and ANN in Modeling and Optimization of Biodiesel Production from Palm (*Elaeisguineensis*) Oil, *International Journal of Applied Engineering Research*, **2018**, *13*(10), 7529–7540.



**CONTENTS**

1.	A sampling technique for light display <b>Le Thi Kim Nga, Doan Thi Xuong, Luong Thi Mong Duyen</b> .....	6
2.	Study on dynamic characteristics of three-phase single-side linear induction motor used in elevator <b>Truong Minh Tan, Nguyen Binh Tai</b> .....	14
3.	Optimal operation of the energy network (electricity - gas) considering solar, wind, and energy storages system based on energy hub modeling <b>Ha Thanh Tung, Pham Thi Hong Anh, Pham Thi Ngoc Dung</b> .....	22
4.	Proposing a strength design process of reinforced concrete beams under combined bending and torsion based on TCVN 5574:2018 standard <b>Pham Thi Lan, Hoang Cong Duy</b> .....	32
5.	Effect of some micro-organic fertilizers on growth and spear yield of <i>Asparagus officinalis</i> L. planted in Quy Nhon city, Binh Dinh province <b>Nguyen Thi Y Thanh, Bui Hong Hai, Doan Cong Thien, Ho Tan</b> .....	44
6.	Local convergence of an inexact Newton-type method involving optimization model on subproblems <b>Tran Ngoc Nguyen, Nguyen Van Vu</b> .....	54
7.	On a matrix equation <b>Nguyen Duy Ai Nhan, Du Thi Hoa Binh</b> .....	62
8.	Identification of cracks in structure by Wavelet transform method <b>Hoang Cong Vu, Nguyen Thi Thao Nguyen</b> .....	68
9.	Central composite design-based optimization for conversion of free fatty acids in oil extracted from coffee grounds into biodiesel <b>Phan Thi Thanh Phuong, Vo Van Tien, Nguyen Viet Quang, Le Thi Thanh Ngan, Dang Nguyen Thoai</b> .....	78